Thermoelasticity of multilayered plates with imperfect interfaces

Aurélien Vattré, Ernian Pan

Thermoelasticity of multilayered plates with imperfect interfaces

A. Vattré[a,*], E. Pan[b]

[a]Safran Aircraft Engines, Etablissement de Villaroche, Safran Group, 77550 Moissy-Cramayel, France
[b]Department of Civil Engineering, University of Akron, Akron, OH 44325, United States

Abstract

Three-dimensional exact solutions for temperature and thermoelastic stresses in multilayered anisotropic plates are derived for advanced boundary-value problems with general boundary conditions. The extended Stroh formalism is formulated to include the thermal coupling with the Eringen nonlocal elasticity theory that captures small scale effects. The simply supported structures are subjected to time-harmonic distributions of temperature, combined with tractions, which are represented by means of Fourier series expansions. In particular, the prescribed loads on both the bottom and top surfaces include the uniformly and heterogeneously distributed normal stresses, while imperfect thermal and mechanical contacts between constituents are incorporated at the internal interfaces. Recursive field relations for multilayered plates with imperfect interfaces are consistently articulated by virtue of the traditional propagation matrix method, which is further completed by the dual variable and position technique to overcome numerical instability issues. Three application examples are proposed to throw light on various effects of the externally applied loads and internal imperfections on the thermoelastic fields in multilayered structures. The residual stress fields in graphite fiber-reinforced epoxy matrix composites are shown to be drastically different from those predicted by the classical elasticity theory when nonlocal effects are significant. The stacking sequence and the number of copper and molybdenum in laminated anisotropic plates are of great importance in tailoring interfacial properties, especially if the thermally conducting boundaries are taken into account. The forced vibration analysis of thermal barrier coatings on nickel based superalloys is investigated, including interfacial bonding effects between adjoining layers. Depending on the input frequency amplitude, severe oscillating displacements and stresses take place in the single crystal superalloys that can endanger the safety-related stability and integrity of aircraft engines. Overall, the present formalism should be utilized in the optimal design of sophisticated multilayered structures with desired steady-state and time-harmonic thermoelastic responses.

Keywords: Nonlocal thermoelasticity, time-harmonic vibrations, multilayered plate, imperfect interface, recursive exact solutions

1. Introduction

High performance structures made of multilayered metal composites are extensively applied to wide-range engineering problems in the aeronautical and aerospace industries, particularly due to their unique structural integrity and high strength-to-weight and stiffness-to-weight ratios (Kelly and Zweben, 1964). While the layered composites provide better mechanical properties than those of their individual material components used alone, crack initiation and crack propagation leading to catastrophic failure need to be prevented in operational safety design of laminated materials (Tabiei and Zhang, 2018). Such precautions require accurate predictions of the three-dimensional deformation and stress states in the composite structures. In aircraft engines, rotating high-pressure turbine blades work in severe temperature environments and are furthermore subjected to high frequency vibration events, for which the thermomechanical resonance effects may dramatically reduce the service life of the engines. This work is focused on exact field solutions for time-harmonic vibration response of multilayered composites using nonlocal thermoelasticity theory with specific conditions at the internal interfaces. Besides the conforming finite element analysis for similar problems (Bhangale and Ganesan, 2006a, Carrera, 2000, Tran et al., 2007, Vidal and Polit, 2008), the present framework is of particular value since the corresponding economical solutions can predict exactly the vibrational behavior of multilayered systems without any numerical dispersions and can therefore be used as benchmarks for various numerical methods in nonlocal thermoelasticity.

The three-dimensional problem of determining the strains and stresses which occur in homogeneous rectangular parallelepipeds subjected to given surface forces is one of the oldest problems in the theory of elasticity (Lamé, 1852, Mathieu, 1868, Poisson, 1829). From mathematical aspects, the exact and general solutions have been represented by arbitrary periodic functions expanding into infinite trigonometric series of sine and cosine terms with coefficients to be determined using specific applied conditions at external surfaces (Hutchinson, 1967, Lamé, 1852, Mathieu, 1868, 1890, Mindlin, 1956). Later, the inhomogeneous problem of laminated composite plates consisting of isotropic and orthotropic layers has been rigorously covered using similar mathematical treatments under various approximate plate theories and various types of edge boundary conditions (Pagano, 1970, Reddy, 1984, Srinivas and Rao, 1970, Touratier, 1991, Whitney and Pagano, 1970).

Since the relevant analytical works by Srinivas and Rao (1970) and Pagano (1970), the particular case of layered composites under simply supported lateral conditions has been investigated to describe the displacement and stress distributions in series of bidirectional

*Now at Université Paris-Saclay, ONERA. Email address: aurelien.vattre@onera.fr

square-symmetric laminates under static bending forces. A vibration analysis of simply supported orthotropic plates subjected to several dynamic pulses has been extended using the Fourier series expansion of the load functions (Dobyns, 1981, Taylor and Nayfeh, 1996). The vibration frequencies and mode shapes have therefore been determined as well as the corresponding field solutions for plate deflections, bending strains, and normal shear forces due to the dynamic loads. It is worth noting that the twofold advantage of the simply supported plate conditions is due to the resulting eigenvalue problems that can be solved analytically and to the corresponding feasibility in designing experiments for static and free vibration responses of layered plates (Kapuria et al., 2008). Because of these specific and attractive features, the simply supported elastic plate model has been extended to include the multiphase coupling effect among the mechanical, electrical and magnetic fields for both static deformation (Bhangale and Ganesan, 2006b, Pan, 2001) and free vibration (Pan and Heyliger, 2002) responses in crystalline metal composites as well as in quasicrystalline multi-structures (Yang et al., 2015, 2017).

As the structural length decreases towards the sub-microscale regime, numerous experiments have observed size-dependent mechanical properties in metals (Poole et al., 1996, Wu et al., 2005) that cannot be captured by the classical scale-free continuum theories. Several size-dependent theories that contain additional internal length scale have also been developed to overcome such limitations, e.g., the micropolar (Toupin, 1973) and micromorphic (Eringen, 1967, Mindlin and Eshel, 1968) continuum theories, and nonlocal integral theories that have been stimulated by the pioneer work of Eringen and co-workers (Eringen, 1972, Eringen and Edelen, 1972). The latter consists in postulating that the stress field at a given material point is related to the strain state at that location and to a nonlocal contribution due to the surrounding medium characterized by a convolution integral form with attenuation kernel functions. By focusing on solid-state physics, the long-distance force effects between atoms and the internal length scale are phenomenologically considered in the construction of the stress-strain constitutive equations (Eringen, 1983), without variational arguments. The Eringen elasticity theory has also been conveniently used to analyze many engineering problems in nonlocal elasticity whereby the structural response is strongly influenced by the presence of a microstructure, such as the wave propagation in heterogeneous materials (Maugin, 1999), the stress evaluation at both the dislocation cores (Eringen, 1977) and crack tips (Eringen et al., 1977) as well as the free vibration analysis (Waksmanski and Pan, 2014) and buckling (Guo et al., 2019) in multilayered nanoplates. Although the Eringen theory (Eringen, 1983) did not provide extra boundary conditions required by the constitutive Helmholtz-based partial differential equations, the introduction of nonlocal ingredients into the conventional simply supported plate theories with proper values of nonlocal parameter −through a least-square fitting procedure− has shown excellent size-dependent predictions compared to molecular dynamics simulations in the biaxial buckling response of single-layered graphene sheets (Ansari and Sahmani, 2013).

Furthermore, composite aircraft structures are exposed to thermal environments including severe temperature gradients, for which the anisotropic thermal properties of the individual material components cannot be ignored in a modern structural design of gas turbine blades with advanced ceramic coatings (Padture, 2016). Similarly to the elasticity theory in predicting the deformation and stress states in anisotropic solids, the non-canonical form of the differential operators makes most of the traditional analytical solution procedures for steady-state heat conduction problems (Mulholland and Cobble, 1972) either inapplicable or intractable (Noor and Burton, 1992). Thus, analogous Fourier series expansions as in elasticity have been proposed by Padovan (1975) to solve the three-dimensional heat transfer problem of rectangular laminated plates subject to thermal loads, which have further been extended to combined loads using the quasi-static theory of linear thermoelasticity (Bhaskar et al., 1995, Savoia and Rao, 1995, Tungikar, 1994). The inherent thermoelastic problems are of critical importance since the interaction between the elastic strain and thermal mismatches and also the corresponding thermal stress concentrations may influence the local driving forces for crack propagation in composite materials (Khaund et al., 1977), which is a major cause of fracture and interfacial delamination of thermal barrier coating systems (Evans and Hutchinson, 2007). Under static deformation, additional coupling effects including piezoelectric fields in layered plates have been formulated (Wang and Pan, 2007), whilst Yang et al. (2018) has recently investigated the thermoelastic quasicrystal response in layered plates by surface loading. To the best of the authors' knowledge, however, the corresponding time-dependent thermoelastic vibration response of a multilayered composite with imperfect interface conditions and nonlocal effects has not yet been treated.

The common assumption made by most of the aforementioned works is related to the ideal perfectly bonded conditions at interfaces between adjoining plates, which requires the continuity of the elastic displacement and traction vectors as well as the temperature and the normal heat flux across all internal boundaries. Although these interface conditions are necessary to solve the mathematical problem in hetero-thermoelasticity, appropriate conditions must strongly reflect the physical properties of the interfaces, particularly for complex multilayered thermal barrier coating systems. Due to the experimental evidence, most of the mechanically compliant interfaces are structurally imperfect in heterostructures (Hirth and Lothe, 1992, Sutton and Balluffi, 1995). While dislocation-based models have been formulated to describe the crystallographic character of heterophase interfaces in terms of discrete dislocation networks (Vattré, 2015, 2016, 2017), phenomenological continuum approaches that smear out the detailed dislocation arrangement have frequently been applied to model the effects of imperfect interfaces. For instance, the general linear spring-type model under isothermal conditions has been proposed (Fan and Wang, 2003, Ru and Schiavone, 1997) by specifying a continuous traction vector but a discontinuous displacement field across the imperfect interface, for which the components of the given displacement jump are assumed to be linearly proportional to the interfacial traction components. For the thermal characteristics, the imperfect interfacial contacts may be related to thermally −weakly or highly− conducting boundaries. More specifically, the normal heat flux is continuous but the temperature is discontinuous across the interface for thermally weakly conducting interfaces (Benveniste and Miloh, 1986, Benveniste, 1999), which includes Kapitza contact thermal resistance with a temperature jump proportional to the normal heat flux (Kapitza, 1941), as similarly defined in the elastic spring model. On the other hand, the temperature is continuous across the interface whereas the normal heat flux has a discontinuity across the interface for highly conducting interfaces (Benveniste, 1999, 2006), which is proportional to the local surface Laplacian of temperature. Because of the process-induced surface defects during fusion welding or layer-by-layer additive manufacturing of metallic aircraft components, a detailed treatment of imperfect interfaces is undoubtedly of paramount importance to understand their influence

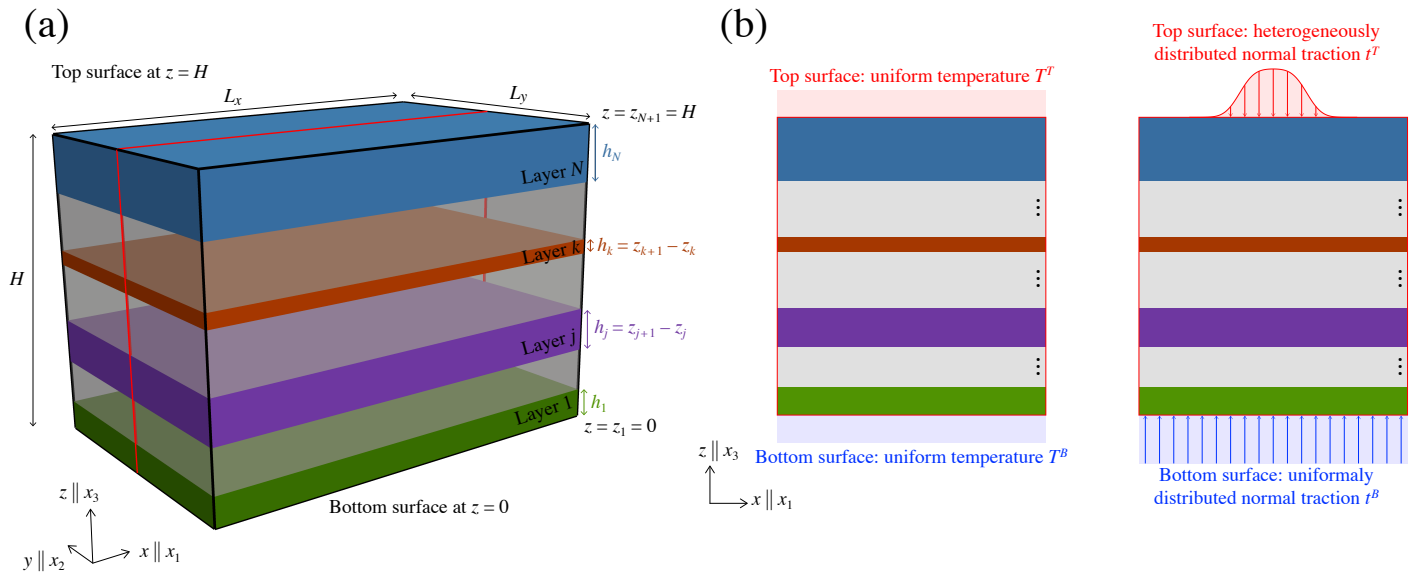

Figure 1: (a) Three-dimensional schematics of a multilayered anisotropic system that is arbitrarily composed of N rectangular layers with nonlocal thermoelastic properties and general imperfect conditions on the internal interfaces. (b) The combined time-harmonic loads are applied on both bottom and top surfaces. The temperature profiles are uniformly distributed, while the normal tractions can be heterogeneously distributed on the external surfaces.

on fatigue performance and corrosion damage.

In this work, a comprehensive analysis is carried out on the time-harmonic response of thermoelastic, anisotropic, and multilayered plates. The layered structure is assumed to be nonlocal with further general imperfect conditions on the internal interfaces between the homogeneous layers. As reviewed above, previous analyses for the thermoelastic layered plates have been conducted under the assumption of static deformation, within which the exact closed-form solutions have been evaluated for individual lower Fourier series terms only. For such restricted circumstances, the traditional propagation matrix method can straightforwardly be applied due to the basic mathematical operations involved. However, because both the positive and negative exponential terms are contained in the propagation matrix method, this technique would fail when the Fourier series term is relatively high and/or when the dynamic frequency is relatively high (Pan, 2019). Thus, in order to take care of the time-harmonic vibration with high frequency as well as higher-order Fourier series terms for thermoelatically distributed and coupled loading problems, the recent dual variable and position technique (Liu et al., 2018, Pan, 2019) has been reformulated by conveniently introducing an elegant rearrangement in the central transfer matrices from the propagation matrix method, combined with the Stroh formalism with nonlocal and thermal effects.

The paper falls into four parts and is organized as follows. The coupled boundary-value problem is described in Section 2. In Section 3, the general time-harmonic solutions for each homogeneous and Eringen-type nonlocal layer are derived by means of double Fourier series expansions. The recursive framework is then developed in Section 4 to determine the exact solutions in the entire multilayers by transferring specific field matrices, including both mechanical and thermal imperfections at internal interfaces. Three application examples are discussed in Section 5, and conclusion remarks are drawn in Section 6.

2. Description of the hetero-thermoelastic problem

Figure (1a) describes the three-dimensional multilayered structure that is composed of an arbitrary number of N-bonded orthotropic, dissimilar, linearly thermoelastic, and rectangular layers with nonlocal effects. Here and in the following, the individual and finite thickness is $h_j = z_{j+1} - z_j$ for the j^{th} layer, with $j = 1, \ldots, N$. A global orthogonal system $(x, y, z) = (x_1, x_2, x_3)$ with Cartesian coordinates is attached to the multilayers where the origin is located at one of the four corners on the bottom surface and all plates are defined in the positive z-region. Thus, the lower and upper interfaces of layer j are defined as z_j and z_{j+1}, respectively, and the in-plane $x \parallel x_1$- and $y \parallel x_2$- directions are aligned with the horizontal edges of the plate boundaries. It follows that $z_1 = 0$ and $z_{N+1} = H$ at the bottom and top surfaces, respectively, with H the total thickness in the vertical direction of the multilayers, while the common dimensions in the $x \parallel x_1$- and $y \parallel x_2$- directions are L_x and L_y for all plates. The four lateral sides are assumed to satisfy the simply supported boundary conditions, and the general combined thermal and mechanical loads are applied on the bottom and top surfaces of the multilayers. Some of the internal interfaces between the adjacent layers are perfectly or imperfectly connected, which will be discussed later on.

2.1. Nonlocal constitutive and governing equations

In the nonlocal theory of steady-state heat conduction, the nonlocal heat flux vector q_i in W/m^2 is proportional to the local temperature gradient (Yu et al., 2016), as follows

$$\left(1 - l_T^2 \nabla^2\right) q_i = -k_{ij} T_{,j} \,, \tag{1}$$

where l_T is the thermal nonlocal parameter in m, k_{ij} are the coefficients of thermal conductivity in W/m/K, and T is the temperature in K. In eq. (1), a comma followed by index j denotes partial differentiation with respect to the position x_j of a material point with $j = 1, 2, 3$, and a repeated index implies summation over the range of the index, while ∇^2 is the 3D Laplacian operator. On the other hand, the anisotropic constitutive relations for each linear and homogeneous Eringen nonlocal plate (Eringen, 1983) including thermal stresses are given by

$$\left(1 - l_E^2 \nabla^2\right) \sigma_{ij} = c_{ijkl} u_{k,l} - \beta_{ij} T = c_{ijkl} u_{k,l} - c_{ijkl} \alpha_{kl} T \,, \tag{2}$$

where l_E is the elastic nonlocal parameter, σ_{ij} is the nonlocal elastic stress tensor in N/m^2, c_{ijkl} are the elastic stiffness constants in N/m^2, u_k is the elastic displacement vector in m, and β_{ij} are the thermal constants in N/m^2/K. In general, the coefficients β_{ij} can be obtained in terms of the thermal expansion coefficients α_{kl} in 1/K and the stiffness tensor, as defined in eq. (2). For orthotropic materials with the three orthogonal planes of symmetry in the fixed Cartesian coordinates (x_1, x_2, x_3), eq. (2) can be expressed in the matrix form as

$$\left(1 - l_E^2 \nabla^2\right) \begin{bmatrix} \sigma_{11} \\ \sigma_{22} \\ \sigma_{33} \\ \sigma_{23} \\ \sigma_{13} \\ \sigma_{12} \end{bmatrix} = \begin{bmatrix} c_{11} & c_{12} & c_{13} & 0 & 0 & 0 \\ c_{12} & c_{22} & c_{23} & 0 & 0 & 0 \\ c_{13} & c_{23} & c_{33} & 0 & 0 & 0 \\ 0 & 0 & 0 & c_{44} & 0 & 0 \\ 0 & 0 & 0 & 0 & c_{55} & 0 \\ 0 & 0 & 0 & 0 & 0 & c_{66} \end{bmatrix} \begin{bmatrix} u_{1,1} \\ u_{2,2} \\ u_{3,3} \\ u_{2,3} + u_{3,2} \\ u_{1,3} + u_{3,1} \\ u_{1,2} + u_{2,1} \end{bmatrix} - \begin{bmatrix} \beta_{11} \\ \beta_{22} \\ \beta_{33} \\ 0 \\ 0 \\ 0 \end{bmatrix} T \,, \tag{3}$$

with c_{ij} the stiffness tensor indexed in Voigt notation. For each individual plate, the balance equation for the steady-state thermal flux without internal heat sources and the time-harmonic equation for the linear thermoelastic deformations in the absence of body forces acting on the materials are both defined by

$$\begin{cases} q_{i,i} = 0 \,, & \text{(4a)} \\ \sigma_{ij,j} - \rho \ddot{u}_i = 0 \,, & \text{(4b)} \end{cases}$$

with ρ being the mass density in kg/m^3, and the superposed dot denotes the differentiation with respect to time. Assuming time-harmonic vibration motion, the field solution of the elastic displacement vector u_i in eqs. (3) and (4b) is sought in the complex standard form and is separated into a function of position and a function of time, as follows

$$u_i\left(x_1, x_2, z, t\right) = \hat{u}_i\left(x_1, x_2, z\right) \mathrm{e}^{i\omega t} \,, \tag{5}$$

where $\hat{u}_i$ is the time-independent nonlocal displacement vector, ω is the angular vibration frequency of excitation in rad/s, and t is time in s. Substituting eq. (5) into eq. (2), the governing partial differential equation of motion in eq. (4b) reads

$$\rho\omega^2 \left(1 - l_E^2 \nabla^2\right) u_i + c_{ijkl} u_{k,lj} - \beta_{ij} T_{,j} = 0 \,, \tag{6}$$

for which the corresponding solution of the deformation state has no effects on temperature. Thus, the general thermal stress problem separates into two distinct problems to be solved consecutively. The steady-state thermal stress analysis can be carried out by solving the heat conduction problem with eq. (4a) first, also by obtaining the temperature field in the static form of eq. (1), and then solving the elasticity problem and determining the thermally induced deformations and stresses from eq. (6). To solve this three-dimensional problem, a representation of field solutions by means of double Fourier trigonometric expansions is considered.

2.2. The three-dimensional boundary-value problem

In the present boundary-value problem, the appropriate boundary conditions that must be satisfied are those on the external surfaces, i.e., at the edges of the multilayered rectangular plate and both horizontal surfaces where the combined time-harmonic thermal and mechanical loads are prescribed, as well as those on the internal interfaces of the multilayered rectangular plates. These boundary conditions are described in the following sections.

2.2.1. External boundary conditions

For the simply supported rectangular composite materials with ideal constraints at the edges, the prescribed boundary conditions at four vertical surface planes are expressed as

$$\begin{cases} u_2 = u_3 = \sigma_{22} = T = 0 \,, \quad \text{at:} \;\; x_1 = 0, \text{ and } \; x_1 = L_x \,, & \text{(7a)} \\ u_1 = u_3 = \sigma_{11} = T = 0 \,, \quad \text{at:} \;\; x_2 = 0, \text{ and } \; x_2 = L_y \,, & \text{(7b)} \end{cases}$$

for all plates along the entire thickness of the multilayered materials. On the other hand, the boundary conditions B on the bottom surface are assumed to be sufficiently general to solve the thermoelastic problem in multilayered materials, where both the time-harmonic

temperature T and normal stress vector t_i are expressed using the two-dimensional Fourier series ansatz (Dobyns, 1981, Srinivas and Rao, 1970, Taylor and Nayfeh, 1996), as follows

$$\mathrm{B}: \begin{cases} T\left(x_1,x_2,z=0,t\right) = \mathrm{e}^{i\omega t} \sum\limits_{m=1}^{\infty} \sum\limits_{n=1}^{\infty} \bar{T}^{B}_{mn} \sin\left(p_m x_1\right) \sin\left(q_n x_2\right), & \text{(8a)} \\ t_i\left(x_1,x_2,z=0,t\right) = \begin{bmatrix} \sigma_{31}\left(x_1,x_2,z=0,t\right) \\ \sigma_{32}\left(x_1,x_2,z=0,t\right) \\ \sigma_{33}\left(x_1,x_2,z=0,t\right) \end{bmatrix} = \mathrm{e}^{i\omega t} \sum\limits_{m=1}^{\infty} \sum\limits_{n=1}^{\infty} \begin{bmatrix} \bar{\sigma}^{B}_{31mn} \cos\left(p_m x_1\right) \sin\left(q_n x_2\right) \\ \bar{\sigma}^{B}_{32mn} \sin\left(p_m x_1\right) \cos\left(q_n x_2\right) \\ \bar{\sigma}^{B}_{33mn} \sin\left(p_m x_1\right) \sin\left(q_n x_2\right) \end{bmatrix}, & \text{(8b)} \end{cases}$$

where the quantities $\bar{T}^{B}_{mn}$ and $\bar{\boldsymbol{t}}^{B}_{mn} = \left[\bar{\sigma}^{B}_{31mn}, \bar{\sigma}^{B}_{32mn}, \bar{\sigma}^{B}_{33mn}\right]^{\mathrm{t}}$ are the Fourier amplitudes applied on the bottom surface, with the superscript $^{\mathrm{t}}$ indicating the vector transpose. In eqs. (8), the half-wave numbers are given by $p_m = m\pi/L_x$ and $q_n = n\pi/L_y$, with m and n being two positive integers, so that all Fourier series expansion coefficients are related to the summations for m and n. Similarly, the external boundary conditions T on top surface are given by

$$\mathrm{T}: \begin{cases} T\left(x_1,x_2,z=H,t\right) = \mathrm{e}^{i\omega t} \sum\limits_{m=1}^{\infty} \sum\limits_{n=1}^{\infty} \bar{T}^{T}_{mn} \sin\left(p_m x_1\right) \sin\left(q_n x_2\right), & \text{(9a)} \\ t_i\left(x_1,x_2,z=H,t\right) = \begin{bmatrix} \sigma_{31}\left(x_1,x_2,z=H,t\right) \\ \sigma_{32}\left(x_1,x_2,z=H,t\right) \\ \sigma_{33}\left(x_1,x_2,z=H,t\right) \end{bmatrix} = \mathrm{e}^{i\omega t} \sum\limits_{m=1}^{\infty} \sum\limits_{n=1}^{\infty} \begin{bmatrix} \bar{\sigma}^{T}_{31mn} \cos\left(p_m x_1\right) \sin\left(q_n x_2\right) \\ \bar{\sigma}^{T}_{32mn} \sin\left(p_m x_1\right) \cos\left(q_n x_2\right) \\ \bar{\sigma}^{T}_{33mn} \sin\left(p_m x_1\right) \sin\left(q_n x_2\right) \end{bmatrix}, & \text{(9b)} \end{cases}$$

where $\bar{T}^{T}_{mn}$ and $\bar{\boldsymbol{t}}^{T}_{mn} = \left[\bar{\sigma}^{T}_{31mn}, \bar{\sigma}^{T}_{32mn}, \bar{\sigma}^{T}_{33mn}\right]^{\mathrm{t}}$ are the Fourier amplitudes applied on the top rectangular surface at $z = H$. It is worth noting that the double Fourier series expansions in eqs. (8) and (9) satisfy the homogeneous lateral boundary conditions given in eq. (7), with m and n occurring as parameters. In the following, both superscripts over p_m and q_n are omitted to avoid notational complexity, unless needed, and whenever the periodic terms arise, summation over m and n must be made.

2.2.2. Internal boundary conditions

The traditional boundary condition for mechanically compliant non-ideal interfaces in anisotropic composite laminates, which enables conformability to non-flat and irregularly shaped surfaces to accommodate the residual stresses between two adjacent materials, are formulated as follows

$$\begin{cases} \left[\!\left[\, \sigma_{3j}\left(x_1,x_2,z=z_k,t\right) \,\right]\!\right]^{+}_{-} = \sigma_{3j}\left(x_1,x_2,z=z^{+}_{k},t\right) - \sigma_{3j}\left(x_1,x_2,z=z^{-}_{k},t\right) = 0, & \text{(10a)} \\ \left[\!\left[\, u_j\left(x_1,x_2,z=z_k,t\right) \,\right]\!\right]^{+}_{-} = u_j\left(x_1,x_2,z=z^{+}_{k},t\right) - u_j\left(x_1,x_2,z=z^{-}_{k},t\right) = \alpha^{(k)}_{j}\, \sigma_{j3}\left(x_1,x_2,z_k,t\right), & \text{(10b)} \end{cases}$$

for $j = \{1,2,3\}$, where both superscripts $^{+}$ and $^{-}$ denote the limit values from the upper and lower sides of any interface of interest located at $z = z_k$, with $k = 2,\ldots,N$. The mechanical contact feature in eqs. (10) is the general spring-type interface condition where traction is continuous but the elastic displacements experience a jump crossing the interface. The proportional interface coefficients $\alpha^{(k)}_{j}$ in m^3/N are also designated by interface compliances. In practice, when the latter interface compliances approach zero, the standard condition for ideal mechanical interfaces is verified, while the completely mechanically debonded interfaces are characterized when the interface coefficients tend to infinity.

As part of the thermal conduction, two anisotropic boundary conditions are taken into account to represent weakly and highly conducting non-ideal interfaces. For weakly conducting interfaces, the Kapitza model is used to describe a possible interfacial thermal resistance, as follows

$$\begin{cases} \left[\!\left[\, q_3\left(x_1,x_2,z=z_k,t\right) \,\right]\!\right]^{+}_{-} = q_3\left(x_1,x_2,z=z^{+}_{k},t\right) - q_3\left(x_1,x_2,z=z^{-}_{k},t\right) = 0, & \text{(11a)} \\ \left[\!\left[\, T\left(x_1,x_2,z=z_k,t\right) \,\right]\!\right]^{+}_{-} = T\left(x_1,x_2,z=z^{+}_{k},t\right) - T\left(x_1,x_2,z=z^{-}_{k},t\right) = -\beta^{(k)}_{T}\, q_3\left(x_1,x_2,z_k,t\right), & \text{(11b)} \end{cases}$$

causing a jump in the temperature and thus changing the effective thermal conductivity of the composite material. In eq. (11b), the adiabatic condition at the contact interfaces is obtained when the non-negative interfacial constant $\beta^{(k)}_{T}$ in Km^2/W tends to infinity. On the other hand, the boundary conditions for highly conducting imperfect interfaces are written as

$$\begin{cases} \left[\!\left[\, q_3\left(x_1,x_2,z=z_k,t\right) \,\right]\!\right]^{+}_{-} = q_3\left(x_1,x_2,z=z^{+}_{k},t\right) - q_3\left(x_1,x_2,z=z^{-}_{k},t\right) = \gamma^{(k)}_{T}\, \nabla^2_{\mathrm{2D}}\, T\left(x_1,x_2,z_k,t\right), & \text{(12a)} \\ \left[\!\left[\, T\left(x_1,x_2,z=z_k,t\right) \,\right]\!\right]^{+}_{-} = T\left(x_1,x_2,z=z^{+}_{k},t\right) - T\left(x_1,x_2,z=z^{-}_{k},t\right) = 0, & \text{(12b)} \end{cases}$$

where $\nabla^2_{\mathrm{2D}} = \left(\partial_{11} + \partial_{22}\right)$ is the surface Laplacian operator and $\gamma^{(k)}_{T}$ is a non-negative interfacial parameter in W/K, for which the upper material is connected to the adjacent lower material with infinite conductivity if $\gamma^{(k)}_{T}$ approaches infinity.

For both interfacial heat conditions given in eqs. (11) and (12), the perfect thermal conditions for ideal interfaces are met when $\beta^{(k)}_{T} = \gamma^{(k)}_{T} = 0$, exhibiting the continuity of temperature and heat flux at ideal interfaces. Because all aforementioned relations are proportional to the common factor $\mathrm{e}^{i\omega t}$, the above mechanical and thermally internal boundary conditions can conveniently be expressed with respect to time-independent field quantities by omitting the time parameter t in eqs. (10), (11) and (12).

3. General series solutions for each Eringen nonlocal plate

General and exact field solutions for each three-dimensional homogeneous plate are derived using the pseudo-Stroh formalism with respect to the nonlocal constitutive relations developed in Section 2.1. The corresponding expressions fulfill both governing equations for thermoelasticity given in eqs. (4a) and (6) exactly in terms of Fourier series expansion functions, which will be further used to determine the complete solutions for multilayered plates by assembly techniques in Section 4. For clarity, a convenient local coordinate system (x_1, x_2, z') is attached to the individual j^{th} layer, with origin at the point where the global $x_3 \parallel z$ axis intersects the bottom surface of the j^{th} plate. The local axes are also parallel to the global axes such that z' and z are related to each other by a translation. The temperature and the nonlocal heat flux vector are first determined in Section 3.1, while Sections 3.2 and 3.3 are associated with the so-called primary and secondary variables of the thermoelastic solutions. The displacement u_i and traction t_i components are the six primary variables calculated by a specific eigenvalue problem, whereas the three secondary in-plane components $\tau_i = [\sigma_{11}, \sigma_{12}, \sigma_{22}]^{\mathrm{t}}$ can be expressed in terms of the primary variables using the constitutive relations.

3.1. Thermal field solutions

Similarly to the expressions for the external boundary conditions on the bottom B and top T surfaces in eqs. (8a) and (9a), the formal time-harmonic solutions for the temperature and normal heat flux components are written to satisfy exactly the simply supported boundary conditions by means of the separation of variables method combined with a Fourier sine-series expansion form, as follows

$$\begin{bmatrix} T(x_1,x_2,z',t) \\ q_3(x_1,x_2,z',t) \end{bmatrix} = \mathrm{e}^{i\omega t} \sum_{m=1}^{\infty} \sum_{n=1}^{\infty} \begin{bmatrix} \bar{T}(z') \sin(px_1) \sin(qx_2) \\ \bar{q}_3(z') \sin(px_1) \sin(qx_2) \end{bmatrix} = \mathrm{e}^{i\omega t}\, \mathrm{e}^{\eta z'} \sum_{m=1}^{\infty} \sum_{n=1}^{\infty} \begin{bmatrix} f \sin(px_1) \sin(qx_2) \\ g \sin(px_1) \sin(qx_2) \end{bmatrix}, \tag{13}$$

where $\bar{T}(z') = f\,\mathrm{e}^{\eta z'}$ and $\bar{q}_3(z') = g\,\mathrm{e}^{\eta z'}$ are two unknown z'-dependent functions, within which f, g and η are the coefficients to be determined. Thus, eq. (13) and the corresponding thermal material properties are explicitly defined for each layer j of the composite plate of interest. Furthermore, for symmetric reasons with respect to the three coordinate planes, the remaining in-plane components q_1 and q_2 of the heat flux vector are expressed by interchanging the sine and cosine terms in the appropriate directions along x_1 and x_2, respectively, as formulated in eqs. (8b) and (9b). Thus, the three components q_i of the heat flux can be obtained from eq. (1) as

$$\left(1 - l_T^2\left(\eta^2 - p^2 - q^2\right)\right) q_1\left(x_1,x_2,z',t\right) = -k_{11}\, p\, \mathrm{e}^{i\omega t}\, \mathrm{e}^{\eta z'} f \cos(px_1) \sin(qx_2)\,, \tag{14a}$$

$$\left(1 - l_T^2\left(\eta^2 - p^2 - q^2\right)\right) q_2\left(x_1,x_2,z',t\right) = -k_{22}\, q\, \mathrm{e}^{i\omega t}\, \mathrm{e}^{\eta z'} f \sin(px_1) \cos(qx_2)\,, \tag{14b}$$

$$\left(1 - l_T^2\left(\eta^2 - p^2 - q^2\right)\right) q_3\left(x_1,x_2,z',t\right) = -k_{33}\, \eta\, \mathrm{e}^{i\omega t}\, \mathrm{e}^{\eta z'} f \sin(px_1) \sin(qx_2)\,, \tag{14c}$$

where the linear Helmholtz-type differential operator ∇^2 in eq. (1) has explicitly been replaced with $(\eta^2 - p^2 - q^2)$, which obviously exhibits in essence a subsequent advantage of using such Fourier series representation in nonlocal thermoelasticity. Substituting the derivatives of the heat flux components of eqs. (14) into the governing heat conduction eq. (4a), the following eigenrelation is obtained

$$\left(k_{11}\, p^2 + k_{22}\, q^2 - k_{33}\, \eta^2\right) f = 0\,, \tag{15}$$

where two nontrivial eigenvalue solutions $\{\eta_1, \eta_2\}$ for η with $k_{33} \neq 0$ are given by

$$\eta = \pm\sqrt{\left(k_{11}\, p^2 + k_{22}\, q^2\right)/k_{33}} \quad \Rightarrow \quad \eta_1 = \sqrt{\left(k_{11}\, p^2 + k_{22}\, q^2\right)/k_{33}} = -\eta_2\,, \tag{16}$$

by eliminating the trivial solution $f = 0$ from eq. (15). According to eq. (13), the derivative of the normal heat flux reads

$$q_{3,3}\left(\eta^2 - p^2 - q^2\right) = \eta\, \mathrm{e}^{i\omega t}\, \mathrm{e}^{\eta z'} g \sin(px_1) \sin(qx_2)\,, \tag{17}$$

so that a similar relation as eq. (15) is obtained by substituting eq. (17) and the derivatives of eqs. (14a) and (14b) in eq. (4a), as follows

$$\left(\left(1 - l_T^2\left(\eta^2 - p^2 - q^2\right)\right) k_{11}\, p^2 + \left(1 - l_T^2\left(\eta^2 - p^2 - q^2\right)\right) k_{22}\, q^2\right) f + \eta\, g = 0\,, \tag{18}$$

at every material point and for all time. Consequently, eqs. (15) and (18) can together be recast into the following time-independent linear system

$$-\begin{bmatrix} 0 & \left(\left(1 - l_T^2\left(\eta^2 - p^2 - q^2\right)\right) k_{33}\right)^{-1} \\ \left(1 - l_T^2\left(\eta^2 - p^2 - q^2\right)\right)\left(k_{11}\, p^2 + k_2 2\, q^2\right) & 0 \end{bmatrix} \begin{bmatrix} f \\ g \end{bmatrix} = \eta \begin{bmatrix} f \\ g \end{bmatrix}, \tag{19}$$

where a set of homogeneous algebraic equations leads to a classical eigenvalue problem for each pair of integers m and n. Without the proportional sine and cosine terms for clarity, the general z'-dependent solutions for the steady-state thermal quantities in each Eringen nonlocal layer can be expressed as

$$\begin{bmatrix} \bar{T}(z') \\ \bar{q}_3(z') \end{bmatrix} = \begin{bmatrix} f_1 & f_2 \\ g_1 & g_2 \end{bmatrix} \begin{bmatrix} \mathrm{e}^{\eta_1 z'} & 0 \\ 0 & \mathrm{e}^{\eta_2 z'} \end{bmatrix} \begin{bmatrix} d_1 \\ d_2 \end{bmatrix}, \tag{20}$$

where the eigenvalues $\{\eta_1,\eta_2\}=\eta_k$ are given in eq. (16), and f_k and g_k are the corresponding eigenvectors of eq. (19) with respect to η_k. In eq. (20), both quantities d_1 and d_2 are two unknown constants to be determined by the thermal interface boundary conditions, as considered in Section 4. While the extracted eigenvalues η_k from standard techniques and the corresponding eigenvectors f_k in the nonlocal case are the same as those in the local case, the eigenvectors g_k are different and depend on the nonlocal thermal parameter l_T, with $g_k=g_k^{\text{local}}/(1-l_T^2(\eta^2-p^2-q^2))$. A set of solution for the local eigenvectors is conveniently chosen to satisfy the relation $f_1+f_2+g_1+g_2=1-l_T^2(\eta^2-p^2-q^2)$, so that

$$\begin{bmatrix} f_1 & f_2 \\ g_1 & g_2 \end{bmatrix} = -\begin{bmatrix} -1 & (2k_{33}\eta_1)^{-1} \\ k_{33}\eta_1\left(1-l_T^2\left(\eta^2-p^2-q^2\right)\right)^{-1} & \left(2\left(1-l_T^2\left(\eta^2-p^2-q^2\right)\right)\right)^{-1} \end{bmatrix}, \tag{21}$$

which can be substituted into eq. (20) and subsequently into eq. (13) to determine the general three-dimensional time-dependent solutions for both the temperature and normal heat flux. To complete the z'-dependent heat flux solutions with the in-plane components, q_1 and q_2 are written as follows

$$\begin{bmatrix} \bar{q}_1(z') \\ \bar{q}_2(z') \end{bmatrix} = -\begin{bmatrix} k_{11}\,p & 0 \\ k_{22}\,q & 0 \end{bmatrix}\begin{bmatrix} \bar{T}(z') \\ \bar{q}_3(z') \end{bmatrix} = -\begin{bmatrix} k_{11}\,p & 0 \\ k_{22}\,q & 0 \end{bmatrix}\begin{bmatrix} f_1 & f_2 \\ g_1 & g_2 \end{bmatrix}\begin{bmatrix} \mathrm{e}^{\eta_1 z'} & 0 \\ 0 & \mathrm{e}^{\eta_2 z'} \end{bmatrix}\begin{bmatrix} d_1 \\ d_2 \end{bmatrix}, \tag{22}$$

with the help of eq. (20). Again, the corresponding general solutions $q_1(x_1,x_2,z',t)$ and $q_2(x_1,x_2,z',t)$ at any desired material point and any time in each plate can straightforwardly be obtained by inserting the sine and cosine terms as well as the time-dependent factor $\mathrm{e}^{i\omega t}$ in eq. (22) with eq. (21).

3.2. Primary elastic solutions for the displacement and traction vectors

Similarly to the thermal contribution, the general elastic displacement vector under time-harmonic motion is expressed as

$$\begin{aligned} u_i\left(x_1,x_2,z',t\right) &= \mathrm{e}^{i\omega t}\sum_{m=1}^{\infty}\sum_{n=1}^{\infty}\begin{bmatrix} \bar{u}_1(z')\cos(px_1)\sin(qx_2) \\ \bar{u}_2(z')\sin(px_1)\cos(qx_2) \\ \bar{u}_3(z')\sin(px_1)\sin(qx_2) \end{bmatrix} \\ &= \mathrm{e}^{i\omega t}\sum_{m=1}^{\infty}\sum_{n=1}^{\infty}\left\{ \mathrm{e}^{sz'}\begin{bmatrix} a_1\cos(px_1)\sin(qx_2) \\ a_2\sin(px_1)\cos(qx_2) \\ a_3\sin(px_1)\sin(qx_2) \end{bmatrix} + f\mathrm{e}^{\eta z'}\begin{bmatrix} r_1\cos(px_1)\sin(qx_2) \\ r_2\sin(px_1)\cos(qx_2) \\ r_3\sin(px_1)\sin(qx_2) \end{bmatrix}\right\}, \end{aligned} \tag{23}$$

where the first part in the double Fourier series decomposition is the elastic homogeneous solution, while the second part is the particular solution of the thermal effect derived in the previous Section 3.1. In eq. (23), the quantity s is the eigenvalue, while a_i are the components of the corresponding eigenvector to be determined as well as the unknown components r_i with respect to the thermal quantities η and f defined in eq. (13). Furthermore, the traction vector t_i is assumed as

$$\begin{aligned} t_i\left(x_1,x_2,z',t\right) &= \mathrm{e}^{i\omega t}\sum_{m=1}^{\infty}\sum_{n=1}^{\infty}\begin{bmatrix} \bar{\sigma}_{31}(z')\cos(px_1)\sin(qx_2) \\ \bar{\sigma}_{32}(z')\sin(px_1)\cos(qx_2) \\ \bar{\sigma}_{33}(z')\sin(px_1)\sin(qx_2) \end{bmatrix} \\ &= \mathrm{e}^{i\omega t}\sum_{m=1}^{\infty}\sum_{n=1}^{\infty}\left\{ \mathrm{e}^{sz'}\begin{bmatrix} b_1\cos(px_1)\sin(qx_2) \\ b_2\sin(px_1)\cos(qx_2) \\ b_3\sin(px_1)\sin(qx_2) \end{bmatrix} + f\mathrm{e}^{\eta z'}\begin{bmatrix} w_1\cos(px_1)\sin(qx_2) \\ w_2\sin(px_1)\cos(qx_2) \\ w_3\sin(px_1)\sin(qx_2) \end{bmatrix}\right\}, \end{aligned} \tag{24}$$

where the four vectors $\{a_i,r_i,b_i,w_i\}=\{\boldsymbol{a},\boldsymbol{r},\boldsymbol{b},\boldsymbol{w}\}$ in eqs. (23) and (24) are written as follows

$$\begin{aligned} \boldsymbol{a} &= \left[a_1,\,a_2,\,a_3\right]^{\mathrm{t}}, \qquad \boldsymbol{r} = \left[r_1,\,r_2,\,r_3\right]^{\mathrm{t}}, \\ \boldsymbol{b} &= \left[b_1,\,b_2,\,b_3\right]^{\mathrm{t}}, \qquad \boldsymbol{w} = \left[w_1,\,w_2,\,w_3\right]^{\mathrm{t}}, \end{aligned} \tag{25}$$

for which nonlocal relations between the expansion coefficients of the displacement and traction vectors can be derived. Substituting eqs. (23) and (24) into eq. (3), the nonlocal constitutive relation for each thermoelastic plate yields

$$\left(1-l_E^2\left(s^2-p^2-q^2\right)\right)\left(\mathrm{e}^{sz'}\boldsymbol{b}+f\mathrm{e}^{\eta z'}\boldsymbol{w}\right) = \mathrm{e}^{sz'}\widetilde{\boldsymbol{b}}+f\mathrm{e}^{\eta z'}\widetilde{\boldsymbol{w}} = \mathrm{e}^{sz'}\left[-\mathbf{R}^{\mathrm{t}}+s\mathbf{T}\right]\boldsymbol{a}+f\mathrm{e}^{\eta z'}\left(\left[-\mathbf{R}^{\mathrm{t}}+\eta\mathbf{T}\right]\boldsymbol{r}-\boldsymbol{k}_2\right), \tag{26}$$

where a tilde, here and in the following, denotes the local quantities since the latter relation is recovered to the traditional Cauchy continuum as the nonlocal length l_E approaches zero. In eq. (26), both involved matrices $\mathbf{R}$ and $\mathbf{T}$ are given by

$$\mathbf{R} = \begin{bmatrix} 0 & 0 & pc_{13} \\ 0 & 0 & qc_{23} \\ -pc_{55} & -qc_{44} & 0 \end{bmatrix}, \tag{27a}$$

$$\mathbf{T} = \begin{bmatrix} c_{55} & 0 & 0 \\ & c_{44} & 0 \\ \text{sym} & & c_{33} \end{bmatrix} = \mathbf{T}^{\mathrm{t}}, \tag{27b}$$

while the vector $\boldsymbol{k}_2$ is defined by

$$\boldsymbol{k}_2 = \left[0,\, 0,\, \beta_{33}\right]^{\mathrm{t}}, \tag{28}$$

exhibiting the thermal effect. Furthermore, introducing eq. (23) into eq. (6), the governing equation of motion reads

$$\begin{aligned} &\mathrm{e}^{sz'}\left[\mathbf{Q} + s\left(\mathbf{R}-\mathbf{R}^{\mathrm{t}}\right) + s^2\,\mathbf{T} + \rho\omega^2\left(1 - l_E^2\left(s^2 - p^2 - q^2\right)\right)\mathbf{I}_{3\times3}\right]\boldsymbol{a} + \quad \ldots \\ &f\mathrm{e}^{\eta z'}\left\{\left[\mathbf{Q} + \eta\left(\mathbf{R}-\mathbf{R}^{\mathrm{t}}\right) + \eta^2\,\mathbf{T} + \rho\omega^2\left(1 - l_E^2\left(\eta^2 - p^2 - q^2\right)\right)\mathbf{I}_{3\times3}\right]\boldsymbol{r} - \boldsymbol{k}_1 - \eta\,\boldsymbol{k}_2\right\} = \mathbf{0}_{3\times1}, \end{aligned} \tag{29}$$

where the involved matrix $\mathbf{Q}$ is defined by

$$\mathbf{Q} = -\begin{bmatrix} p^2c_{11} + q^2c_{66} & pq(c_{12}+c_{66}) & 0 \\ & p^2c_{66} + q^2c_{22} & 0 \\ \text{sym} & & p^2c_{55} + q^2c_{44} \end{bmatrix} = \mathbf{Q}^{\mathrm{t}}, \tag{30}$$

and the subsequent vector $\boldsymbol{k}_1$ by

$$\boldsymbol{k}_1 = \left[p\beta_{11},\, q\beta_{22},\, 0\right]^{\mathrm{t}}, \tag{31}$$

while $\mathbf{I}_{3\times3}$ in eq. (29) is the identity matrix. Thus, according to both eqs. (26) and (29), two individual relations between the vectors in eq. (25) can be formulated by identification as follows

$$\widetilde{\boldsymbol{b}} = \left(1 - l_E^2\left(s^2 - p^2 - q^2\right)\right)\boldsymbol{b} = \left[-\mathbf{R}^{\mathrm{t}} + s\mathbf{T}\right]\boldsymbol{a} = -s^{-1}\left[\mathbf{Q} + \rho\omega^2\left(1 - l_E^2\left(s^2 - p^2 - q^2\right)\right)\mathbf{I}_{3\times3} + s\mathbf{R}\right]\boldsymbol{a}, \tag{32a}$$

$$\widetilde{\boldsymbol{w}} = \left(1 - l_E^2\left(\eta^2 - p^2 - q^2\right)\right)\boldsymbol{w} = \left[-\mathbf{R}^{\mathrm{t}} + \eta\mathbf{T}\right]\boldsymbol{r} - \boldsymbol{k}_2 = -\eta^{-1}\left[\mathbf{Q} + \rho\omega^2\left(1 - l_E^2\left(\eta^2 - p^2 - q^2\right)\right) + \eta\mathbf{R}\right]\boldsymbol{r} + \eta^{-1}\boldsymbol{k}_1, \tag{32b}$$

which can be recast into two quadratic eigenequations, i.e.

$$\left[\widetilde{\mathbf{Q}} + s\left(\mathbf{R}-\mathbf{R}^{\mathrm{t}}\right) + s^2\,\widetilde{\mathbf{T}}\right]\boldsymbol{a} = \mathbf{0}_{3\times1}, \tag{33a}$$

$$\left[\widetilde{\mathbf{Q}} + \eta\left(\mathbf{R}-\mathbf{R}^{\mathrm{t}}\right) + \eta^2\,\widetilde{\mathbf{T}}\right]\boldsymbol{r} - \boldsymbol{k}_1 - \eta\,\boldsymbol{k}_2 = \mathbf{0}_{3\times1}, \tag{33b}$$

where $\widetilde{\mathbf{Q}}$ and $\widetilde{\mathbf{T}}$ are time-harmonic and length-dependent symmetric matrices, given by

$$\widetilde{\mathbf{Q}} = \mathbf{Q} + \rho\omega^2\left(1 + l_E^2\left(p^2 + q^2\right)\right)\mathbf{I}_{3\times3} = \widetilde{\mathbf{Q}}^{\mathrm{t}}, \tag{34a}$$

$$\widetilde{\mathbf{T}} = \mathbf{T} - \rho\omega^2 l_E^2\,\mathbf{I}_{3\times3} = \widetilde{\mathbf{T}}^{\mathrm{t}}, \tag{34b}$$

where $\mathbf{Q}$ and $\mathbf{T}$ are defined in eqs. (30) and (27b), respectively. Finally, eqs. (33) with the help of eqs. (32) can further be converted into the following linear eigensystems of equations

$$\begin{bmatrix} \widetilde{\mathbf{T}}^{-1}\mathbf{R}^{\mathrm{t}} & \widetilde{\mathbf{T}}^{-1} \\ -\widetilde{\mathbf{Q}} - \mathbf{R}\widetilde{\mathbf{T}}^{-1}\mathbf{R}^{\mathrm{t}} & -\mathbf{R}\widetilde{\mathbf{T}}^{-1} \end{bmatrix}\begin{bmatrix} \boldsymbol{a} \\ \widetilde{\boldsymbol{b}} - \rho\omega^2 l_E^2\, s\,\boldsymbol{a} \end{bmatrix} = s\begin{bmatrix} \boldsymbol{a} \\ \widetilde{\boldsymbol{b}} - \rho\omega^2 l_E^2\, s\,\boldsymbol{a} \end{bmatrix}, \tag{35a}$$

$$\begin{bmatrix} \widetilde{\mathbf{T}}^{-1}\mathbf{R}^{\mathrm{t}} & \widetilde{\mathbf{T}}^{-1} \\ -\widetilde{\mathbf{Q}} - \mathbf{R}\widetilde{\mathbf{T}}^{-1}\mathbf{R}^{\mathrm{t}} & -\mathbf{R}\widetilde{\mathbf{T}}^{-1} \end{bmatrix}\begin{bmatrix} \boldsymbol{r} \\ \widetilde{\boldsymbol{w}} - \rho\omega^2 l_E^2\,\eta\,\boldsymbol{r} \end{bmatrix} = \eta\begin{bmatrix} \boldsymbol{r} \\ \widetilde{\boldsymbol{w}} - \rho\omega^2 l_E^2\,\eta\,\boldsymbol{r} \end{bmatrix} - \begin{bmatrix} \mathbf{0}_{3\times3} & \widetilde{\mathbf{T}}^{-1} \\ \mathbf{I}_{3\times3} & -\mathbf{R}\widetilde{\mathbf{T}}^{-1} \end{bmatrix}\begin{bmatrix} \boldsymbol{k}_1 \\ \boldsymbol{k}_2 \end{bmatrix}, \tag{35b}$$

which are defined for any values of ω, l_E, m, and n. Equation (35a) is the extended pseudo-Stroh sextic formalism (Stroh, 1958, 1962, Ting, 1996) that provides a general solution for the generalized plane-strain deformation in a linear anisotropic medium, while eq. (35b) is equivalently solved for the eigenvectors associated to the both thermal roots η_1 and $\eta_2 = -\eta_1$, obtained in eq. (16). Both linear pseudo-Stroh eigensystems in eqs. (35) have a similar structure as in the local and quasi-static ones, which can thus be solved for the six corresponding eigenvalues and eigenvectors. Because the elasticity tensor is positive, these complex quantities appear in complex conjugate pairs (Eshelby et al., 1953) and can be conveniently rearranged such that the first three eigenvalues $\{s_1, s_2, s_3\}$ have positive real parts with $\mathrm{Re}(s_1) \geq \mathrm{Re}(s_2) \geq \mathrm{Re}(s_3)$, while the remaining solutions have opposite signs $\{s_4 = -s_1, s_5 = -s_2, s_6 = -s_3\}$ to the first three eigenvalues. After solving the eigenvalues and eigenvectors of both eigensystems, only the eigenvector parts related to vectors $\boldsymbol{a}$ and $\boldsymbol{r}$ are kept, whereas the additional parts related to vectors $\boldsymbol{b}$ and $\boldsymbol{w}$ are subsequently deduced using eqs. (32a) and (32b), respectively.

Similarly to eq. (20) for the thermal contribution, the general solution for the z'-dependent coefficients of displacement $\bar{u}_i$ and traction $\bar{t}_i$ fields for each layer j can be expressed as

$$\begin{bmatrix} \bar{\boldsymbol{u}}(z') \\ \bar{\boldsymbol{t}}(z') \end{bmatrix} = \begin{bmatrix} \mathbf{A}_{\dagger} & \mathbf{A}_{\dagger\dagger} \\ \mathbf{B}_{\dagger} & \mathbf{B}_{\dagger\dagger} \end{bmatrix}\begin{bmatrix} \langle \mathrm{e}^{\boldsymbol{s}_{\dagger} z'} \rangle & \mathbf{0}_{3\times3} \\ \mathbf{0}_{3\times3} & \langle \mathrm{e}^{\boldsymbol{s}_{\dagger\dagger} z'} \rangle \end{bmatrix}\begin{bmatrix} \boldsymbol{K}_{\dagger} \\ \boldsymbol{K}_{\dagger\dagger} \end{bmatrix} + \begin{bmatrix} \boldsymbol{r}_1 & \boldsymbol{r}_2 \\ \boldsymbol{w}_1 & \boldsymbol{w}_2 \end{bmatrix}\begin{bmatrix} \mathrm{e}^{\eta_1 z'} & 0 \\ 0 & \mathrm{e}^{-\eta_1 z'} \end{bmatrix}\begin{bmatrix} f_1 & 0 \\ 0 & f_2 \end{bmatrix}\begin{bmatrix} d_1 \\ d_2 \end{bmatrix}, \tag{36}$$

where $\boldsymbol{K}_{\dagger}$ and $\boldsymbol{K}_{\dagger\dagger}$ are 3×1 constant column matrices to be determined from the thermomechanical interface boundary conditions, which are also analogous to d_1 and d_2 in eq. (22) from the purely thermal boundary conditions, as described in the Section 4. The six complex eigenvalues $\boldsymbol{s}$ of eq. (35a) and quantities $\boldsymbol{K}$ in eq. (36) are ordered as follows

$$\begin{aligned}
&\boldsymbol{s}_{\dagger} = \left[s_1, s_2, s_3\right]^{\mathrm{t}}, \qquad \boldsymbol{s}_{\dagger\dagger} = \left[s_4, s_5, s_6\right]^{\mathrm{t}}, \\
&\boldsymbol{K}_{\dagger} = \left[K_1, K_2, K_3\right]^{\mathrm{t}}, \quad \boldsymbol{K}_{\dagger\dagger} = \left[K_4, K_5, K_6\right]^{\mathrm{t}},
\end{aligned} \tag{37}$$

and the corresponding 3×3 submatrices are defined as

$$\begin{aligned}
&\mathbf{A}_{\dagger} = \left[\boldsymbol{a}_1, \boldsymbol{a}_2, \boldsymbol{a}_3\right], \quad \mathbf{A}_{\dagger\dagger} = \left[\boldsymbol{a}_4, \boldsymbol{a}_5, \boldsymbol{a}_6\right], \\
&\mathbf{B}_{\dagger} = \left[\boldsymbol{b}_1, \boldsymbol{b}_2, \boldsymbol{b}_3\right], \quad \mathbf{B}_{\dagger\dagger} = \left[\boldsymbol{b}_4, \boldsymbol{b}_5, \boldsymbol{b}_6\right],
\end{aligned} \tag{38}$$

such that $\mathbf{A}_{\dagger}$ and $\mathbf{B}_{\dagger}$ are the collections of eigenvectors associated with the first three eigenvalues $\boldsymbol{s}_{\dagger}$, while $\mathbf{A}_{\dagger\dagger}$ and $\mathbf{B}_{\dagger\dagger}$ are related to the eigenvectors of the eigenvalues $\boldsymbol{s}_{\dagger\dagger}$. In eq. (36), the z'-dependent diagonal and exponential matrices are represented by

$$\langle \mathrm{e}^{\boldsymbol{s}_{\dagger} z'} \rangle = \mathrm{diag}\left[\mathrm{e}^{s_1 z'}, \mathrm{e}^{s_2 z'}, \mathrm{e}^{s_3 z'}\right], \quad \langle \mathrm{e}^{\boldsymbol{s}_{\dagger\dagger} z'} \rangle = \mathrm{diag}\left[\mathrm{e}^{s_4 z'}, \mathrm{e}^{s_5 z'}, \mathrm{e}^{s_6 z'}\right], \tag{39}$$

while both constants f_1 and f_2 are defined in eq. (21). Furthermore, the thermal-related eigenvectors $\boldsymbol{r}_1$ and $\boldsymbol{w}_1$ in eq. (36) correspond to the specific eigenvalue $\eta = \eta_1$, and $\boldsymbol{r}_2$ and $\boldsymbol{w}_2$ to $\eta = \eta_2 = -\eta_1$, which are solved by means of eq. (35b) as

$$\begin{bmatrix} \boldsymbol{r} \\ \widetilde{\boldsymbol{w}} \end{bmatrix} = -\begin{bmatrix} -\widetilde{\mathbf{T}}^{-1}\mathbf{R}^{\mathrm{t}} + \eta\mathbf{I}_{3\times 3} & -\widetilde{\mathbf{T}}^{-1} \\ \widetilde{\mathbf{Q}} + \mathbf{R}\widetilde{\mathbf{T}}^{-1}\mathbf{R}^{\mathrm{t}} & \mathbf{R}\widetilde{\mathbf{T}}^{-1} + \eta\mathbf{I}_{3\times 3} \end{bmatrix}^{-1} \begin{bmatrix} \mathbf{0}_{3\times 3} & \widetilde{\mathbf{T}}^{-1} \\ \mathbf{I}_{3\times 3} & -\mathbf{R}\widetilde{\mathbf{T}}^{-1} \end{bmatrix} \begin{bmatrix} \boldsymbol{k}_1 \\ \boldsymbol{k}_2 \end{bmatrix}, \tag{40}$$

where $\widetilde{\mathbf{Q}}$, $\mathbf{R}$, and $\widetilde{\mathbf{T}}$ are given by eqs. (34) and (27) as well as $\boldsymbol{k}_1$ and $\boldsymbol{k}_2$ by eqs. (31) and eq. (28), respectively.

For each pair of integers m and n, the general solutions of eqs. (23) and (24) for displacement $u_i(x_1, x_2, z', t)$ and traction $t_i(x_1, x_2, z', t)$ fields in each homogenous nonlocal plate are also obtained by introducing the sine and cosine terms as well as the time-dependent factor $\mathrm{e}^{i\omega t}$ in eq. (36) and by solving the aforementioned eigenequations based on the Stroh formalism.

3.3. Secondary elastic solutions for the in-plane stress components

In order to complete the total stress fields, the remaining in-plane stresses τ_i are organized as follows

$$\begin{aligned}
\tau_i\left(x_1, x_2, z', t\right) &= \mathrm{e}^{i\omega t} \sum_{m=1}^{\infty}\sum_{n=1}^{\infty} \begin{bmatrix} \bar{\sigma}_{11}(z')\sin(px_1)\sin(qx_2) \\ \bar{\sigma}_{12}(z')\cos(px_1)\cos(qx_2) \\ \bar{\sigma}_{22}(z')\sin(px_1)\sin(qx_2) \end{bmatrix} \\
&= \mathrm{e}^{i\omega t} \sum_{m=1}^{\infty}\sum_{n=1}^{\infty} \left\{ \mathrm{e}^{sz'} \begin{bmatrix} c_1\sin(px_1)\sin(qx_2) \\ c_2\cos(px_1)\cos(qx_2) \\ c_3\sin(px_1)\sin(qx_2) \end{bmatrix} + f\mathrm{e}^{\eta z'} \begin{bmatrix} v_1\sin(px_1)\sin(qx_2) \\ v_2\cos(px_1)\cos(qx_2) \\ v_3\sin(px_1)\sin(qx_2) \end{bmatrix} \right\},
\end{aligned} \tag{41}$$

which is similarly defined as in eqs. (23) and (24). Substituting the displacement expansion eq. (23) and the in-plane stress eq. (41) into eq. (2), additional explicit relations between the associated expansion coefficients are derived, i.e.

$$\left(1 - l_E^2\left(s^2 - p^2 - q^2\right)\right) \begin{bmatrix} c_1 \\ c_2 \\ c_3 \end{bmatrix} = \begin{bmatrix} -pc_{11} & -qc_{12} & sc_{13} \\ qc_{66} & pc_{66} & 0 \\ -pc_{12} & -qc_{22} & sc_{23} \end{bmatrix} \begin{bmatrix} a_1 \\ a_2 \\ a_3 \end{bmatrix}, \tag{42a}$$

$$\left(1 - l_E^2\left(\eta^2 - p^2 - q^2\right)\right) \begin{bmatrix} v_1 \\ v_2 \\ v_3 \end{bmatrix} = \begin{bmatrix} -pc_{11} & -qc_{12} & \eta c_{13} \\ qc_{66} & pc_{66} & 0 \\ -pc_{12} & -qc_{22} & \eta c_{23} \end{bmatrix} \begin{bmatrix} r_1 \\ r_2 \\ r_3 \end{bmatrix} - \begin{bmatrix} \beta_{11} \\ 0 \\ \beta_{22} \end{bmatrix}, \tag{42b}$$

which are further used to determine the expansion coefficients of the in-plane stress vector. Thus, the solution of the z'-dependent in-plane stresses in eq. (41) is the summation over all the eigenvalues, given by

$$\begin{aligned}
\begin{bmatrix} \bar{\sigma}_{11}(z') \\ \bar{\sigma}_{12}(z') \\ \bar{\sigma}_{22}(z') \end{bmatrix} &= \sum_{i=1}^{6} \frac{1}{1 - l_E^2\left(s_i^2 - p^2 - q^2\right)} \begin{bmatrix} -pc_{11} & -qc_{12} & s_i c_{13} \\ qc_{66} & pc_{66} & 0 \\ -pc_{12} & -qc_{22} & s_i c_{23} \end{bmatrix} \begin{bmatrix} a_{1_i} \\ a_{2_i} \\ a_{3_i} \end{bmatrix} \mathrm{e}^{s_i z'} K_i + \quad \ldots \\
&\sum_{i=1}^{2} \frac{1}{1 - l_E^2\left(\eta_i^2 - p^2 - q^2\right)} f_i d_i \mathrm{e}^{\eta_i z'} \left\{ \begin{bmatrix} -pc_{11} & -qc_{12} & \eta_i c_{13} \\ qc_{66} & pc_{66} & 0 \\ -pc_{12} & -qc_{22} & \eta_i c_{23} \end{bmatrix} \begin{bmatrix} r_{1_i} \\ r_{2_i} \\ r_{3_i} \end{bmatrix} - \begin{bmatrix} p\beta_{11} \\ 0 \\ q\beta_{22} \end{bmatrix} \right\},
\end{aligned} \tag{43}$$

where $\mathrm{e}^{s_i z'} K_i$ can be obtained by using the expression of the displacement vector in eq. (36), so that

$$\begin{bmatrix} \langle \mathrm{e}^{\boldsymbol{s}_1 z'} \rangle \boldsymbol{K}_{\dagger} \\ \langle \mathrm{e}^{\boldsymbol{s}_2 z'} \rangle \boldsymbol{K}_{\dagger\dagger} \end{bmatrix} = \begin{bmatrix} \mathbf{A}_{\dagger} & \mathbf{A}_{\dagger\dagger} \\ \mathbf{B}_{\dagger} & \mathbf{B}_{\dagger\dagger} \end{bmatrix}^{-1} \begin{bmatrix} \bar{\boldsymbol{u}}(z') \\ \bar{\boldsymbol{t}}(z') \end{bmatrix} - \begin{bmatrix} \mathbf{A}_{\dagger} & \mathbf{A}_{\dagger\dagger} \\ \mathbf{B}_{\dagger} & \mathbf{B}_{\dagger\dagger} \end{bmatrix}^{-1} \begin{bmatrix} \boldsymbol{r}_1 & \boldsymbol{r}_2 \\ \boldsymbol{w}_1 & \boldsymbol{w}_2 \end{bmatrix} \begin{bmatrix} f_1 d_1 \mathrm{e}^{\eta_1 z'} \\ f_2 d_2 \mathrm{e}^{-\eta_1 z'} \end{bmatrix}, \tag{44}$$

while $d_i \mathrm{e}^{\eta_i z'}$ is given by eq. (20) as follows

$$\begin{bmatrix} \mathrm{e}^{\eta_1 z'} d_1 \\ \mathrm{e}^{-\eta_1 z'} d_2 \end{bmatrix} = \begin{bmatrix} f_1 & f_2 \\ g_1 & g_2 \end{bmatrix}^{-1} \begin{bmatrix} \bar{T}(z') \\ \bar{q}_3(z') \end{bmatrix} = \left(1 - l_T^2 \left(\eta^2 - p^2 - q^2\right)\right) \begin{bmatrix} -g_2 & f_2 \\ g_1 & -f_1 \end{bmatrix} \begin{bmatrix} \bar{T}(z) \\ \bar{q}_3(z) \end{bmatrix}, \tag{45}$$

within which the inverse of the specific matrix of thermal eigenvectors is explicitly defined by

$$\begin{bmatrix} f_1 & f_2 \\ g_1 & g_2 \end{bmatrix}^{-1} = \left(1 - l_T^2 \left(\eta^2 - p^2 - q^2\right)\right) \begin{bmatrix} -g_2 & f_2 \\ g_1 & -f_1 \end{bmatrix}, \tag{46}$$

and the corresponding components by eq. (21). Again, the general solutions for the in-plane stress components $\tau_i(x_1, x_2, z', t)$ in eq. (41) are obtained for each homogeneous Eringen nonlocal plate by considering the sine and cosine terms as well as the time-dependent factor $\mathrm{e}^{i\omega t}$ in eq. (43). Importantly, eqs. (41) and (43) show that once the temperature, the normal heat flux, the displacement and traction vectors are known, the remaining in-plane stress field components are inherently provided by algebraic operations.

4. Recursive field relations for multilayered plates with imperfect interfaces

Combined with the previous pseudo-Stroh formalism using the Eringen nonlocal thermoelasticity, two recursive techniques, namely the transfer matrix and the dual variable and position techniques, are formulated to determine the local relations between field quantities at both opposite interfaces of each individual plate, and then propagate the corresponding solutions recursively, but differently, through all layers. While the forward propagation from the bottom to the top surfaces is performed in the first method, a mixed forward and backward propagation of solutions is subsequently introduced in the second technique, as described in Sections 4.1 and 4.2, respectively. Numerical comparison and differences that emerge from these two approaches are shown and discussed in the application Section 5. In the following, general conditions for imperfect interfaces are included in both recursive approaches. For the sake of clarity, because only the z'-dependent field expressions from the former solutions are needed to derive the diverse propagation and imperfect matrices using algebraic manipulations, the sine and cosine functions of x_1 and x_2 as well as the time-dependent factor $\mathrm{e}^{i\omega t}$ are conveniently omitted. The physical quantities are then straightforwardly appended to determine the final recursive relations.

4.1. Approach I: The transfer matrix technique

The first procedure to determine the thermoelastic vibration responses of irregularly multilayered plates is based on the transfer matrix method (Gilbert and Bachus, 1966, Pan, 2001). In practice, the technique consists first in transferring the general field solutions derived in the eqs. (20) and (36) from the bottom of each homogeneous plate j at z_j to the upper surface at z_{j+1}. The forwarding thermoelastic solutions are then conveniently reformulated in terms of the propagating matrix relations to analyze the global multilayered system by means of specific boundary conditions across the internal interfaces. The coefficients in the corresponding series expansions are identified using the specific boundary conditions at the external surfaces as well as the internal interfaces described in Section 2.2.

4.1.1. Single-layer propagation matrix

The z'-dependent thermal solutions for any layer j of thickness h_j can be specified in the local coordinate system with respect to the top interface at $z' = z_{j+1} = h_j$, as follows

$$\begin{bmatrix} \bar{T}(z') \\ \bar{q}_3(z') \end{bmatrix}_{z'=z_{j+1}} = \begin{bmatrix} f_1 & f_2 \\ g_1 & g_2 \end{bmatrix} \begin{bmatrix} \mathrm{e}^{\eta_1 h_j} & 0 \\ 0 & \mathrm{e}^{-\eta_1 h_j} \end{bmatrix} \begin{bmatrix} d_1 \\ d_2 \end{bmatrix}_j, \tag{47}$$

according to eq. (20), with $\eta_2 = -\eta_1$. On the other hand, when the thermal solutions are set to the lower interface at $z' = z_j = 0$, the unknown thermal constants in eq. (20) are reduced to

$$\begin{bmatrix} d_1 \\ d_2 \end{bmatrix}_j = \begin{bmatrix} f_1 & f_2 \\ g_1 & g_2 \end{bmatrix}^{-1} \begin{bmatrix} \bar{T}(z') \\ \bar{q}_3(z') \end{bmatrix}_{z'=z_j}, \tag{48}$$

so that combining eq. (47) with eq. (48) yields the major propagation relation for the thermal part, as

$$\begin{bmatrix} \bar{T}(z') \\ \bar{q}_3(z') \end{bmatrix}_{z'=z_{j+1}} = \begin{bmatrix} f_1 & f_2 \\ g_1 & g_2 \end{bmatrix} \begin{bmatrix} \mathrm{e}^{\eta_1 h_j} & 0 \\ 0 & \mathrm{e}^{-\eta_1 h_j} \end{bmatrix} \begin{bmatrix} f_1 & f_2 \\ g_1 & g_2 \end{bmatrix}^{-1} \begin{bmatrix} \bar{T}(z') \\ \bar{q}_3(z') \end{bmatrix}_{z'=z_j}, \tag{49}$$

which links the local temperature and the normal heat flux from the bottom to the top surface for each individual plate. Furthermore, substituting the thermal unknowns d_1 and d_2 from eq. (47) into eq. (36), the vectors $\boldsymbol{K}_{\dagger}$ and $\boldsymbol{K}_{\dagger\dagger}$ can be expressed as follows

$$\begin{bmatrix}\boldsymbol{K}_{\dagger}\\ \boldsymbol{K}_{\dagger\dagger}\end{bmatrix}_j = \begin{bmatrix}\mathbf{A}_{\dagger} & \mathbf{A}_{\dagger\dagger}\\ \mathbf{B}_{\dagger} & \mathbf{B}_{\dagger\dagger}\end{bmatrix}^{-1}\begin{bmatrix}\bar{\boldsymbol{u}}(z')\\ \bar{\boldsymbol{t}}(z')\end{bmatrix}_{z'=z_j} - \begin{bmatrix}\mathbf{A}_{\dagger} & \mathbf{A}_{\dagger\dagger}\\ \mathbf{B}_{\dagger} & \mathbf{B}_{\dagger\dagger}\end{bmatrix}^{-1}\begin{bmatrix}\boldsymbol{r}_1 & \boldsymbol{r}_2\\ \boldsymbol{w}_1 & \boldsymbol{w}_2\end{bmatrix}\begin{bmatrix}f_1 & 0\\ 0 & f_2\end{bmatrix}\begin{bmatrix}\mathrm{e}^{-\eta_1 h_j} & 0\\ 0 & \mathrm{e}^{\eta_1 h_j}\end{bmatrix}\begin{bmatrix}f_1 & f_2\\ g_1 & g_2\end{bmatrix}^{-1}\begin{bmatrix}\bar{T}(z')\\ \bar{q}_3(z')\end{bmatrix}_{z'=z_{j+1}}, \tag{50}$$

establishing an intermediate equation between the elastic quantities at the bottom surface and the thermal solutions at the top surface. After algebraic manipulation that consists in setting $z'=z_{j+1}$ in eq. (36) and then substituting the result into eq. (50) with the help of eqs. (46), (47) and (49), the subsequent propagation relation for the mechanical part is given by

$$\begin{aligned}\begin{bmatrix}\bar{\boldsymbol{u}}(z')\\ \bar{\boldsymbol{t}}(z')\end{bmatrix}_{z'=z_{j+1}} &= \begin{bmatrix}\mathbf{A}_{\dagger} & \mathbf{A}_{\dagger\dagger}\\ \mathbf{B}_{\dagger} & \mathbf{B}_{\dagger\dagger}\end{bmatrix}\begin{bmatrix}\left\langle \mathrm{e}^{\boldsymbol{s}_{\dagger}h_j}\right\rangle & \mathbf{0}_{3\times3}\\ \mathbf{0}_{3\times3} & \left\langle \mathrm{e}^{\boldsymbol{s}_{\dagger\dagger}h_j}\right\rangle\end{bmatrix}\begin{bmatrix}\mathbf{A}_{\dagger} & \mathbf{A}_{\dagger\dagger}\\ \mathbf{B}_{\dagger} & \mathbf{B}_{\dagger\dagger}\end{bmatrix}^{-1}\begin{bmatrix}\bar{\boldsymbol{u}}(z')\\ \bar{\boldsymbol{t}}(z')\end{bmatrix}_{z'=z_j} \quad \cdots\\ &\quad -\left(1-l_T^2\left(\eta^2-p^2-q^2\right)\right)\begin{bmatrix}\boldsymbol{r}_1 & \boldsymbol{r}_2\\ \boldsymbol{w}_1 & \boldsymbol{w}_2\end{bmatrix}\begin{bmatrix}f_1g_2\,\mathrm{e}^{\eta_1 h_j} & -f_1f_2\,\mathrm{e}^{\eta_1 h_j}\\ -f_2g_1\,\mathrm{e}^{-\eta_1 h_j} & f_1f_2\,\mathrm{e}^{-\eta_1 h_j}\end{bmatrix}\begin{bmatrix}\bar{T}(z')\\ \bar{q}_3(z')\end{bmatrix}_{z'=z_j} \quad \cdots\\ &\quad -\left(1-l_T^2\left(\eta^2-p^2-q^2\right)\right)\begin{bmatrix}\mathbf{A}_{\dagger} & \mathbf{A}_{\dagger\dagger}\\ \mathbf{B}_{\dagger} & \mathbf{B}_{\dagger\dagger}\end{bmatrix}\begin{bmatrix}\left\langle \mathrm{e}^{\boldsymbol{s}_{\dagger}h_j}\right\rangle & \mathbf{0}_{3\times3}\\ \mathbf{0}_{3\times3} & \left\langle \mathrm{e}^{\boldsymbol{s}_{\dagger\dagger}h_j}\right\rangle\end{bmatrix}\begin{bmatrix}\mathbf{A}_{\dagger} & \mathbf{A}_{\dagger\dagger}\\ \mathbf{B}_{\dagger} & \mathbf{B}_{\dagger\dagger}\end{bmatrix}^{-1}\begin{bmatrix}\boldsymbol{r}_1 & \boldsymbol{r}_2\\ \boldsymbol{w}_1 & \boldsymbol{w}_2\end{bmatrix}\begin{bmatrix}-f_1g_2 & f_1f_2\\ f_2g_1 & -f_1f_2\end{bmatrix}\begin{bmatrix}\bar{T}(z')\\ \bar{q}_3(z')\end{bmatrix}_{z'=z_j},\end{aligned} \tag{51}$$

where the two last contributions evidence the thermal coupling part to elasticity. Both eqs. (49) and (51) can together be combined to obtain the specific and concise relation between the thermomechanical solutions at the lower and upper surfaces for any homogeneous layer j, as follows

$$\begin{bmatrix}\bar{\boldsymbol{u}}(z')\\ \bar{\boldsymbol{t}}(z')\\ \bar{T}(z')\\ \bar{q}_3(z')\end{bmatrix}_{z'=z_{j+1}} = \begin{bmatrix}\begin{bmatrix}\mathbf{E}_{11} & \mathbf{E}_{12}\\ \mathbf{E}_{21} & \mathbf{E}_{22}\end{bmatrix} & \begin{bmatrix}\boldsymbol{L}_{11} & \boldsymbol{L}_{12}\\ \boldsymbol{L}_{21} & \boldsymbol{L}_{22}\end{bmatrix}\\ \mathbf{0}_{2\times6} & \begin{bmatrix}F_{11} & F_{12}\\ F_{21} & F_{22}\end{bmatrix}\end{bmatrix}_j\begin{bmatrix}\bar{\boldsymbol{u}}(z')\\ \bar{\boldsymbol{t}}(z')\\ \bar{T}(z')\\ \bar{q}_3(z')\end{bmatrix}_{z'=z_j} = \mathbf{P}_j(h_j)\begin{bmatrix}\bar{\boldsymbol{u}}(z')\\ \bar{\boldsymbol{t}}(z')\\ \bar{T}(z')\\ \bar{q}_3(z')\end{bmatrix}_{z'=z_j}, \tag{52}$$

where $\mathbf{P}_j(h_j)$ is the transfer matrix function of the finite thickness h_j, and the submatrices are given by

$$\begin{bmatrix}\mathbf{E}_{11} & \mathbf{E}_{12}\\ \mathbf{E}_{21} & \mathbf{E}_{22}\end{bmatrix}_{6\times6} = \begin{bmatrix}\mathbf{A}_{\dagger} & \mathbf{A}_{\dagger\dagger}\\ \mathbf{B}_{\dagger} & \mathbf{B}_{\dagger\dagger}\end{bmatrix}\begin{bmatrix}\left\langle \mathrm{e}^{\boldsymbol{s}_{\dagger}h_j}\right\rangle & \mathbf{0}_{3\times3}\\ \mathbf{0}_{3\times3} & \left\langle \mathrm{e}^{\boldsymbol{s}_{\dagger\dagger}h_j}\right\rangle\end{bmatrix}\begin{bmatrix}\mathbf{A}_{\dagger} & \mathbf{A}_{\dagger\dagger}\\ \mathbf{B}_{\dagger} & \mathbf{B}_{\dagger\dagger}\end{bmatrix}^{-1}, \tag{53a}$$

$$\begin{bmatrix}\boldsymbol{L}_{11} & \boldsymbol{L}_{12}\\ \boldsymbol{L}_{21} & \boldsymbol{L}_{22}\end{bmatrix}_{6\times2} = -\left(1-l_T^2\left(\eta^2-p^2-q^2\right)\right)\left\{\begin{bmatrix}\boldsymbol{r}_1 & \boldsymbol{r}_2\\ \boldsymbol{w}_1 & \boldsymbol{w}_2\end{bmatrix}\begin{bmatrix}f_1g_2\,\mathrm{e}^{\eta_1 h_j} & -f_1f_2\,\mathrm{e}^{\eta_1 h_j}\\ -f_2g_1\,\mathrm{e}^{-\eta_1 h_j} & f_1f_2\,\mathrm{e}^{-\eta_1 h_j}\end{bmatrix} + \begin{bmatrix}\mathbf{E}_{11} & \mathbf{E}_{12}\\ \mathbf{E}_{21} & \mathbf{E}_{22}\end{bmatrix}\begin{bmatrix}\boldsymbol{r}_1 & \boldsymbol{r}_2\\ \boldsymbol{w}_1 & \boldsymbol{w}_2\end{bmatrix}\begin{bmatrix}-f_1g_2 & f_1f_2\\ f_2g_1 & -f_1f_2\end{bmatrix}\right\}, \tag{53b}$$

$$\begin{bmatrix}F_{11} & F_{12}\\ F_{21} & F_{22}\end{bmatrix}_{2\times2} = \left(1-l_T^2\left(\eta^2-p^2-q^2\right)\right)\begin{bmatrix}f_1 & f_2\\ g_1 & g_2\end{bmatrix}\begin{bmatrix}\mathrm{e}^{\eta_1 h_j} & 0\\ 0 & \mathrm{e}^{-\eta_1 h_j}\end{bmatrix}\begin{bmatrix}-g_2 & f_2\\ g_1 & -f_1\end{bmatrix}, \tag{53c}$$

which are uniquely defined for any laminate with specific homogeneous nonlocal elastic and thermal properties as well as specific geometrical characteristics.

4.1.2. Thermomechanical interface matrix

By virtue of the various interface boundary conditions from Section 2.2.2, the interface between two adjacent layers at $z'=z_k$ is considered, within which perfect/imperfect thermal and mechanical properties are described by introducing the general 8×8 interface matrix $\mathbf{Z}_k$, as follows

$$\begin{bmatrix}\bar{\boldsymbol{u}}(z')\\ \bar{\boldsymbol{t}}(z')\\ \bar{T}(z')\\ \bar{q}_3(z')\end{bmatrix}_{z'=z_k^+} = \mathbf{Z}_k\begin{bmatrix}\bar{\boldsymbol{u}}(z')\\ \bar{\boldsymbol{t}}(z')\\ \bar{T}(z')\\ \bar{q}_3(z')\end{bmatrix}_{z'=z_k^-} = \begin{bmatrix}\mathbf{Z}_E & \mathbf{0}_{6\times2}\\ \mathbf{0}_{2\times6} & \mathbf{Z}_T^{\eta}\end{bmatrix}_k\begin{bmatrix}\bar{\boldsymbol{u}}(z')\\ \bar{\boldsymbol{t}}(z')\\ \bar{T}(z')\\ \bar{q}_3(z')\end{bmatrix}_{z'=z_k^-}, \tag{54}$$

where the sine and cosine terms as well as the factor $\mathrm{e}^{i\omega t}$ in the field solutions have been omitted, for convenience. In eq. (54), both locations z_k^- and z_k^+ denote the lower and upper sides of the interface, respectively, while the coupling submatrices $\mathbf{Z}_E$ and $\mathbf{Z}_T^{\eta}$ are related to the mechanical and thermal interface properties, respectively. In particular, the symbol η with binary values $\{0,1\}$ reflects the two different types of thermally conductive interfaces introduced in Section 2.2.2, where $\eta=0$ is associated with the specific conditions for weakly conducting interfaces, and $\eta=1$ with highly conducting interfaces.

According to eq. (10), the mechanical compliance condition at interfaces can be expressed as follows

$$\mathbf{Z}_E = \begin{bmatrix} \mathbf{I}_{3\times3} & \operatorname{diag}\left[\alpha_1^{(k)}, \alpha_2^{(k)}, \alpha_3^{(k)}\right] \\ \mathbf{0}_{3\times3} & \mathbf{I}_{3\times3} \end{bmatrix}, \tag{55}$$

for which the continuity of the elastic displacement and traction vectors can be prescribed when all components $\alpha_i^{(k)} = 0$, so that eq. (55) can be reduced to the idealistic mechanical condition for all perfectly bonded interfaces. On the other hand, the thermally imperfect matrix is defined by

$$\mathbf{Z}_T^{\eta} = (1-\eta)\,\mathbf{Z}_T^{-} + \eta\,\mathbf{Z}_T^{+}, \tag{56}$$

which is therefore used to distinguish thermal insulation or high heat conduction properties of interfaces. Thus, the thermally weakly conducting interface, described by a discontinuous temperature, is formally rewritten from eq. (11) by using the following interfacial matrix, i.e.

$$\mathbf{Z}_T^0 = \mathbf{Z}_T^{-} = \begin{bmatrix} 1 & -\beta_T^{(k)} \\ 0 & 1 \end{bmatrix}, \tag{57}$$

while the highly conducting interface, characterized by a discontinuous jump in the normal heat flux across the interface in eq. (12), is defined by

$$\mathbf{Z}_T^1 = \mathbf{Z}_T^{+} = \begin{bmatrix} 1 & 0 \\ -\gamma_T^{(k)}\left(p_m^2 + q_n^2\right) & 1 \end{bmatrix}, \tag{58}$$

where one component depends explicitly on p_m and q_n, consequently on m and n. It is worth mentioning that all $\mathbf{Z}$-matrices in eqs. (55), (57) and (58) are uniquely defined for the k^{th} internal interface. In other words, there are as many anisotropic interfacial properties that can be different from each other as there are imperfect interfaces in a given multilayered plate.

4.1.3. Forward recursive field solutions in multilayers

The recursive transfer matrix method for multilayered solids with general boundary conditions at all internal interfaces between adjacent materials can be formulated by applying eq. (52) combined with eq. (54) repeatedly through successive layers. In the global coordinate system, the propagation relation between the physical displacement, traction, temperature, and normal heat flux components on the bottom and top surfaces for any arbitrary multilayers in presence of perfect/imperfect internal interfaces is therefore given by

$$\begin{bmatrix} \bar{\boldsymbol{u}}(z) \\ \bar{\boldsymbol{t}}(z) \\ \bar{T}(z) \\ \bar{q}_3(z) \end{bmatrix}_{z=H} = \underbrace{\left(\prod_{j=2}^{N} \mathbf{P}_j(h_j)\,\mathbf{Z}_j\right)\mathbf{P}_1(h_1)}_{=\mathbf{N}_{8\times8}} \begin{bmatrix} \bar{\boldsymbol{u}}(z) \\ \bar{\boldsymbol{t}}(z) \\ \bar{T}(z) \\ \bar{q}_3(z) \end{bmatrix}_{z=0} = \begin{bmatrix} \begin{bmatrix} \mathbf{N}_{11} & \mathbf{N}_{12} \\ \mathbf{N}_{21} & \mathbf{N}_{22} \end{bmatrix} & \begin{bmatrix} \boldsymbol{N}_{13} & \boldsymbol{N}_{14} \\ \boldsymbol{N}_{23} & \boldsymbol{N}_{24} \end{bmatrix} \\ \mathbf{0}_{2\times6} & \begin{bmatrix} N_{33} & N_{34} \\ N_{43} & N_{44} \end{bmatrix} \end{bmatrix} \begin{bmatrix} \bar{\boldsymbol{u}}(z) \\ \bar{\boldsymbol{t}}(z) \\ \bar{T}(z) \\ \bar{q}_3(z) \end{bmatrix}_{z=0}, \tag{59}$$

for which the internal interfaces are defined for $j > 1$. In eq. (59), the global 8×8 matrix $\mathbf{N}$ contains specific submatrices as a result of the product of the local transfer matrices by the corresponding interface matrices. In particular, for ideal description of multilayered structures with perfect interfaces, $\forall j : \mathbf{Z}_j = \mathbf{I}_{8\times8}$, such that $\mathbf{N}$ transfers successively the field solutions by satisfying the continuity of all components.

A similar propagation relation for the field quantities as eq. (59) from the bottom surface to any location z_f in plate j of a multilayered laminate can merely be expressed as follows

$$\begin{bmatrix} \bar{\boldsymbol{u}}(z_f) \\ \bar{\boldsymbol{t}}(z_f) \\ \bar{T}(z_f) \\ \bar{q}_3(z_f) \end{bmatrix}_{z_j \le z_f \le z_{j+1}} = \mathbf{P}_j(z_f - z_{j-1})\,\mathbf{Z}_j \times \mathbf{P}_{j-1}(h_{j-1})\,\mathbf{Z}_{j-1} \times \ldots \times \mathbf{P}_2(h_2)\,\mathbf{Z}_2 \times \mathbf{P}_1(h_1) \begin{bmatrix} \bar{\boldsymbol{u}}(z) \\ \bar{\boldsymbol{t}}(z) \\ \bar{T}(z) \\ \bar{q}_3(z) \end{bmatrix}_{z=0}, \tag{60}$$

where the field quantities on the right-hand side at $z = 0$ can be rewritten to meet the external boundary conditions described in Section 2.2.1. By means of the prescribed mechanical tractions $\bar{\boldsymbol{t}}_{mn}^B$ and $\bar{\boldsymbol{t}}_{mn}^T$ as well as temperatures $\bar{T}_{mn}^B$ and $\bar{T}_{mn}^T$ applied on both the bottom and top surfaces at $z = 0$ and $z = H$, as described by eqs. (8) and (9), respectively, eq. (59) yields a set of eight equations with eight unknowns, namely

$$\begin{cases} \bar{\boldsymbol{u}}(H) = \mathbf{N}_{11}\,\bar{\boldsymbol{u}}(0) + \mathbf{N}_{12}\,\bar{\boldsymbol{t}}_{mn}^B + \boldsymbol{N}_{13}\,\bar{T}_{mn}^B + \boldsymbol{N}_{14}\,\bar{q}_3(0), & \text{(61a)} \\ \bar{\boldsymbol{t}}_{mn}^T = \mathbf{N}_{21}\,\bar{\boldsymbol{u}}(0) + \mathbf{N}_{22}\,\bar{\boldsymbol{t}}_{mn}^B + \boldsymbol{N}_{23}\,\bar{T}_{mn}^B + \boldsymbol{N}_{24}\,\bar{q}_3(0), & \text{(61b)} \\ \bar{T}_{mn}^T = N_{33}\,\bar{T}_{mn}^B + N_{34}\,\bar{q}_3(0), & \text{(61c)} \\ \bar{q}_3(H) = N_{43}\,\bar{T}_{mn}^B + N_{44}\,\bar{q}_3(0), & \text{(61d)} \end{cases}$$

for which the solutions of $\bar{\boldsymbol{u}}(0)$ and $\bar{q}_3(0)$ can be uniquely determined by considering eqs. (61b), (61c) and (61d). Thus, substituting the latter fields into eq. (60), the exact closed-form solution for the displacement and traction vectors as well as the temperature and normal heat flux are defined at any position z_f within the j^{th} plate by

$$\begin{bmatrix} \bar{\boldsymbol{u}}(z_f) \\ \bar{\boldsymbol{t}}(z_f) \\ \bar{T}(z_f) \\ \bar{q}_3(z_f) \end{bmatrix}_{z_j \le z_f \le z_{j+1}} = \mathbf{P}_j(z_f - z_{j-1}) \mathbf{Z}_j \left(\prod_{k=2}^{j-1} \mathbf{P}_k(h_k) \mathbf{Z}_k \right) \mathbf{P}_1(h_1) \begin{bmatrix} \mathbf{N}_{21}^{-1} \left[\bar{\boldsymbol{t}}_{mn}^T - \mathbf{N}_{22} \bar{\boldsymbol{t}}_{mn}^B - \boldsymbol{N}_{23} \bar{T}_{mn}^B - N_{34}^{-1} \boldsymbol{N}_{24} \left(\bar{T}_{mn}^T - N_{33} \bar{T}_{mn}^B \right) \right] \\ \bar{\boldsymbol{t}}_{mn}^B \\ \bar{T}_{mn}^B \\ N_{34}^{-1} \left(\bar{T}_{mn}^T - N_{33} \bar{T}_{mn}^B \right) \end{bmatrix}_{z=0}, \tag{62}$$

where the remaining in-plane stress components $\bar{\boldsymbol{\tau}}(z_f)$ are deduced using eqs. (43 – 46). Finally, the corresponding physical solutions with respect to (x_1, x_2, x_3) and time t are straightforwardly obtained by introducing in eq. (62) the double sums of infinite sine and cosine series over m and n as well as the time-dependent factor $\mathrm{e}^{i\omega t}$ assigned to eqs. (13), (23) and (24), thus without modifying the intrinsic transfer and interface matrices. In Section 5, several Fourier expansion amplitudes for specific prescribed temperature and tractions used in eq. (62) are explicitly written for various application examples.

4.2. Approach II: The dual variable and position technique

The dual variable and position procedure combined with the Stroh formalism (Liu et al., 2018), inspired from the extended precise integration method (Ai and Cheng, 2014), is subsequently used to propagate the vectorial solutions among different layers. The main operation consists of avoiding critical positive signs in the exponential Fourier series derived in Section 3, which leads to i) divergence-free solutions without spurious oscillations for large amplitudes of frequencies or half-wave numbers, and to ii) a computational cost similar to the first transfert matrix technique with high accuracy. The single-layer transfer matrix in eq. (52) is used to assemble field solutions and further to determine alternative recursive relations in multilayered structures including imperfect interfaces. Here again, the series expansion coefficients are formulated with respect to the specific boundary conditions applied at the external surfaces.

4.2.1. Dual variable and position matrix for each homogeneous plate

In the following, eq. (52) is conveniently reordered to harmonize the dimensions of the submatrices in the transfer matrix $\mathbf{P}_j$ as follows

$$\begin{bmatrix} \bar{\boldsymbol{u}}(z') \\ \bar{T}(z') \\ \bar{\boldsymbol{t}}(z') \\ \bar{q}_3(z') \end{bmatrix}_{z'=z_{j+1}} = \underline{\mathbf{P}}_j(h_j) \begin{bmatrix} \bar{\boldsymbol{u}}(z') \\ \bar{T}(z') \\ \bar{\boldsymbol{t}}(z') \\ \bar{q}_3(z') \end{bmatrix}_{z'=z_j} = \begin{bmatrix} \underline{\mathbf{P}}_{11} & \underline{\mathbf{P}}_{12} \\ \underline{\mathbf{P}}_{21} & \underline{\mathbf{P}}_{22} \end{bmatrix}_j \begin{bmatrix} \bar{\boldsymbol{u}}(z') \\ \bar{T}(z') \\ \bar{\boldsymbol{t}}(z') \\ \bar{q}_3(z') \end{bmatrix}_{z'=z_j}, \tag{63}$$

where the underbar notation stands for the corresponding rearrangement of field solutions. In eq. (63), the 4×4 submatrices $\underline{\mathbf{P}}_{\xi\delta}$ are explicitly obtained by straightforward permutation and are also defined by

$$\underline{\mathbf{P}}_{\xi\delta} = \begin{bmatrix} \mathbf{E}_{\xi\delta} & \boldsymbol{L}_{\xi\delta} \\ \mathbf{0}_{1\times3} & F_{\xi\delta} \end{bmatrix}, \tag{64}$$

where the Greek subscripts ξ and δ take on the values 1 and 2, accordingly to eq. (52). Furthermore, two adequate 4×1 vectors $\bar{\boldsymbol{u}}_{\bar{T}}$ and $\bar{\boldsymbol{t}}_{\bar{q}}$ are introduced for reasons of clarity, such that eq. (63) reads

$$\begin{bmatrix} \bar{\boldsymbol{u}}_{\bar{T}}(z') \\ \bar{\boldsymbol{t}}_{\bar{q}}(z') \end{bmatrix}_{z'=z_{j+1}} = \begin{bmatrix} \underline{\mathbf{P}}_{11} & \underline{\mathbf{P}}_{12} \\ \underline{\mathbf{P}}_{21} & \underline{\mathbf{P}}_{22} \end{bmatrix}_j \begin{bmatrix} \bar{\boldsymbol{u}}_{\bar{T}}(z') \\ \bar{\boldsymbol{t}}_{\bar{q}}(z') \end{bmatrix}_{z'=z_j}, \quad \text{with} : \begin{cases} \bar{\boldsymbol{u}}_{\bar{T}}(z') = \left[\bar{\boldsymbol{u}}(z'), \bar{T}(z') \right]^{\mathrm{t}} \\ \bar{\boldsymbol{t}}_{\bar{q}}(z') = \left[\bar{\boldsymbol{t}}(z'), \bar{q}_3(z') \right]^{\mathrm{t}}, \end{cases} \tag{65}$$

and the cross field solutions at $z' = z_j$ and $z' = z_{j+1}$ are obviously related to each other by

$$\begin{bmatrix} \bar{\boldsymbol{u}}_{\bar{T}}(z_j) \\ \bar{\boldsymbol{t}}_{\bar{q}}(z_{j+1}) \end{bmatrix} = \begin{bmatrix} \underline{\mathbf{P}}_{11} & \mathbf{0}_{4\times4} \\ -\underline{\mathbf{P}}_{21} & \mathbf{I}_{4\times4} \end{bmatrix}_j^{-1} \begin{bmatrix} \mathbf{I}_{4\times4} & -\underline{\mathbf{P}}_{12} \\ \mathbf{0}_{4\times4} & \underline{\mathbf{P}}_{22} \end{bmatrix}_j \begin{bmatrix} \bar{\boldsymbol{u}}_{\bar{T}}(z_{j+1}) \\ \bar{\boldsymbol{t}}_{\bar{q}}(z_j) \end{bmatrix} = \begin{bmatrix} \underline{\mathbf{P}}_{11}^{-1} & -\underline{\mathbf{P}}_{11}^{-1}\underline{\mathbf{P}}_{12} \\ \underline{\mathbf{P}}_{21}\underline{\mathbf{P}}_{11}^{-1} & -\underline{\mathbf{P}}_{21}\underline{\mathbf{P}}_{11}^{-1}\underline{\mathbf{P}}_{12} + \underline{\mathbf{P}}_{22} \end{bmatrix}_j \begin{bmatrix} \bar{\boldsymbol{u}}_{\bar{T}}(z_{j+1}) \\ \bar{\boldsymbol{t}}_{\bar{q}}(z_j) \end{bmatrix} = \mathbf{V}_{8\times8}^j \begin{bmatrix} \bar{\boldsymbol{u}}_{\bar{T}}(z_{j+1}) \\ \bar{\boldsymbol{t}}_{\bar{q}}(z_j) \end{bmatrix}, \tag{66}$$

where $\mathbf{V}_{8\times8}^j$ is the dual variable and position matrix with components that are related to the transfer submatrices as follows

$$\begin{aligned} \mathbf{V}_{11}^j &= \left[\underline{\mathbf{P}}_{11}^{-1} \right]_j, & \mathbf{V}_{12}^j &= \left[-\underline{\mathbf{P}}_{11}^{-1}\underline{\mathbf{P}}_{12} \right]_j, \\ \mathbf{V}_{21}^j &= \left[\underline{\mathbf{P}}_{21}\underline{\mathbf{P}}_{11}^{-1} \right]_j, & \mathbf{V}_{22}^j &= \left[-\underline{\mathbf{P}}_{21}\underline{\mathbf{P}}_{11}^{-1}\underline{\mathbf{P}}_{12} + \underline{\mathbf{P}}_{22} \right]_j, \end{aligned} \tag{67}$$

for any plate j bonded by the lower interface at z_j and the upper interface at z_{j+1}. The iterative procedure is established by considering the similar sequence for the adjacent layer $j-1$ bounded by both interfaces at $z' = z_{j-1}$ and $z' = z_j$, and by making use of the continuity

conditions of the expansion coefficients at $z' = z_j$. Thus, the recursive relation that propagates the thermoelastic solutions from the bottom interface of $j-1^{\text{th}}$ layer to the upper interface of the adjacent j^{th} layer is given by

$$\begin{bmatrix} \bar{\boldsymbol{u}}_{\bar{T}}(z_{j-1}) \\ \bar{\boldsymbol{t}}_{\bar{q}}(z_{j+1}) \end{bmatrix} = \begin{bmatrix} \mathbf{V}_{11}^{j-1:j} & \mathbf{V}_{12}^{j-1:j} \\ \mathbf{V}_{21}^{j-1:j} & \mathbf{V}_{22}^{j-1:j} \end{bmatrix} \begin{bmatrix} \bar{\boldsymbol{u}}_{\bar{T}}(z_{j+1}) \\ \bar{\boldsymbol{t}}_{\bar{q}}(z_{j-1}) \end{bmatrix}, \tag{68}$$

where the superscripts $^{j-1:j}$ denote the resulting propagation submatrices from layer $j-1$ to layer j, for any perfect internal interfaces described for $j = 2, \ldots, N$. The corresponding 4×4 recurrence layer-to-layer submatrices in eq. (68) are defined by

$$\begin{cases} \mathbf{V}_{11}^{j-1:j} = \mathbf{V}_{11}^{j-1}\mathbf{V}_{11}^{j} + \mathbf{V}_{11}^{j-1}\mathbf{V}_{12}^{j}\left[\mathbf{I}_{4\times4} - \mathbf{V}_{21}^{j-1}\mathbf{V}_{12}^{j}\right]^{-1}\mathbf{V}_{21}^{j-1}\mathbf{V}_{11}^{j}, & \text{(69a)} \\ \mathbf{V}_{12}^{j-1:j} = \mathbf{V}_{12}^{j-1} + \mathbf{V}_{11}^{j-1}\mathbf{V}_{12}^{j}\left[\mathbf{I}_{4\times4} - \mathbf{V}_{21}^{j-1}\mathbf{V}_{12}^{j}\right]^{-1}\mathbf{V}_{22}^{j-1}, & \text{(69b)} \\ \mathbf{V}_{21}^{j-1:j} = \mathbf{V}_{21}^{j} + \mathbf{V}_{22}^{j}\left[\mathbf{I}_{4\times4} - \mathbf{V}_{21}^{j-1}\mathbf{V}_{12}^{j}\right]^{-1}\mathbf{V}_{21}^{j-1}\mathbf{V}_{11}^{j}, & \text{(69c)} \\ \mathbf{V}_{22}^{j-1:j} = \mathbf{V}_{22}^{j}\left[\mathbf{I}_{4\times4} - \mathbf{V}_{21}^{j-1}\mathbf{V}_{12}^{j}\right]^{-1}\mathbf{V}_{22}^{j-1}, & \text{(69d)} \end{cases}$$

where the individual elements $\mathbf{V}_{\xi\delta}^{j}$ are specified in eq. (67).

4.2.2. Interfacial duality properties

For the general layered case that is bounded by two imperfect interfaces, the layer-to-layer eqs. (69) can be extended by introducing and rearranging the interface matrix characterized in Section 4.1.2, and by propagating the thermoelastic solutions from the lower side at $z' = z_j^-$ to the upper side at $z' = z_j^+$. Thus, for the lower interface at $z' = z_j$, designated in the following by "int. L", the interfacial dual variable and position form of eq. (54) reads

$$\begin{bmatrix} \bar{\boldsymbol{u}}_{\bar{T}}(z_j^-) \\ \bar{\boldsymbol{t}}_{\bar{q}}(z_j^+) \end{bmatrix} = \underline{\mathbf{Z}}_j^{\text{int.L}} \begin{bmatrix} \bar{\boldsymbol{u}}_{\bar{T}}(z_j^+) \\ \bar{\boldsymbol{t}}_{\bar{q}}(z_j^-) \end{bmatrix}, \tag{70}$$

where the corresponding elements of the interfacial matrix $\underline{\mathbf{Z}}_j^{\text{int.L}}$ are defined by

$$\underline{\mathbf{Z}}_j^{\text{int.L}} = \begin{bmatrix} \underline{\mathbf{Z}}_{11}^{\text{int.L}} & \underline{\mathbf{Z}}_{12}^{\text{int.L}} \\ \underline{\mathbf{Z}}_{21}^{\text{int.L}} & \underline{\mathbf{Z}}_{22}^{\text{int.L}} \end{bmatrix}_j = \begin{bmatrix} \mathbf{I}_{4\times4} & -\operatorname{diag}\left[\alpha_1^{(j)}, \alpha_2^{(j)}, \alpha_3^{(j)}, -(1-\eta)\,\beta_T^{(j)}\right] \\ \operatorname{diag}\left[0, 0, 0, -\eta\,\gamma_T^{(j)}\left(p_m^2 + q_n^2\right)\right] & \mathbf{I}_{4\times4} \end{bmatrix}, \tag{71}$$

combining eqs. (55), (57) and (58) with eqs. (66) and (67). By virtue of eq. (70), the particular interface "int. L" is conceptually considered as a distinct layer with an infinitely small thickness. In eq. (71), the binary term $\eta = 0$ or $= 1$ stands for weakly or highly conducting interfaces, respectively, as expressed in Section 4.1.2. Furthermore, the propagation from z_j^+ to any fictitious horizontal surface at z_f in layer j is described by

$$\begin{bmatrix} \bar{\boldsymbol{u}}_{\bar{T}}(z_j^+) \\ \bar{\boldsymbol{t}}_{\bar{q}}(z_f) \end{bmatrix} = \begin{bmatrix} \mathbf{V}_{11}^{j} & \mathbf{V}_{12}^{j} \\ \mathbf{V}_{21}^{j} & \mathbf{V}_{22}^{j} \end{bmatrix} \begin{bmatrix} \bar{\boldsymbol{u}}_{\bar{T}}(z_f) \\ \bar{\boldsymbol{t}}_{\bar{q}}(z_j^+) \end{bmatrix}, \tag{72}$$

according to eq. (66) with eq. (67), so that eqs. (70) and (72) are combined as follows

$$\begin{bmatrix} \bar{\boldsymbol{u}}_{\bar{T}}(z_j^-) \\ \bar{\boldsymbol{t}}_{\bar{q}}(z_f) \end{bmatrix} = \begin{bmatrix} \mathbf{V}_{11}^{\text{int.L}:j} & \mathbf{V}_{12}^{\text{int.L}:j} \\ \mathbf{V}_{21}^{\text{int.L}:j} & \mathbf{V}_{22}^{\text{int.L}:j} \end{bmatrix} \begin{bmatrix} \bar{\boldsymbol{u}}_{\bar{T}}(z_f) \\ \bar{\boldsymbol{t}}_{\bar{q}}(z_j^-) \end{bmatrix}, \tag{73}$$

as defined in eq. (68). Using eqs. (69), the corresponding recurrence relations in eq. (73) are given by

$$\begin{cases} \mathbf{V}_{11}^{\text{int.L}:j} = \mathbf{V}_{11}^{j} + \mathbf{V}_{12}^{j}\,\mathbf{Y}_{12}^{j}\,\underline{\mathbf{Z}}_{21}^{\text{int.L}}\,\mathbf{V}_{11}^{j}, & \text{(74a)} \\ \mathbf{V}_{12}^{\text{int.L}:j} = \underline{\mathbf{Z}}_{12}^{\text{int.L}} + \mathbf{V}_{12}^{j}\,\mathbf{Y}_{12}^{j}, & \text{(74b)} \\ \mathbf{V}_{21}^{\text{int.L}:j} = \mathbf{V}_{21}^{j} + \mathbf{V}_{22}^{j}\,\mathbf{Y}_{12}^{j}\,\underline{\mathbf{Z}}_{21}^{\text{int.L}}\,\mathbf{V}_{11}^{j}, & \text{(74c)} \\ \mathbf{V}_{22}^{\text{int.L}:j} = \mathbf{V}_{22}^{j}\,\mathbf{Y}_{12}^{j}, & \text{(74d)} \end{cases}$$

in which $\mathbf{Y}_{12}^{j}$ is explicitly formulated as follows

$$\mathbf{Y}_{12}^{j} = \left[\mathbf{I}_{4\times4} - \underline{\mathbf{Z}}_{21}^{\text{int.L}}\,\mathbf{V}_{12}^{j}\right]^{-1} = \operatorname{diag}\left[1, 1, 1, F_{11}\left(F_{11} + \eta\,\gamma_T^{(j)}\left(p_m^2 + q_n^2\right)F_{12}\right)^{-1}\right], \tag{75}$$

which is reduced to the identity matrix, when $\gamma_T^{(j)} = 0$. In eq. (75), both thermal scalars F_{11} and F_{12} are given in eq. (53c).

Applying the same procedure for the potential imperfect interface "int. U" at the upper surface of the layer j, the subsequent interfacial dual variable and position relation at z_{j+1} is given

$$\begin{bmatrix} \bar{\boldsymbol{u}}_{\bar{T}}(z_{j+1}^-) \\ \bar{\boldsymbol{t}}_{\bar{q}}(z_{j+1}^+) \end{bmatrix} = \underline{\mathbf{Z}}_{j+1}^{\text{int.U}} \begin{bmatrix} \bar{\boldsymbol{u}}_{\bar{T}}(z_{j+1}^+) \\ \bar{\boldsymbol{t}}_{\bar{q}}(z_{j+1}^-) \end{bmatrix}, \tag{76}$$

where $\underline{\mathbf{Z}}_{j+1}^{\text{int.U}}$ is similarly defined as in eq. (71), while eq. (68) becomes

$$\begin{bmatrix} \bar{\boldsymbol{u}}_{\bar{T}}(z_f) \\ \bar{\boldsymbol{t}}_{\bar{q}}(z_{j+1}^+) \end{bmatrix} = \begin{bmatrix} \mathbf{V}_{11}^{j:\text{int.U}} & \mathbf{V}_{12}^{j:\text{int.U}} \\ \mathbf{V}_{21}^{j:\text{int.U}} & \mathbf{V}_{22}^{j:\text{int.U}} \end{bmatrix} \begin{bmatrix} \bar{\boldsymbol{u}}_{\bar{T}}(z_{j+1}^+) \\ \bar{\boldsymbol{t}}_{\bar{q}}(z_f) \end{bmatrix}, \tag{77}$$

with the following propagation submatrices from the layer j to "int. U", as follows

$$\begin{cases} \mathbf{V}_{11}^{j:\text{int.U}} = \mathbf{V}_{11}^{j} + \mathbf{V}_{11}^{j}\,\underline{\mathbf{Z}}_{12}^{\text{int.U}} \left[\mathbf{I}_{4\times4} - \underline{\mathbf{Z}}_{12}^{\text{int.U}}\,\mathbf{V}_{21}^{j}\right]^{-1} \mathbf{V}_{21}^{j}, & \text{(78a)} \\ \mathbf{V}_{12}^{j:\text{int.U}} = \mathbf{V}_{12}^{j} + \mathbf{V}_{11}^{j}\,\underline{\mathbf{Z}}_{12}^{\text{int.U}} \left[\mathbf{I}_{4\times4} - \underline{\mathbf{Z}}_{12}^{\text{int.U}}\,\mathbf{V}_{21}^{j}\right]^{-1} \mathbf{V}_{22}^{j}, & \text{(78b)} \\ \mathbf{V}_{21}^{j:\text{int.U}} = \underline{\mathbf{Z}}_{21}^{\text{int.U}} + \left[\mathbf{I}_{4\times4} - \underline{\mathbf{Z}}_{12}^{\text{int.U}}\,\mathbf{V}_{21}^{j}\right]^{-1} \mathbf{V}_{21}^{j}, & \text{(78c)} \\ \mathbf{V}_{22}^{j:\text{int.U}} = \left[\mathbf{I}_{4\times4} - \underline{\mathbf{Z}}_{12}^{\text{int.U}}\,\mathbf{V}_{21}^{j}\right]^{-1} \mathbf{V}_{22}^{j}, & \text{(78d)} \end{cases}$$

which differ from eqs. (74). It is worth noting, however, that eqs. (74) and (78) are equivalent and are reduced to the elements and submatrices for the perfect interfacial case, when the perfect thermoelastic interface conditions are satisfied, when $\beta_T^{(k)} = \gamma_T^{(k)} = \alpha_i^{(k)} = 0$ in all $\underline{\mathbf{Z}}^{\text{int}}$-matrices.

4.2.3. Recursive criss-cross solutions in multilayers

By continuously propagating eq. (68) through all layers from the bottom external surface at $z_1 = 0$ to the top surface at $z_{N+1} = H$ and passing all internal interfaces, the corresponding recursive relation for thermoelastic solutions is formulated as follows

$$\begin{bmatrix} \bar{\boldsymbol{u}}_{\bar{T}}(0) \\ \bar{\boldsymbol{t}}_{\bar{q}}(H) \end{bmatrix} = \mathbf{V}_{8\times8}^{1:N} \begin{bmatrix} \bar{\boldsymbol{u}}_{\bar{T}}(H) \\ \bar{\boldsymbol{t}}_{\bar{q}}(0) \end{bmatrix} = \begin{bmatrix} \mathbf{V}_{11}^{1:N} & \mathbf{V}_{12}^{1:N} \\ \mathbf{V}_{21}^{1:N} & \mathbf{V}_{22}^{1:N} \end{bmatrix} \begin{bmatrix} \bar{\boldsymbol{u}}_{\bar{T}}(H) \\ \bar{\boldsymbol{t}}_{\bar{q}}(0) \end{bmatrix}, \tag{79}$$

where the built-in layer-to-layer submatrices $\mathbf{V}_{\xi\delta}^{j-1:j}$ from the layer $j-1$ to layer j with $j = 2, 3, \ldots, N$, are given by eqs. (74) and (78) for any lower and upper interfaces at z_j and z_{j+1}, respectively. For any field point z_f in layer j, eq. (79) is therefore split into two equivalent systems that recursively propagate the solutions from $z_1 = 0$ to z_f and from z_f to $z_{N+1} = H$ to obtain the following sets of linear equations, i.e.

$$\begin{cases} \begin{bmatrix} \bar{\boldsymbol{u}}_{\bar{T}}(0) \\ \bar{\boldsymbol{t}}_{\bar{q}}(z_f) \end{bmatrix} = \begin{bmatrix} \mathbf{V}_{11}^{1:j} & \mathbf{V}_{12}^{1:j} \\ \mathbf{V}_{21}^{1:j} & \mathbf{V}_{22}^{1:j} \end{bmatrix} \begin{bmatrix} \bar{\boldsymbol{u}}_{\bar{T}}(z_f) \\ \bar{\boldsymbol{t}}_{\bar{q}}(0) \end{bmatrix}, & \text{(80a)} \\ \begin{bmatrix} \bar{\boldsymbol{u}}_{\bar{T}}(z_f) \\ \bar{\boldsymbol{t}}_{\bar{q}}(H) \end{bmatrix} = \begin{bmatrix} \mathbf{V}_{11}^{j:N} & \mathbf{V}_{12}^{j:N} \\ \mathbf{V}_{21}^{j:N} & \mathbf{V}_{22}^{j:N} \end{bmatrix} \begin{bmatrix} \bar{\boldsymbol{u}}_{\bar{T}}(H) \\ \bar{\boldsymbol{t}}_{\bar{q}}(z_f) \end{bmatrix}, & \text{(80b)} \end{cases}$$

which can be recast as follows

$$\begin{bmatrix} \mathbf{V}_{11}^{1:j} & \mathbf{0}_{4\times4} & -\mathbf{I}_{4\times4} & \mathbf{0}_{4\times4} \\ \mathbf{V}_{21}^{1:j} & -\mathbf{I}_{4\times4} & \mathbf{0}_{4\times4} & \mathbf{0}_{4\times4} \\ -\mathbf{I}_{4\times4} & \mathbf{V}_{12}^{j:N} & \mathbf{0}_{4\times4} & \mathbf{V}_{11}^{j:N} \\ \mathbf{0}_{4\times4} & \mathbf{V}_{22}^{j:N} & \mathbf{0}_{4\times4} & \mathbf{V}_{21}^{j:N} \end{bmatrix} \begin{bmatrix} \bar{\boldsymbol{u}}_{\bar{T}}(z_f) \\ \bar{\boldsymbol{t}}_{\bar{q}}(z_f) \\ \bar{\boldsymbol{u}}_{\bar{T}}(0) \\ \bar{\boldsymbol{t}}_{\bar{q}}(H) \end{bmatrix} = \begin{bmatrix} -\mathbf{V}_{12}^{1:j}\,\bar{\boldsymbol{t}}_{\bar{q}}(0) \\ -\mathbf{V}_{22}^{1:j}\,\bar{\boldsymbol{t}}_{\bar{q}}(0) \\ \mathbf{0}_{4\times1} \\ \bar{\boldsymbol{t}}_{\bar{q}}(H) \end{bmatrix}, \tag{81}$$

where the external boundary-value solutions $\bar{\boldsymbol{t}}_{\bar{q}}(0)$ and $\bar{\boldsymbol{t}}_{\bar{q}}(H)$ on the right-hand side must be written with respect to the prescribed mechanical tractions $\bar{\boldsymbol{t}}_{mn}^{B}$ and $\bar{\boldsymbol{t}}_{mn}^{T}$ as well as temperatures $\bar{T}_{mn}^{B}$ and $\bar{T}_{mn}^{T}$ on both the bottom and top surfaces at $z = 0$ and $z = H$, respectively. Considering the main components of the general matrix $\mathbf{V}_{8\times8}^{1:N}$ in eq. (79) as follows

$$\mathbf{V}_{8\times8}^{1:N} = \begin{bmatrix} \begin{bmatrix} \mathbf{M}_{11} & \boldsymbol{M}_{12} \\ \mathbf{0}_{1\times3} & M_{22} \end{bmatrix} & \begin{bmatrix} \mathbf{M}_{13} & \boldsymbol{M}_{14} \\ \mathbf{0}_{1\times3} & M_{24} \end{bmatrix} \\ \begin{bmatrix} \mathbf{M}_{31} & \boldsymbol{M}_{32} \\ \mathbf{0}_{1\times3} & M_{42} \end{bmatrix} & \begin{bmatrix} \mathbf{M}_{33} & \boldsymbol{M}_{34} \\ \mathbf{0}_{1\times3} & M_{44} \end{bmatrix} \end{bmatrix}, \tag{82}$$

		case 1		case 2		case 3			
Property	unit	graphite/epoxy	soft core	Cu	Mo	ZrO_2	Al_2O_3	β-NiAlPt	CMSX4
k_{11}	W/m/K	50.0	50.0	401.0	142.0	1.5	8.0	20.0	20.0
k_{22}	W/m/K	0.5	50.0	401.0	142.0	1.5	8.0	20.0	20.0
k_{33}	W/m/K	0.5	50.0	401.0	142.0	1.5	8.0	20.0	20.0
α_{11}	10^{-6}/K	-2.0	30.0	16.5	5.3	10.0	8.0	15.0	14.0
α_{22}	10^{-6}/K	50.0	30.0	16.5	5.3	10.0	8.0	15.0	14.0
α_{33}	10^{-6}/K	50.0	30.0	16.5	5.3	10.0	8.0	15.0	14.0
c_{11}	GPa	201.55	1.62	168.4	460.0	405.0	498.0	199.0	174.0
c_{22}	GPa	9.16	3.24	168.4	460.0	405.0	498.0	199.0	174.0
c_{33}	GPa	9.16	3.24	168.4	460.0	405.0	498.0	199.0	174.0
c_{12}	GPa	3.10	1.25	121.4	176.0	110.0	163.0	137.0	97.0
c_{13}	GPa	3.10	1.25	121.4	176.0	110.0	163.0	137.0	97.0
c_{23}	GPa	2.32	1.38	121.4	176.0	110.0	163.0	137.0	97.0
c_{44}	GPa	2.20	3.70	75.4	110.0	58.0	147.0	116.0	112.0
c_{55}	GPa	5.00	0.80	75.4	110.0	58.0	147.0	116.0	112.0
c_{66}	GPa	5.00	0.80	75.4	110.0	58.0	147.0	116.0	112.0
ρ	kg/m^3					5680.0	3950.0	5960.0	8374.0

Table 1: Constituent thermoelastic properties for an effective graphite fiber/epoxy matrix composite (example 1) and a multilayered thermal barrier on a superalloy (example 2). The thermal expansion coefficients k_{ii} are in W/m/K, the thermal conductivities α_{ii} in 10^{-6} /K, the elastic stiffness components c_{ij} are in GPa, and the densities ρ in kg/m^3. All anisotropic properties of the graphite/epoxy composite are effective that have been calculated using a classical homogenization procedure.

the vectors $\bar{\boldsymbol{t}}_{\bar{q}}$ at both external surfaces on the right-hand side of eq. (81) are analytically determined by solving eq. (79) and are also given by

$$\bar{\boldsymbol{t}}_{\bar{q}}(0) = \begin{bmatrix} \bar{\boldsymbol{t}}^{B}_{mn} \\ -M_{24}^{-1}\left(M_{22}\bar{T}^{T}_{mn} - \bar{T}^{B}_{mn}\right) \end{bmatrix}, \tag{83a}$$

$$\bar{\boldsymbol{t}}_{\bar{q}}(H) = \begin{bmatrix} \bar{\boldsymbol{t}}^{T}_{mn} \\ -M_{24}^{-1}\left((M_{22}\,M_{44} - M_{24}\,M_{42})\bar{T}^{T}_{mn} - M_{44}\bar{T}^{B}_{mn}\right) \end{bmatrix}, \tag{83b}$$

which are valid for any integers m and n, as explicitly described in Section 5.1 for various combined examples of external boundary conditions. The physical solutions for the displacement, temperature, traction vectors, and normal heat flux defined at any position z_f within the j^{th} layer are determined by inverting the left-hand side matrix of eq. (81) and simply introducing the double sums of infinite sine and cosine series over m and n as well as the time-dependent factor $\mathrm{e}^{i\omega t}$. Identical to the previous approach I in Section 4.1, the remaining in-plane stress components $\bar{\boldsymbol{\tau}}(z_f)$ are obtained from eqs. (43 – 46).

5. Application examples

Illustrative examples of the present theory of thermoelasticity in multilayered structures subjected to external distributed loads are provided for various thermal stress problems. General surface distributions of temperature and tractions in arbitrary rectangular domains on the opposite sides are reported in Section 5.1, including uniformly and heterogeneously distributed loads. These treatments complete the solutions in eq. (83) by determining the specific expansion coefficients in accordance with the prescribed boundary conditions. Three cases are analyzed and specific effects on the field solutions in modern applications are qualitatively described. The preliminary case 1 is related to the steady-state and transient thermoelastic response of composite-faced soft-core sandwich plates with high anisotropy. Effects of the aspect ratios, of the length scale nonlocal parameter with respect to the classical theory, and of two types of external loads on the multilayered structure are discussed in Section 5.2. Comparison between the propagation matrix method and the dual variable and position technique on the convergence of field solutions are evaluated, exhibiting the computational instability issues inherent in the former. In Section 5.3, case 2 illustrates further the effects on the converged solutions in metallic multilayers composed of Cu and Mo plates, including the number and the stacking sequences of individual layers as well as specific boundary conditions with imperfect thermal contact between constituents. In Section 5.4, case 3 examines the residual stress fields in thermal barrier coated superalloys induced by several boundary-value conditions. In particular, forced vibration analysis of four-layered superalloys is investigated with special attention on the temperature-dependent material properties as well as the imperfect mechanical contact properties at internal interfaces. Comparison with the equivalent homogeneous problem, the role played by the thermal barrier coating made of a low-thermal conductivity ceramic is quantified. The material properties used in these three cases are defined in Table 1.

5.1. Distributed surface loads for external temperature and tractions

As pictured in Fig. (1b), general two-dimensional distributions of temperature and normal stresses are applied on both the bottom and top surfaces in an arbitrary manner. Without loss of generality, the temperature is always uniformly distributed on both external

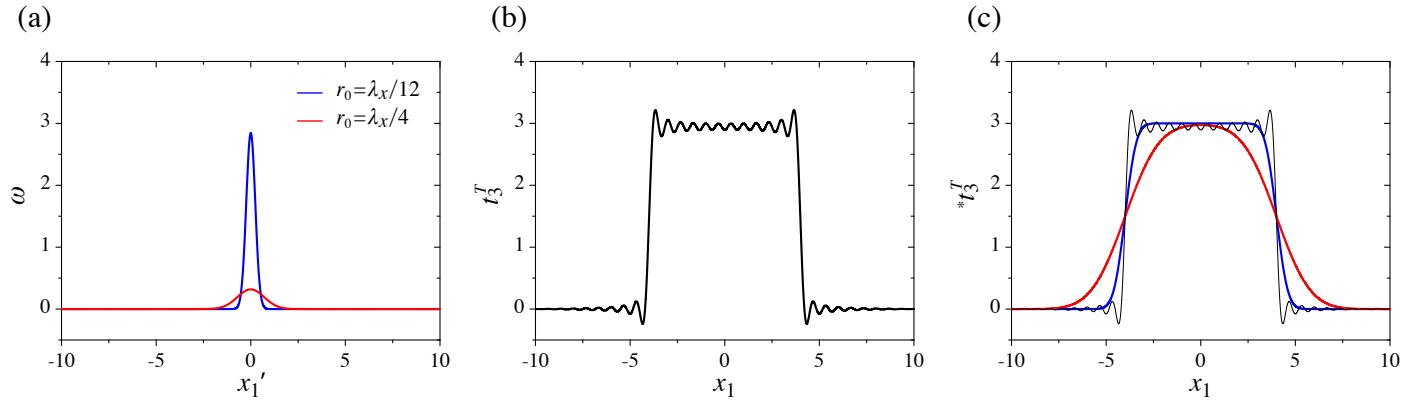

Figure 2: (a) Cross section of the two-dimensional Gaussian kernel with respect to two standard deviations. (b) Rectangular distribution of the normal stress field applied to the external surface with $m = n = 30$ harmonic terms. (c) Convolution of the rectangular distributed load with the Gaussian pulses, which gives rise to smoothed normal tractions without spurious oscillations. This procedure avoids the standard Gibbs phenomenon near singularities in piecewise discontinuous functions.

surfaces with different amplitudes, while the tractions can be heterogeneously distributed within rectangular domains. Using a spreading procedure by convolution with a Gaussian function to regularize the stress singularities at the dislocation cores (Vattré and Pan, 2019), the latter distribution can be adequately and advantageously (for numerical reasons) described using only a few first terms in each Fourier series. For both types of uniformly and heterogeneously distributed loads, the corresponding series expansion coefficients are analytically determined.

5.1.1. Homogeneously distributed loads

With regard to the Fourier series representations of the temperature, the corresponding series expansions $\bar{T}^B_{mn}$ in eq. (8a) for a uniform distribution on the bottom surface is merely defined for any combination of m and n by

$$\bar{T}^B_{mn} = \begin{cases} \dfrac{16}{\pi^2 mn}\bar{T}^B, & n \text{ and } m \text{ odd}, \quad (84a) \\ 0, & n \text{ or } m \text{ even}, \quad (84b) \end{cases}$$

where $\bar{T}^B$ is the physical prescribed temperature in K. On the top surface, similar expressions as in eqs. (84) for the uniformly distributed temperature $\bar{T}^T_{mn}$ are derived with respect to the constant $\bar{T}^T$. Without loss of generality, the forced vibration treatment of multilayered plates under a time-harmonic normal traction is considered, while all other traction components at bottom and top surfaces are zero. Thus, the double Fourier series expansions for applied tractions at the bottom surface are given by

$$\bar{\boldsymbol{t}}^B_{mn} = \left[0, 0, \bar{\sigma}^B_{33mn}\right]^{\mathsf{t}}, \quad (85)$$

where the uniformly distributed normal traction $\bar{\sigma}^B_{33mn}$ is analogously defined to eq. (84a) by

$$\bar{\sigma}^B_{33mn} = \begin{cases} \dfrac{16}{\pi^2 mn}\bar{\sigma}^B_{33}, & n \text{ and } m \text{ odd}, \quad (86a) \\ 0, & n \text{ or } m \text{ even}, \quad (86b) \end{cases}$$

with $\bar{\sigma}^B_{33}$ being constant in Pa. The specific free surface condition is also satisfied by imposing $\bar{\sigma}^B_{33} = 0$ in eq. (86a). The same treatment for the applied tractions $\bar{\boldsymbol{t}}^T_{mn}$ at the top surface is completed, and the free-standing condition on multilayered structures can be investigated for $\bar{\sigma}^T_{33} = \bar{\sigma}^B_{33} = 0$. Importantly, eqs. (84−86) as well as the equivalent expressions for the top surface are introduced into eq. (62) and into eqs. (83) and then eq. (81) to determine the field solutions using approaches I and II from Sections 4.1 and 4.2, respectively, for any m and n. In practice, the Fourier series expansions $\bar{\boldsymbol{t}}^T_{mn}$ can, however, be formulated to provide a heterogeneously-distributed load on the top surfaces, as described in Section 5.1.2

5.1.2. Heterogeneous spreading normal loads for tractions

Following the procedure for core-spreading dislocations by Vattré and Pan (2019), the normal stress vector t^T_3 on the top rectangular surface in eq. (9b) is first conveniently convolved with a Gaussian kernel ϖ, as follows

$${}^*t^T_3(x_1, x_2, z = H, t) = \mathrm{e}^{i\omega t} \sum_{m=1}^{\infty}\sum_{n=1}^{\infty} \bar{\sigma}^T_{33mn} \sin\left(p_m\left(x_1 - L_x/2\right)\right) \sin\left(q_n\left(x_2 - L_y/2\right)\right) * \varpi\left(x_1, x_2\right), \quad (87)$$

where a practical change of space variable for further operations is advocated to shift the applied loads relative to $x_1 = x_2 = 0$. In eq. (87) and in the following, the pre-superscript * indicates the quantities that have been convoluted by the weighted functions. As displayed in

Fig. (2a) with two standard deviations, the Gaussian function ϖ is defined by

$$\varpi\left(x_1,x_2\right)=\frac{\mathrm{e}^{-(x_1+x_2)^2/r_0^2}}{\pi r_0^2}\,,\quad \text{with}:\ \int_{-\infty}^{\infty}\int_{-\infty}^{\infty}\varpi\left(x_1,x_2\right)dx_1dx_2=1\,, \tag{88}$$

where $r_0\geq 0$ is the spreading-stress parameter. Equation (87) is reduced to

$$\begin{aligned}{}^{*}t_3^T\left(x_1,x_2,z=H,t\right)&\equiv \mathrm{e}^{i\omega t}\sum_{m=1}^{\infty}\sum_{n=1}^{\infty}\bar{\sigma}_{33mn}^T\int_{-\infty}^{\infty}\int_{-\infty}^{\infty}\sin\left(p_m\left(x_1'-L_x/2\right)\right)\sin\left(q_n\left(x_2'-L_y/2\right)\right)\varpi\left(x_1-x_1',x_2-x_2'\right)dx_1'dx_2'\\ &=\mathrm{e}^{i\omega t}\sum_{m=1}^{\infty}\sum_{n=1}^{\infty}\bar{\sigma}_{33mn}^T\,\mathrm{e}^{-\left(\pi m\, r_0/(2L_x)\right)^2}\sin\left(p_m\left(x_1'-L_x/2\right)\right)\mathrm{e}^{-\left(\pi n\, r_0/(2L_y)\right)^2}\sin\left(q_n\left(x_2'-L_y/2\right)\right),\end{aligned} \tag{89}$$

such that $r_0=0$ yields to the classical solution in the Fourier series representations. For heterogeneously distributed normal traction over the two-dimensional rectangular domain $-\lambda_x\leq x_1\leq\lambda_x$ and $-\lambda_y\leq x_2\leq\lambda_y$ on the top surface, the expansion series coefficients are determined by the Fourier-Kaplan-Sonnemann transform technique, as follows

$${}^{*}\bar{\sigma}_{33mn}^T=\begin{cases}\dfrac{4}{L_xL_y}\,\mathrm{e}^{i\omega t-(\pi m\, r_0/(2L_x))^2-(\pi n\, r_0/(2L_y))^2}\,\bar{\sigma}_{33}^T\displaystyle\int_{-\lambda_x}^{\lambda_x}\int_{-\lambda_y}^{\lambda_y}\sin\left(p_m\left(x_1'-L_x/2\right)\right)\sin\left(q_n\left(x_2'-L_y/2\right)\right)dx_1dx_2\,, & n \text{ and } m \text{ odd}\,, \quad \text{(90a)}\\ 0\,, & n \text{ or } m \text{ even}\,, \quad \text{(90b)}\end{cases}$$

which, after carrying out the double integral, read

$${}^{*}\bar{\sigma}_{33mn}^T=\begin{cases}(-1)^{\frac{m+3}{2}}\,(-1)^{\frac{n+3}{2}}\,\dfrac{16}{\pi^2mn}\,\mathrm{e}^{i\omega t-(\pi m\, r_0/(2L_x))^2-(\pi n\, r_0/(2L_y))^2}\,\bar{\sigma}_{33}^T\sin\left(\dfrac{\pi m\lambda_x}{2L_x}\right)\sin\left(\dfrac{\pi n\lambda_y}{2L_y}\right), & n \text{ and } m \text{ odd}\,, \quad \text{(91a)}\\ 0\,, & n \text{ or } m \text{ even}\,, \quad \text{(91b)}\end{cases}$$

so that the corresponding Fourier series expansions $\bar{\boldsymbol{t}}_{mn}^T$ in eq. (83b) for spreading-stress tractions at the top surface are given by

$$\bar{\boldsymbol{t}}_{mn}^T=\left[0,0,{}^{*}\bar{\sigma}_{33mn}^T\right]^{\mathsf{t}}, \tag{92}$$

for any m and n. To illustrate the advantage of using the aforementioned spreading procedure on the heterogeneously distributed loads, Fig. (2b) and (2c) show the standard Fourier series representation of the normal traction and the convolution of the latter with the Gaussian kernel on an arbitrary square surface, respectively. The profiles are depicted along the x_1-axis with $x_2=L_y/2$, where $L_x=L_y=10$ m, and $m=n=30$ Fourier terms in eq. (89) as well as $\bar{\sigma}_{33}^T=3$ Pa, and $\lambda_x=\lambda_y=4$ m in eq. (91a) with respect to both standard deviations. It is also shown that the spreading-load procedure inhibits the Gibbs phenomenon near singularities on each of the four edges of the square, within which the normal traction is distributed, and the prescribed traction converges conditionally and numerically faster without spurious oscillations than the standard expansions to the exact solution, even with small value of r_0.

5.2. Cross-ply layers in composite laminates

As in Savoia and Rao (1995), unidirectional graphite-epoxy composites with fibers oriented along the x_1-direction (material I) and a soft core (material II) are investigated. The thermoelastic properties of both materials for this application case 1 are reported in Table 1. The steady-state thermoelastic bending of the three-layered sandwich square plates with $L_x/L_y=1$ are subjected to a sinusoidal temperature that rises at both external horizontal surfaces, with $\bar{T}^B=1$ K, and $\bar{T}^T=-1$ K. The general coupled thermoelastic loads can be applied by combining the previous thermal loading with normal stresses, defined by $\bar{t}^B=-1$ MPa, and $\bar{t}^T=-1$ MPa. The thicknesses of the soft core (material II) and the two stiff external layers (material I) are equal to $0.6H$ and $0.2H$, respectively, where $H=100$ nm is the thickness of the multilayered system. As a preliminary and practical analysis, the field solutions are determined for a few terms in the Fourier series, for which the nonlocal parameter is used as a phenomenological ingredient, with no physical meaning. For the sake of simplicity, both nonlocal parameters l_T and l_E are assumed equal, thus $l_T=l_E=l$. In this Section 5.2, all through-the-thickness profiles are depicted for $x_1=x_2=L_x/2$, thus along the z-direction, and the calculations are performed using $m=n=1$, unless specified otherwise.

Fig. (3) shows the effects of the ratios of L_x/H and l/H on various thermoelastic field solutions, by varying the lateral length L_x as well as the nonlocal parameter l, where the entire thickness H is kept fixed. Figs. (3a) and (3b) depict thermal quantities using the local thermoelastic theory, that is $l=0$. For thinner plates, the temperature profile tends to a linear distribution through each individual layer, as illustrated in Fig. (3a), while nonlinear exponential branches appear in the graphite-epoxy composite plates for larger thicknesses. This trend indicates that when the aspect ratio is small, namely $L_x/H<5$, the standard thin-plate result may be invalid, even though the temperature remains linear (close to zero) in the middle layer. The corresponding curves associated with the heat flux in Fig. (3b)

are different from the temperature variation along the vertical z-direction. In particular, the normal heat flux is continuous across the interfaces and tends also to be steeper for thinner systems, while significant gradient emerges at the external surfaces as L_x/H decreases.

The in-plane normal stress components σ_{11} and σ_{22} are displayed in Figs. (3c-f) for both extreme aspect ratios with further consideration of nonlocal effect. Three ratios for the nonlocal analysis are examined. It is worth noting that with reference to the composite stiff faces, higher in-plane stress levels occur in the direction perpendicular to the fibers. Moreover, due to material property mismatch between the layers, these in-plane normal stresses are discontinuous at both interfaces, with significant discontinuities in σ_{11} when the aspect ratio is small, as shown in Fig. (3d). The amplitudes of these discontinuities at internal interfaces are therefore less pronounced for thinner plates, with negligible effect by the nonlocal parameter. However, the nonlocal parameter l has a significant influence on the stress field for extremely thick plates subjected to thermal loads only, where the nonlocal parameter can completely change the variation trend of the stresses, switching their signs and altering their magnitudes, as depicted by the blue curves in Figs. (3d) and (3f).

Figs. (4a-d) and (4e-h) illustrate the effects of the type of external loads on the vertical and horizontal displacement components u_3 and u_2, specially under the thermal only, as shown in Figs. (3), and under the combined thermal and mechanical load case, respectively. Again, the two aspect ratios, i.e., $L_x/H = 10$ and $L_x/H = 2$, are considered, with further three values for the nonlocal parameter $l = 0$ (i.e., local theory), $l/H = 0.04$, and $l/H = 0.1$, reasonably comparable to the range of similar parameters obtained by atomistic models and hybrid atomistic/continuum mechanics under static and dynamic loadings (Ansari and Sahmani, 2013, Arash and Wang, 2012, Chen et al., 2017, Waksmanski and Pan, 2014). Regarding the displacement solutions induced by thermal loading only, the effect of nonlocal parameter is significant when the aspect ratio is small (i.e., for thick layered plates), with different variation trends by comparing Figs. (4a) to (4b) and (4c) to (4d). As compared to the thermal loading only, the vertical displacements for multilayers subjected to combined loads are more sensitive to the nonlocal parameter than the corresponding horizontal displacement fields. This feature is attributed to the horizontal displacement that has a lower-order curvature (i.e., linear versus quadratic) as compared to the vertical component. Furthermore, except for extremely thick plates subjected to thermal load only, where a complete reversal variation of the horizontal displacement occurs in Fig. (4d), both displacement components gradually vary with increasing nonlocal parameters. It is also worth noting that the nonlocal parameter would enhance the nonlinearity of the elastic field solutions, especially near the external surfaces and internal interfaces.

Figs. (5a-d) and (5e-h) picture the traction components σ_{33} and σ_{23} under thermal loading only and combined thermomechanical loads, for both aspect ratios and the nonlocal parameter values, as in Figs. (4). It is noted first that these field solutions on both bottom and top surfaces are either zero (i.e., free tractions for thermal loads) or equal to the applied tractions (i.e., under combined loads), as requested. These values accurately validate the present formulation and the numerical results by means of the prescribed boundary conditions. It is observed that the normal stress σ_{33} is equal to zero at the middle of the multilayers with an asymmetrical distribution with respect to the median line at $z/H = 0.5$, while the residual shear component σ_{23} is symmetrically distributed. As shown in Figs. (5c) and (5d) under thermal loading only, the highest magnitude of the stress component is either located close to the internal interfaces, or in the middle of the top/bottom graphite-epoxy layers, respectively. On the other hand, both stress components are very sensitive to the nonlocal parameter, with reversal distribution trends for thick plate with a large nonlocal parameter, similar to those observed in Figs. (4). Under combined loads, however, these stresses are nearly independent of the nonlocal parameter, except for σ_{23} in Fig. (5h) when the plate is thick and the nonlocal parameter is large.

Fig. (6) compares different thermoelastic field solutions obtained by both recursive methods from the Section 4, namely the propagation matrix method (PMM) and the dual variable and position (DVP) technique, under the combined thermomechanical load with various numbers of Fourier series terms. It is also observed that for small numbers of harmonics m and n (i.e., from $m = n = 1$ to $m = n = 4$), both PMM and DVP methods yield the same field solutions for thermal quantities T and q_3, as well as the elastic stress components σ_{11} and σ_{33}. For $m = n = 7$, however, solutions by the PMM method dramatically diverge, while the DVP technique is still able to rigorously determine the accurate solutions. Furthermore, it is shown that for modeling the distributed surface loading, the convergence of σ_{33} to the exact solution is slower than σ_{11} using the DVP approach. In the following, converged solutions will be determined using the DVP method with 128 terms in each Fourier series to meet an excellent agreement with the prescribed distribution of normal loads.

5.3. Multilayered structures with Cu and Mo plates

The steady-state thermoelastic response of the three- and five-layered systems composed of Cu and Mo layers is analyzed. Nanocomposites that consist of alternating Cu and Mo layers become increasingly important in the field of thermal management for electronic devices. This is due to the excellent thermal properties that cannot be met by the individual constituents, but may be found by stacking both layers since the heterogeneous Mo-based metallic multilayers have very strong interface bounding as well as high thermal conductivity. The corresponding residual stresses with respect to specific interface conditions are therefore of major relevance in designing novel multilayers with unprecedented thermomechanical properties.

The symmetric thin plates are considered with $L_x/L_y = 1$ and $L_x/H = 10$, while all individual plates have the same thickness $h = 20$ nm. The properties of both Cu and Mo for this case 2 are listed in Table 1, and all the following calculations are performed using the local thermoelasticity theory, thus with $l_T = l_E = 0$. Both thermal and thermomechanical loadings are examined, where the steady-state temperature is uniformly distributed over both bottom and top surfaces with $\bar{T}^B = 300$ K and $\bar{T}^T = 340$ K, respectively. On the other hand, the normal traction on the top surface is $\bar{t}^T = 1$ MPa, while the free traction condition is applied on the bottom surface. Both perfectly and imperfectly thermal boundary conditions on internal interfaces are investigated in Figs. (7) and (8), respectively.

Fig. (7) shows various through-the-thickness elastic field profiles along the z-direction for $x_1 = L_x/4$ and $x_2 = 3L_x/4$. The influence of the number of harmonic terms used in the Fourier series (i.e., $m = n = 1$ versus $m = n = 128$), of the number of individual layers (i.e., three versus five) as well as of the stacking sequences (i.e., Cu/.../Cu versus Mo/.../Mo) are examined. The calculations that are

carried out with 128 terms in each Fourier series yield the converged field solutions with high accuracy, while the first harmonic term gives rise to results that are far from the exact solutions. Furthermore, since the reversal variation with respect to m and n are shown for the normal σ_{33} and the transverse shear σ_{23} stress components, a sufficient number of Fourier series terms is highly recommended to analyze realistic (i.e., converged) thermoelastic fields.

Compared to different layups, it is observed that the Cu/Mo/Cu and Cu/Mo/Cu/Mo/Cu multilayered systems exhibit higher magnitude in the elastic displacement u_3 than the Mo/Cu/Mo and Mo/Cu/Mo/Cu/Mo multilayers with piecewise variations. The largest displacement amplitudes are located in the Cu layers. Overall, the magnitude of the stresses is reduced when the middle layer of the sandwich (e.g., Cu/Mo/Cu) is replaced by a reversed sandwich (e.g., Cu/Mo/Cu/Mo/Cu). Furthermore, the normal stress σ_{33} is roughly three times higher in Cu/Mo/Cu than in Mo/Cu/Mo with opposite sign. The in-plane stress component σ_{12} is almost uniformly distributed in each layer with the highest magnitude in the Mo layers. On the other hand, alternating zig-zag transverse shear stress σ_{23} profiles are observed with the largest magnitude at the internal interfaces.

Fig. (8) shows different through-the-thickness distributions of converged field solutions at $x_1 = x_2 = L_x/2$ for the Cu/Mo/Cu composite in presence of thermally imperfect interfaces. As illustrated in Fig. (8a), both internal interfaces are assumed to have weak (red curves), high (blue curves) conduction properties, while the third example case combines both weakly and highly conducting interfaces (green curves). The solutions are compared to the results from calculations with perfectly thermal interface conditions (black curves). Considering the internal interfaces with fictitious thin thicknesses h_{int}, the corresponding interfacial conductivity k_{int} in W/m/K is introduced to link the intrinsic interfacial properties with the properties in bulk materials. Thus, both thermal parameters β_T and γ_T for weakly and highly conducting interfaces in eqs. (11b) and (12b) are defined by $\beta_T = \delta\, h_{\text{int}}/k_{\text{int}}$ and $\gamma_T = \delta\, h_{\text{int}}\, k_{\text{int}}$, where δ is an arbitrary parameter that describes the relation between the effective thermal conductivity in multilayers and the interfacial conductivity, respectively. Here, $k_{\text{int}} = 200$ W/m/K, and $h_{\text{int}} = 1$ nm, while $\delta = \{0, 10^3, 10^4\}$. The case $\delta = 0$ corresponds to the perfect thermal interface conditions (black curves).

As for the temperature distribution in Fig. (8b), the prescribed boundary conditions are fulfilled at both external (top and bottom) surfaces and internal interfaces, specially for weakly conducting interfaces that produce temperature discontinuities, as requested. The temperature distribution is considerably altered by the imperfect interface conditions, with uniform profiles in the core materials in presence of weak conductive interfaces. The weak thermal conditions at both interfaces give therefore rise to constant temperatures in the outer layers as well, which are equal to the prescribed temperatures. On the other hand, the high conductive interfaces yield to large temperature gradients with piecewise linear profiles in these layers. The normal displacement in Fig. (8c) is very sensitive to the interface imperfection, for which the displacement profiles are relatively smoother nearby the highly than the weakly conducting interfaces. The magnitude of u_3 increases (decreases) with increasing (decreasing) severity of imperfection with thermally weak (high) conduction, specially for the combined weak/high interfacial case that produces the largest magnitudes in the Cu/Mo/Cu composite. As for the stresses, the continuous normal stress field σ_{33} in Fig. (8d), much smaller than σ_{11} in Fig. (8e) in magnitude, is dramatically reduced for the highest conductive interfacial case, to zero for both interfaces with perfectly adiabatic conditions. Interestingly, when the interfaces are weakly conductive, the magnitude of σ_{33} increases (decreases) for $\delta = 10^3$ ($\delta = 10^4$). On the other hand, the in-plane stress field σ_{11} in the core material Mo becomes tensile for large amplitude of thermal imperfections with a compressive state in both Cu layers, while the equivalent mises stress τ_{vm} in the entire Cu/Mo/Cu multilayered structure is strongly dependent on all considered thermal conditions between both Cu and Mo materials, as shown in Fig. (8f).

5.4. Forced vibration of thermal barrier coatings on nickel based superalloys

The residual stress fields in a thermal barrier coated superalloy made of four layers, namely the zirconium dioxide (ceramic) ZrO_2, the thermally grown alumina oxide Al_2O_3, the β-NiAlPt coated Ni-based single crystal superalloy CMSX-4 are examined. The thermoelastic properties are given in Table 1, while the thicknesses of each plate are $h_{ZrO_2} = 100$ μm, $h_{Al_2O_3} = 20$ μm, $h_{\text{NiAlPt}} = 200$ μm, and $h_{\text{CMSX-4}} = 500$ μm, respectively, as displayed in Fig. (10a), with $L_x = L_y = 10$ mm. The thinner layer is also the thermally grown alumina oxide, which exhibits the largest elastic properties as well. In terms of external boundary conditions, both thermal and mechanical loads are applied, specially $\bar{T}^B = 300$ K and $\bar{T}^T = 1300$ K, while $\bar{t}^T = 50$ MPa and the bottom surface is free of tractions. In the following, the steady-state and time-harmonic deformations are performed using the local thermoelasticity theory with 128 terms in each Fourier series.

Fig. (9) shows the temperature T and residual stress field components σ_{33} and σ_{11} as well as the von Mises stress τ_{vm} in the four-layered superalloy under high temperature on the top surface. The converged thermoelastic solutions are determined for four different problems, namely i) the heterogeneous problem, where each layer has constant material properties (black curves), ii) the homogeneous problem, for which all thermoelastic properties have been identified to the CMSX-4 material properties (green curves), iii) the previous heterogeneous problem i) with a heterogeneously distributed normal traction on the top surface (red curves), and iv) the heterogeneous case i) with temperature-dependent material properties (blue curves). The problem iii) is illustrated in Fig. (2), where the normal traction of 50 MPa is applied (zero, outside) on a square with $\lambda_x = \lambda_y = L_x/20$ and $r_0 = \lambda_x/100$. In the temperature-dependent application case iv), each layer is subdivided into 128 thin plates, within which a slow-changing linear temperature variation is assumed. For simplicity, the latter operation is conducted to the elastic constants that arbitrarily vary from their initial values listed in Table 1 at 300 K to zero at 1600 K.

As shown in Fig. (9a), the heterogeneous temperature profile in the four-layered structure shows the main role played by the thermal barrier coating made of a low-thermal conductivity ceramic. The latter provides a major temperature reduction, from the applied temperature on the top surface $\bar{T}^T = 1300$ K to 730 K at the upper surface of the thermally grown alumina oxide Al_2O_3, and to 615 K at the upper surface the CMSX4 superalloy. Without such thermal barrier coatings for gas-turbine engines, the temperature is linearly

distributed, as well as the in-plane σ_{11} and the von Mises τ_{vm} stresses that are continuous at the internal interfaces, as depicted by the green lines in Fig. (9). These linear profiles differ from those provided by the more realistic heterogeneous calculations. It is clear that advanced strategies are required for design engineers of high-pressure turbine blades protected by external thermal barrier coatings since the efficient lifetime prediction of the superalloy/bond coat/thermal barrier systems are mainly controlled by the interactions among the different layers.

The heterogeneous structure with a uniformly distributed traction on the top surface gives rise to a large magnitude of the in-plane stress component σ_{11} in the individual thermally grown alumina oxide layer, which affects the corresponding von Mises stress in Fig. (9d). The normal stresses σ_{33} are continuous at the internal interfaces, while large jumps in σ_{11} are located at the lower and upper interfaces of the Al_2O_3 plate. Furthermore, it is also shown that the von Mises stress in the CMSX-4 superalloy is considerably reduced by adding a low-thermal conductivity coating, which enhances the high-temperature strength heterogeneousof the multilayered structure. Using the temperature-dependent properties, the von Mises stress decreases in CMSX-4, but fairly increases in both NiAlPt and Al_2O_3 layers. Such differences in stress state may favor the phase transition of the β-NiAlPt coatings as well as the void formation and crack initiation at the internal Al_2O_3/NiAlPt interface that could deteriorate the thermal barrier coating system and therefore reduce the lifetime of turbine blades.

It is worth noting that the thermally grown alumina oxide layer would be plastically deformed, and the residual local stresses partially released by introducing misfit dislocations at both ZrO_2/Al_2O_3 and Al_2O_3/NiAlPt interfaces. This contribution could be adressed by extending the recent work (Vattré, 2017, Vattré and Pan, 2018, 2019) to the linearized thermal elasticity theory in three dimensions. On the other hand, the heterogeneously distributed normal load changes the sign of σ_{11} from tension to compression in the top ZrO_2 layer, and becomes constant in both NiAlPt and CMSX-4 layers. Significant differences between the homogeneously and heterogeneously distributed traction are observed in the ceramic ZrO_2 layer, where the von Mises stress considerably increases and decreases (with the gradient amplitude, but with a opposite sign) from the top surface to the upper surface of the Al_2O_3 plate.

The time-harmonic vibration behavior of the coated single crystal superalloy is analyzed with forced frequencies ω from 0 to 10^8 rad/s, as illustrated in Fig. (10a). The normal displacement component u_3 in Fig. (10b) shows two vibration behaviors in response to the top surface harmonic excitation. When $\omega < 2.5 \times 10^7$ rad/s, smooth displacement profiles are qualitatively identical to the steady-state case. However, oscillating regimes are observed for the highest frequencies when $\omega > 2.5 \times 10^7$ rad/s, with alternating positive and negative values with respect to the zero displacement field. The critical frequency $\omega_{\text{c}} = 2.5 \times 10^7$ is considered as the resonant frequency, which produces infinite displacement amplitudes. Both steady-like and oscillating regimes can be identified in terms of normal stress σ_{33}, as illustrated by Fig. (10c) and (10d), respectively. It is shown that the number and distribution of the antinodes and vibration nodes increase with increasing frequencies. Therefore, the heterogeneous thermal-mechanical response of time-harmonically forced vibrations is more complicated than the quasi-static case, which needs to be adequately analyzed case by case for specific external excitations.

The imperfect spring-type interface condition between the thermal barrier coating ZrO_2 and the thermally grown alumina oxide Al_2O_3 layer is introduced to model asperities and voids at the damaged oxide-metal ZrO_2/Al_2O_3 interface. The interfacial spring stiffness parameter α in eq. (10b) is arbitrarily specified as $\alpha = \{0, 10^{-10}, 10^{-8}\}$ m^3/N, while the consequence on the normal stress field component σ_{33} is shown in Figs. (11a) and (11b) for both aforementioned regimes with particular frequencies ω, respectively. When $\omega = 0$ rad/s, the influence of the imperfectly bounded interface conditions on σ_{33} is negligible, but interestingly, the spring interface conditions cause strong oscillations in the top ZrO_2 layer and the lower CMSX-4 superalloy for intermediate (red curves with symbols, where $\omega = 10^6$ rad/s) and high (blue curves with symbols, where $\omega = 10^8$ rad/s) frequencies, respectively. Thus, depending on the frequency vibration amplitudes on thermal barrier coated superalloys during very high cycle fatigue, severe deformations may occur in the single crystal superalloys due to structural imperfections at high frequencies, where the oxide-metal interfaces could also act as failure initiation sites.

For illustration, Fig. (12) shows the two-dimensional in-plane σ_{11}, the normal σ_{33}, and the von Mises τ_{vm} stresses for three representative samples. The residual stress distribution in cross-section are displayed at $x_2 = L_x/2$ with ideal perfectly bonded conditions, namely the steady-state case with uniformly distributed normal tractions on the top surface (sample 1), the steady-state case with heterogeneously distributed normal tractions (sample 2), and the time-harmonic vibration case with $\omega = 10^7$ rad/s and uniformly distributed normal tractions (sample 3). The complex distribution of the residual stresses in the thermal barrier coated superalloy subjected to different loadings can also be used to investigate the internal stress concentrations and to capture the early stages of the crack initiation and propagation, especially close to the various internal interfaces.

6. Concluding remarks

Three-dimensional exact solutions for time-harmonic temperature and thermoelastic stresses in multilayered anisotropic layers are derived with imperfect boundary conditions at internal interfaces using the mathematically elegant Stroh formalism. While the general field solutions for each homogeneous plate are determined using the Eringen nonlocal elasticity theory to capture small scale effects, the multilayered feature is recursively handed by combining the traditional propagation matrix method with the dual variable and position technique. The present solutions are formulated by considering Fourier series expansions, consistently with the representations of the uniformly and heterogeneously distributed loads in arbitrary rectangular domains at both opposite external surfaces. Application illustrations are proposed to throw light on various effects of the externally applied loads and internal imperfections on the thermoelastic fields in three representative multilayered structures, namely:

1. The residual thermal stress fields in graphite fiber-reinforced epoxy matrix composites are shown to be drastically different from those predicted by the classical elasticity theory when nonlocal effects are significant. The present phenomenologically defined nonlocal parameter gives rise to important influence on the field solutions for nonlocal orthotropic plates subjected to thermal loading. In particular, remarkable change in the magnitude and sign of the induced thermal stresses with increasing nonlocal parameter is exhibited when the multilayered nanoscale plates are relatively thick. Molecular dynamics simulations could be used to calibrate the appropriate characteristic values of nonlocal parameters and therefore to cautiously match the corresponding predictions of scale effects in smaller sized structures.
2. Using enough harmonic terms in the Fourier series expansions, the converged thermoelastic solutions in multilayered structures made of Cu and Mo plates are strongly dependent on the stacking sequence as well as the number of anisotropic laminates, especially when the highly thermal conducting conditions are introduced at the internal interfaces.
3. The internal stress fields due to time-harmonically forced vibration in three-dimensional thermal barrier coated superalloys are described using imperfect interfacial properties between adjoining layers and temperature-dependent material properties. Depending on the input frequency amplitude, severe oscillating displacements and stresses take place in the four-layered superalloys that can endanger the safety-related stability and integrity of aircraft engines. While the role played by the thermal barrier coating made of a low-thermal conductivity ceramic is theoretically quantified, the oxide-metal interfaces is shown to act as preferential failure initiation sites.

Overall, the present formalism can be utilized in the preliminary case-by-case design of multilayered samples with desired steady-state and time-harmonic thermoelastic responses. Goodman, Haigh or Soderberg diagrams in the aeronautical and aerospace industries could be improved by integrating such quantification of residual stress fields in turbine blades loaded at high temperatures with large mean stresses and superimposed high-frequency cycle thermal fatigue.

References

Z. Ai, Y. Cheng, 2014. Extended precise integration method for consolidation of transversely isotropic poroelastic layered media. Comput. Math. Appl. 68, 1806-1818.

R. Ansari, S. Sahmani, 2013. Prediction of biaxial buckling behavior of single-layered graphene sheets based on nonlocal plate models and molecular dynamics simulations. Appl. Math. Model. 37, 7338-7351.

B. Arash, Q. Wang, 2012. A review on the application of nonlocal elastic models in modeling of carbon nanotubes and graphenes. Comput. Mater. Sci. 51, 303-313.

K. Bhaskar, T. Varadan, J. Ali, 1995. Thermoelastic solutions for orthotropic and anisotropic composite laminates. Compos. B 27, 415-420.

Y. Benveniste, T. Miloh, 1986. The effective conductivity of composite with imperfect contact at constituent interfaces. Int. J. Engng. Sci. 24, 1537-1552.

Y. Benveniste, 1999. On the decay of end effects in conduction phenomena: a sandwich strip with imperfect interfaces of low or high conductivity. J. Appl. Phys. 86, 1273-1279.

Y. Benveniste, 2006. A general interface model for a three-dimensional curved thin anisotropic interphase between two anisotropic media. J. Mech. Phys. Solids 54, 708-734.

R. Bhangale, N. Ganesan, 2006a. Thermoelastic buckling and vibration behavior of a functionally graded sandwich beam with constrained viscoelastic core. J. Sound Vib. 295, 294-316.

R. Bhangale, N. Ganesan, 2006b. Static analysis of simply supported functionally gradedand layered magneto-electro-elastic plates. Int. J. Solids Struct. 43, 3230-3253.

E. Carrera, 2000. An assessment of mixed and classical theories for the thermal stress analysis of orthotropic multilayered plates. J. Therm. Stresses. 23, 797-831.

J. Chen, J. Guo, E. Pan, 2017. Wave propagation in magneto-electro-elastic multilayered plates with nonlocal effect. J. Sound. Vib., 400, 550-563.

A. Dobyns, 1981. Analysis of simply supported orthotropic plates subject to static and dynamic loads. AIAA Journal 19, 642-650.

A. Eringen, 1967. Mechanics of micromorphic continua. In: Mechanics of generalized continua. Springer: Berlin.

A. Eringen, 1972. Linear theory of nonlocal elasticity and dispersion of plane waves. Int. J. Engng. Sci. 10, 425-435.

A. Eringen, D. Edelen, 1972. On non-local elasticity. Int. J. Engng. Sci. 10, 233-248.

A. Eringen, 1977. Edge dislocation in nonlocal elasticity. Int. J. Engng. Sci. 15, 177-183.

A. Eringen, C. Speziale, B. Kim, 1977. Crack-tip problem in non-local elasticity. J. Mech. Phys. Solids 25, 339-355.

A. Eringen, 1983. On differential equations of nonlocal elasticity and solutions of screw dislocation and surface waves. J. Appl. Phys. 54, 4703-4710.

J. Eshelby, W. Read, W. Shockley, 1953. Anisotropic elasticity with applications to dislocation theory. Acta Metall. 1, 251-259.

A . Evans, J. Hutchinson, 2007. The mechanics of coating delamination in thermal gradients. Surf. Coat. Technol. 201, 7905-7916.

H. Fan, G. Wang, 2003. Screw dislocation interacting with imperfect interface. Mech. Mater. 35, 943-953.

F. Gilbert, G. Backus, 1966. Propagator matrices in elastic wave and vibration problems. Geophys. 31, 326-332.

J. Guo, T. Sun, E. Pan, 2019. Three-dimensional buckling of embedded multilayered magnetoelectroelastic nanoplates/graphene sheets with nonlocal effect. J. Intell. Mater. Syst. Struct. 30, 2870-2893

T. Hirai, D. Kline, 1973. Dynamic mechanical properties of graphite-epoxy and carbon-epoxy composites. J. Comp. Mat. 7, 160-177.

J. Hirth, J. Lothe, 1992. Theory of dislocations. 2nd ed. Kriger: Melbourne.

J. Hutchinson 1967. Axisymmetric vibrations of a solid elastic cylinder encased in a rigid container. J. Acoust. Soc. Am. 42, 398-402.

P. Kapitza, 1941. J.E.T.P 11. Collected papers of P. Kapitza. Pergamon Press: Oxford 1965.

S Kapuria, M. Bhattacharyya, A. Kumar, 2008. Bending and free vibration response of layered functionally graded beams: A theoretical model and its experimental validation. Compos. Struct. 82, 390-402.

A. Kelly, C. Zweben, 2000. Comprehensive composite materials. Elsevier Science: Oxford.

A. Khaund, V. Krstic, P. Nicholson, 1977. Influence of elastic and thermal mismatch on the local crack-driving force in brittle composites. J. Mater. Sci. 12, 2269-2273.

G. Lamé, 1852. Leçons sur la théorie mathématique de l'élasticité des corps solides. Bachelier: Paris.

H. Liu, E. Pan, Y. Cai, Y., 2018. General surface loading over layered transversely isotropic pavements with imperfect interfaces. Adc. Eng. Softw. 115, 268-282.

E. Mathieu, 1868. Mémoire sur le mouvement vibratoire d'une membrane de forme elliptique. Journal de Mathématiques Pures et Appliquées 13, 137-203.

E. Mathieu, 1890. Théorie de l'élasticité des corps solides. Gauthier-Villars: Paris.

G. Maugin, 1999. Nonlinear waves in elastic crystals. Oxford university press: Oxford.

R. Mindlin, 1956. Simple modes of vibration of crystals. J. Appl. Phys. 27, 1462-1466.

R. Mindlin, N. Eshel, 1968. On first strain-gradient theories in linear elasticity. Int. J . Solid. Struct. 4, 109-124.

G. Mulholland, M. Cobble, 1972. Diffusion through composite media. Int. J. Heat Mass Transfert 15, 147-160.

A. Noor, W. Burton, 1992. Computational models for high-temperature multilayered composite plates and shells. Appl. Mech. Rev. 45, 419-446.

J. Padovan, 1975. Solution of transient temperature fields in laminated anisotropic slabs and cylinders. Int. J. Engng. Sci. 13, 247-260.

E. Pan, 2001. Exact solution for simply supported and multilayered magneto-electro-elastic plates. J. Appl. Mech. 68, 608-618.

E. Pan, P. Heyliger, 2002. Free vibrations of simply supported and multilayered magneto-electro-elastic plates. J. Sound Vib. 252, 429-442.

E. Pan, 2019. Green's functions for geophysics: a review. Rep. Prog. Phys. 82, 106801.

N. Pagano, 1970. Exact solutions for rectangular bidirectional composites and sandwich plates. J. Composite Mater. 4, 20-34.

N. Padture, 2016. Advanced structural ceramics in aerospace propulsion. Nat. Mater. 4, 525-529.

M. Poisson, 1829. Mémoire sur l'équilibre et le mouvement des corps élastiques. Mémoires de l'Académie des sciences, Tome 8, 357-570.

W. Poole, M. Ashby, N. Fleck, 1996. Micro-hardness of annealed and work-hardened copper polycrystals. Scr. Mater. 34, 559-564.

J. Reddy, 1984. Exact solutions of moderately thick laminated shells. J. Eng. Mech. 110, 794-809.

C. Ru, P. Schiavone, 1997. A circular inclusion with circumferentially inhomogeneous interface in antiplane shear. Proc. R. Soc. Lond A 453, 2551-2572.

M. Savoia, J. Reddy, 1995. Three-dimensional thermal analysis of laminated composite pates. Int. J. Solids Struct. 32, 593-608.

S. Srinivas, A. Rao, 1970. Bending, vibration and buckling of simply supported thick orthotropic rectangular plates and laminates. Int. J. Solids Struct. 6, 1463-1481.

A. Stroh, 1958. Dislocations and Cracks in Anisotropic Elasticity. Philos. Mag. 3, 625-646.

A. Stroh, 1962. Steady state problems in anisotropic elasticity. J. Math. Phys. 41, 77-103.

A. Sutton, R. Balluffi, 1995. Interfaces in Crystalline Materials. Oxford: Oxford University Press.

A. Tabiei, W. Zhang, 2018. Composite laminate delamination simulation and experiment: A review of recent development. Appl. Mech. Rev. May 2018, 70, 030801.

T. Taylor, A. Nayfeh, 1996. The vibration characteristics of thick rectangular multilayered plates. Compos. B 27, 623-631.

T. Ting, 1996. Anisotropic elasticity: theory and applications. New York/Oxford: Oxford University Press.

R. Toupin, 1973. Elastic materials with couple-stresses. Arch. Ration. Mech. Anal. 11, 385-414.

M. Touratier, 1991. An efficient standard plate theory. Int. Engng. Sci. 29, 901-916;

T. Tran, H. Lee, S. Lim, 2005. Structural intensity analysis of thin laminated composite plates subjected to thermally induced vibration. Compos. Struct. 78, 70-83.

V. Tungikar, K. Rao, 1994. Three dimensional exact solution of thermal stresses in rectangular composite laminate. Compos. Struct. 27, 419-430.

A. Vattré, 2015. Mechanical interactions between semicoherent heterophase interfaces and free surfaces in crystalline bilayers. Acta Mater. 93, 46-59.

A. Vattré, 2016. Elastic interactions between interface dislocations and internal stresses in finite-thickness nanolayered materials. Acta Mater. 114, 184-197.

A. Vattré, 2017a. Elastic strain relaxation in interfacial dislocation patterns: I. A parametric energy-based framework. J. Mech. Phys. Solids 105, 254-282.

A. Vattré, 2017b. Elastic strain relaxation in interfacial dislocation patterns: II. From long- and short-range interactions to local reactions. J. Mech. Phys. Solids 105, 283-305.

A. Vattré, Pan, 2018. Three-dimensional interaction and movements of various dislocations in anisotropic bicrystals with semicoherent interfaces. J. Mech. Phys. Solids 124, 929-956.

A. Vattré, Pan, 2019. Semicoherent heterophase interfaces with core-spreading dislocation structures in magneto-electro-elastic multilayers under external surface loads. J. Mech. Phys. Solids 124, 929-956.

P. Vidal, O. Polit, 2008. A family of sinus finite elements for the analysis of rectangular laminated beams. Compos. Struct. 84, 56-72.

N. Waksmanski, E. Pan. An analytical three-dimensional solution for free vibration of a magneto-electro-elastic plate considering the nonlocal effect. J. Intell. Mater. Syst. Struct. 28, 1501-1513.

X. Wang, E. Pan, 2007. Exact solutions for simply supported and multilayered piezothermoelastic plates with imperfect interfaces. The Open Mech. J. 1, 1-10.

J. Whitney, N. Pagano, 1970. Shear deformation in heterogeneous anisotropic plates. J. Appl. Mech. 37, 1031-1036.

B. Wu, A. Heidelberg, J. Boland, 2005. Mechanical properties of ultrahigh-strength gold nanowires. Nat. Mater. 4, 525-529.

L. Yang, Y. Gao, E. Pan, N. Waksmanski, 2015. An exact closed-form solution for a multilayered one-dimensional orthorhombic quasicrystal plate. Acta Mech 226, 3611-3621.

L. Yang, Y. Li, Y. Gao, E. Pan, N. Waksmanski, 2015. Three-dimensional exact electric-elastic analysis of a multilayered two-dimensional decagonal quasicrystal plate subjected to patch loading. Compos. Struct. 171, 198-216.

L. Yang, Y. Li, Y. Gao, E. Pan, 2018. Three-dimensional exact thermo-elastic analysis of multilayered two-dimensional quasicrystal nanoplates. Appl. Math. Model. 63, 203-218.

Y. Yu, Z. Xue, C. Li, X. Tian, 2016. Buckling of nanobeams under nonuniform temperature based on nonlocal thermoelasticity. Compos. Struct. 146, 108-113.

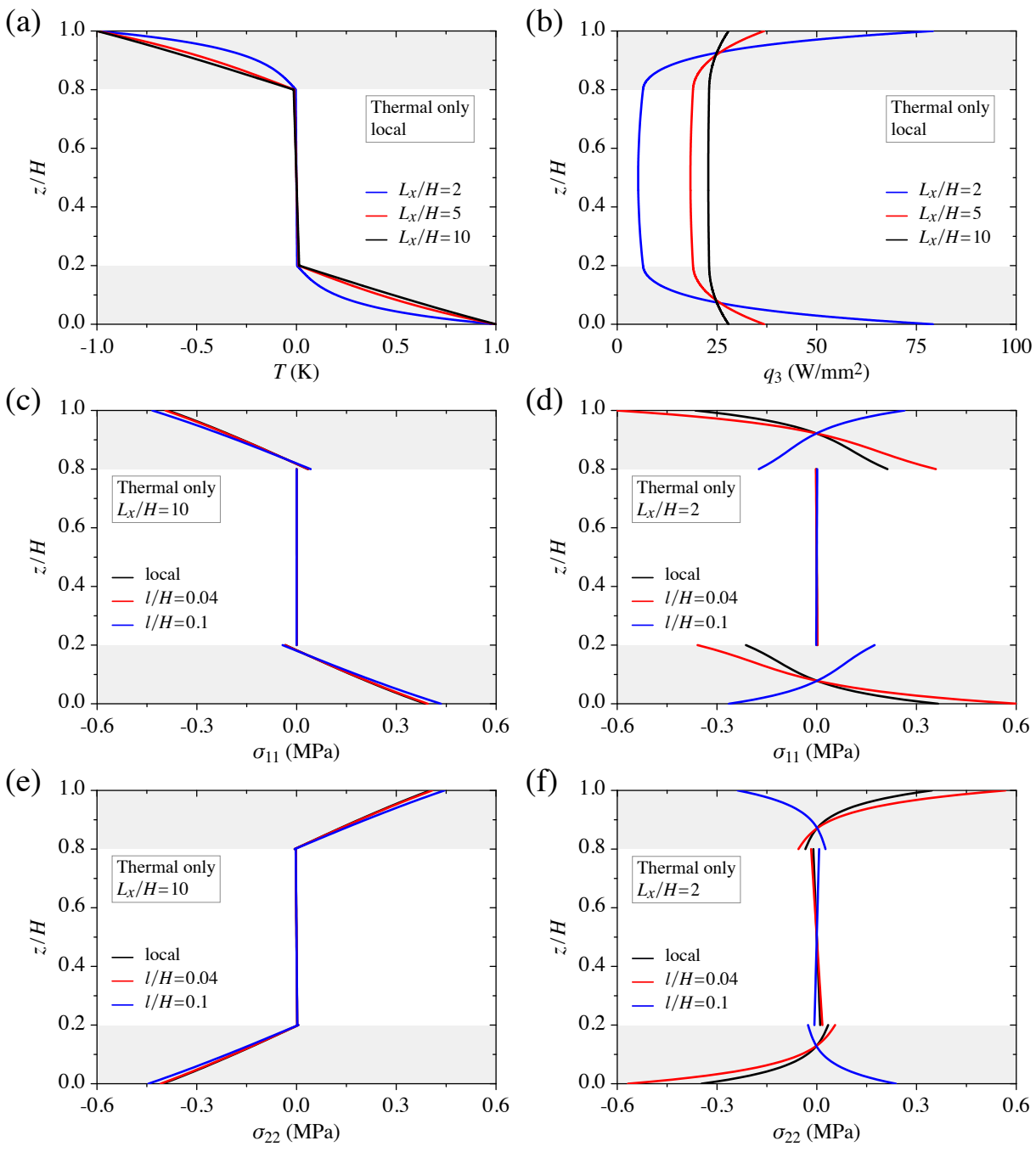

Figure 3: Steady-state thermoelastic bending of a three-layered structure with square plates subjected to a sinusoidal temperature rise at the two external faces. The first terms in the temperature expansion are considered, thus $m = n = 1$. The light grey regions are the unidirectional graphite-epoxy composites with fibers oriented along the x_1-direction, which are bonded by a soft core material. The through-the-thickness distributions for different values of the aspect ratios L_x/H and of the nonlocal parameters l/H are depicted for (a) the temperature T, (b) the normal heat flux q_3, (c-d) the in-plane stresses σ_{11}, and (e-f) σ_{22}. The standard local case corresponds to the field solutions with $l = 0$.

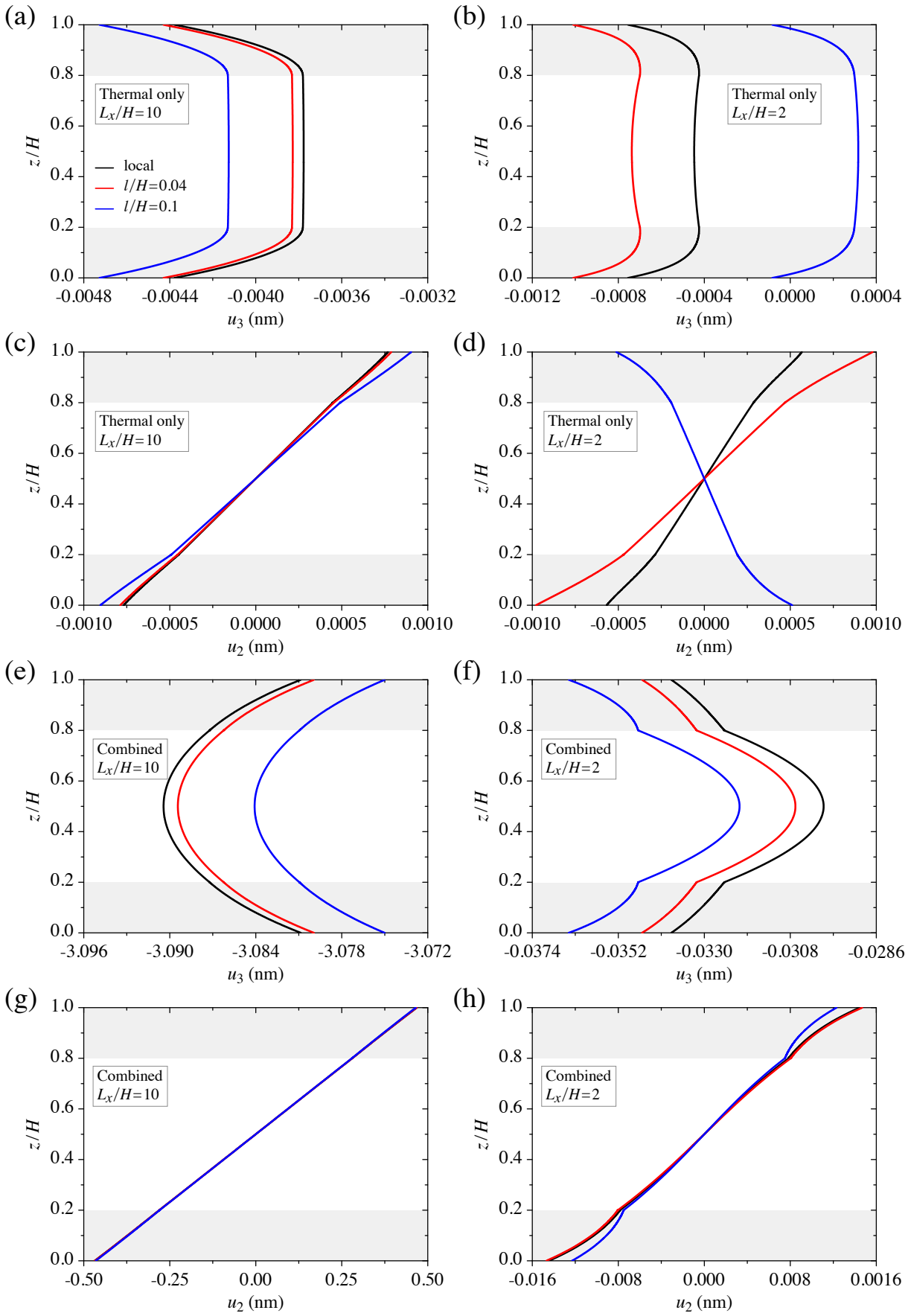

Figure 4: Steady-state thermoelastic bending of a three-layered structure with square plates subjected to a sinusoidal temperature and to a combined thermomechanical loading at both external faces. The first terms in the Fourier series expansions are considered, thus $m = n = 1$. The light grey regions are the unidirectional graphite-epoxy composites with fibers oriented along the x_1-direction, which are bonded by a soft core material. Under thermal loading only, the through-the-thickness distributions for different values of the aspect ratios L_x/H and of the nonlocal parameters l/H are depicted for (a-b) the normal displacement u_3, and (c-d) the in-plane displacement u_2. Under combined loading, the profiles are analogously displayed for (e-f) u_3, and (g-h) u_2. The standard local case corresponds to the field solutions with $l = 0$.

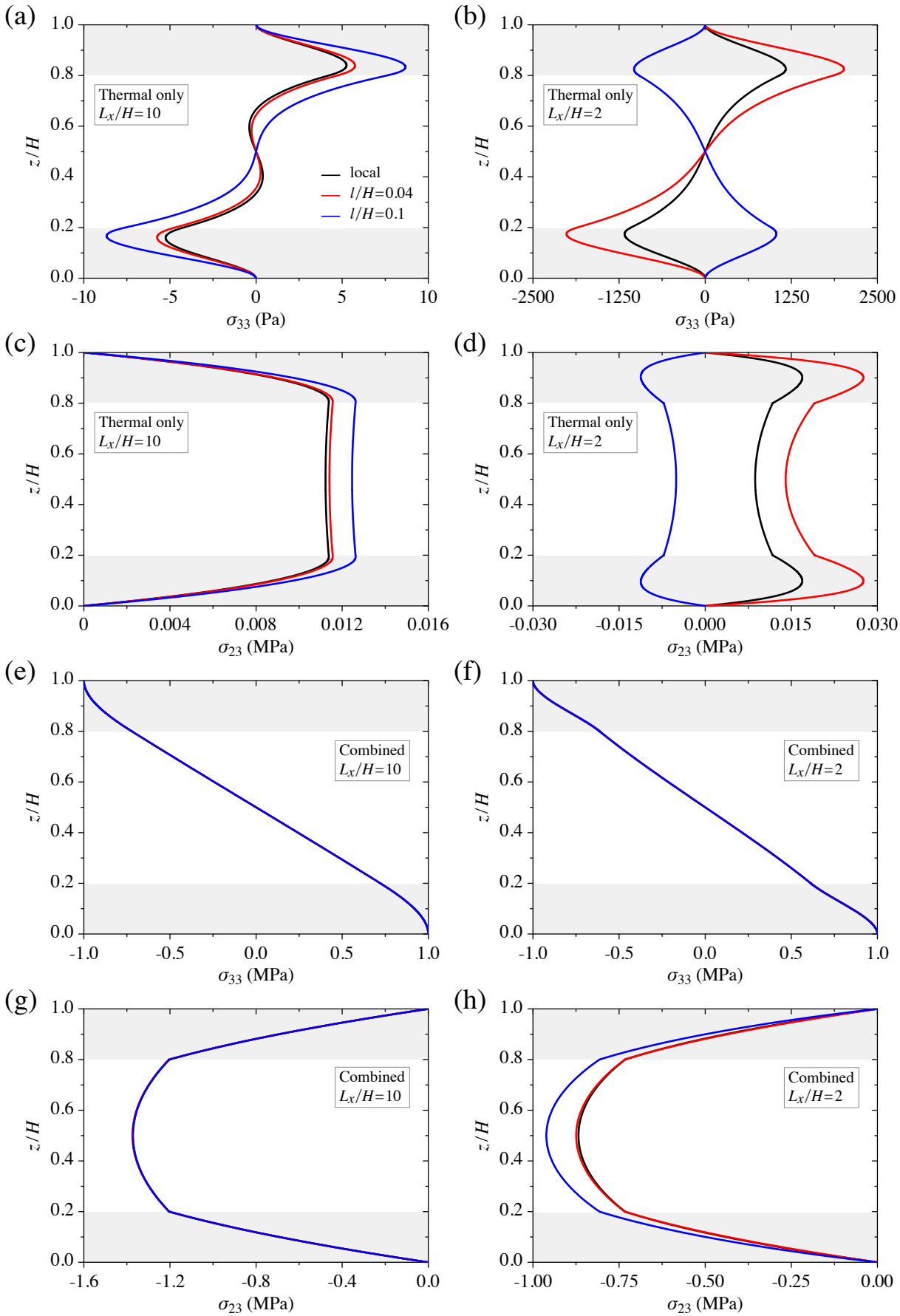

Figure 5: Steady-state thermoelastic bending of a three-layered structure with square plates subjected to a sinusoidal temperature and to a combined thermomechanical loading at both external faces. The first terms in the Fourier series expansions are considered, thus $m = n = 1$. The light grey regions are the unidirectional graphite-epoxy composites with fibers oriented along the x_1-direction, which are bonded by a soft core material. Under thermal loading only, the through-the-thickness distributions for different values of the aspect ratios L_x/H and of the nonlocal parameters l/H are depicted for (a-b) the normal stress σ_{33}, and (c-d) the transverse shear stress σ_{23}. Under combined loading, the profiles are analogously displayed for (e-f) σ_{33}, and (g-h) σ_{23}. The standard local case corresponds to the field solutions with $l = 0$.

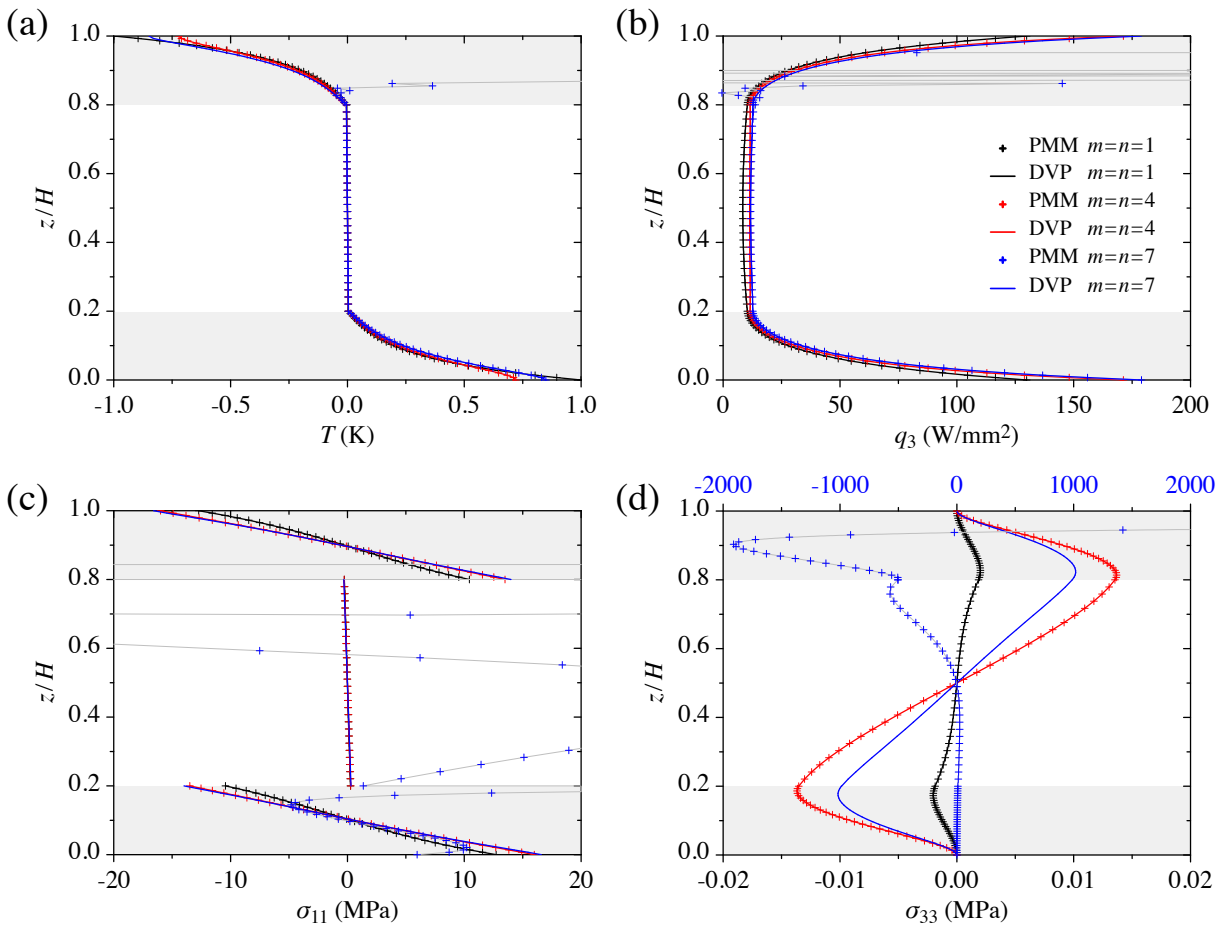

Figure 6: Numerical efficiency comparison of thermoelastic field solutions obtained by the propagation matrix method (PMM) and the dual variable and position (DVP) technique under combined loading, for various numbers of coefficients in the Fourier series by means of (a) the temperature T, (b) the normal heat flux q_3, (c) the in-plane stress σ_{11}, and (d) the normal stress σ_{33}. In (d), the range of the normal stress σ_{33} determined by the PMM approach with $m = n = 7$ is shown on the top axis.

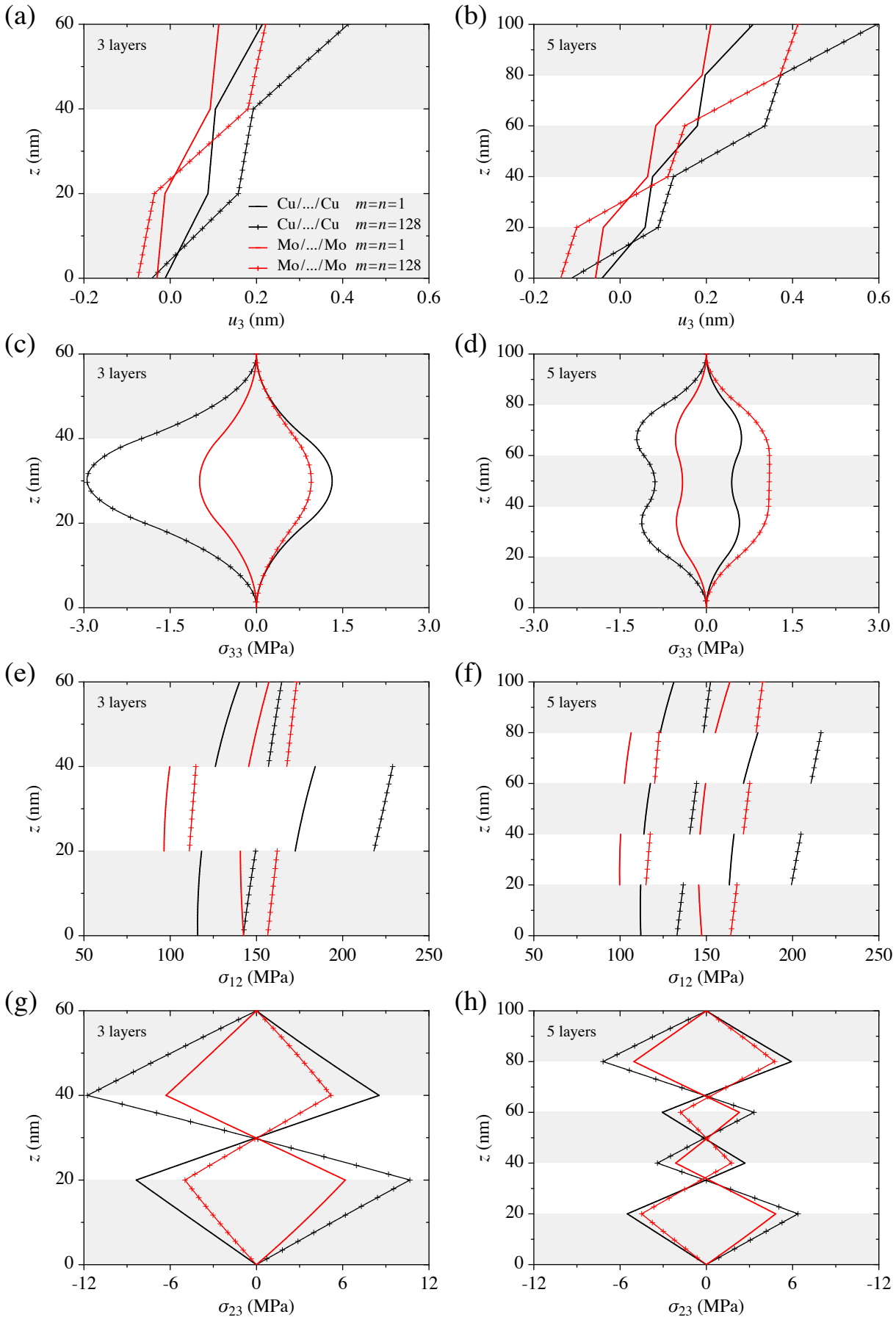

Figure 7: Steady-state thermoelastic bending of a three- and five-layered structures composed of Cu and Mo square plates subjected to a combined thermomechanical loading at both external faces. Field solutions obtained by the first terms in the Fourier series expansions only are displayed by solid lines, while the converged results to the exact solutions with 128 harmonic terms are shown by lines and symbols. The through-the-thickness distributions for different stacking sequences of individual layers are depicted for (a-b) the normal displacement u_3, (c-d) the normal stress σ_{33}, (e-f) the in-plane shear stress σ_{12}, and (g-h) the transverse shear stress σ_{23}.

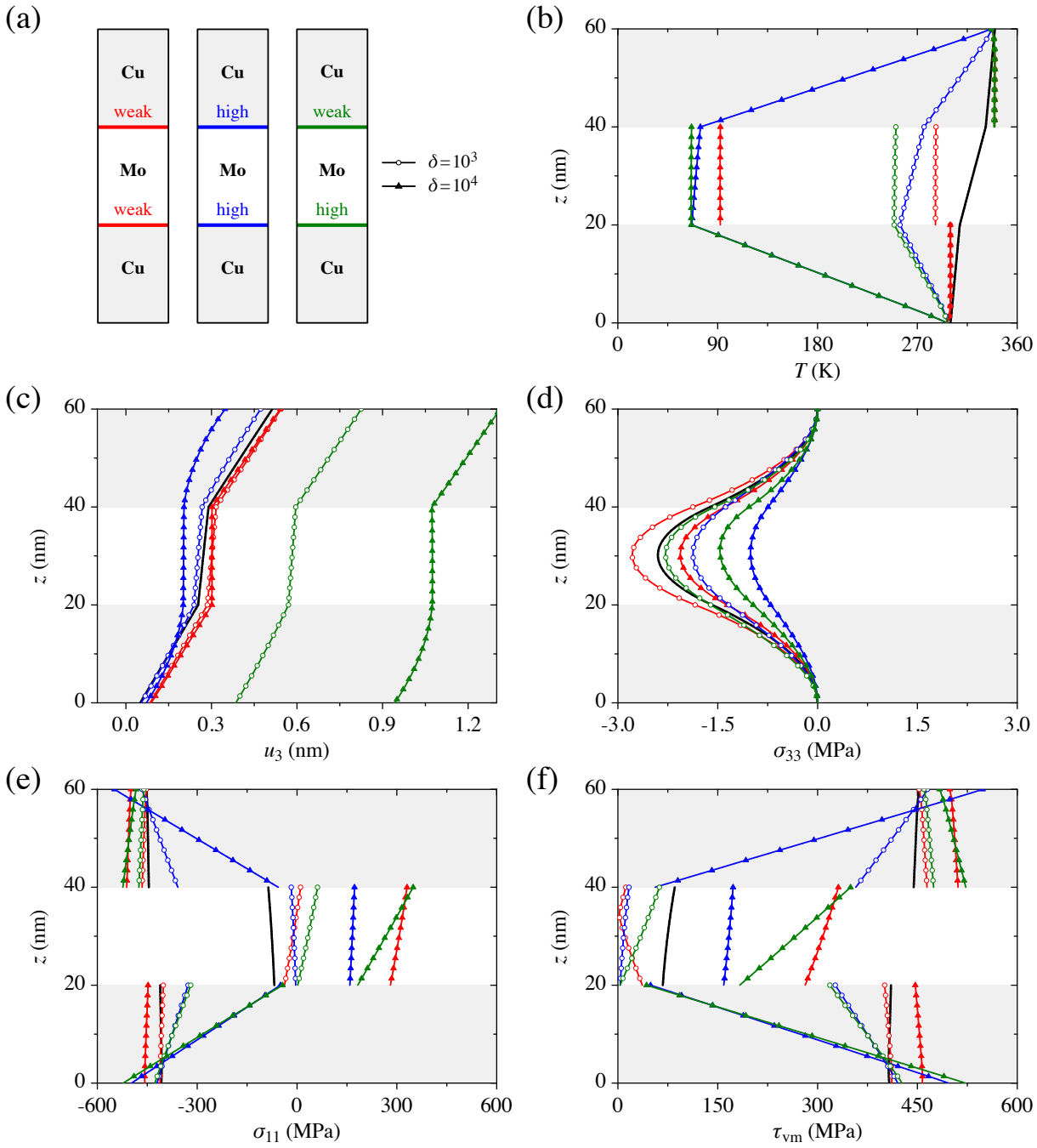

Figure 8: Steady-state thermoelastic bending of the Cu/Mo/Cu structures subjected to a combined thermomechanical loading at both external faces. (a) Imperfect thermal contact between constituents are introduced at both internal interfaces. The corresponding consequence in the through-the-thickness distributions of (b) the temperature T, (c) the normal displacement u_3, (d) the normal stress σ_{33}, (e) in-plane stress σ_{11}, and (f) the von Mises stress τ_{vm}.

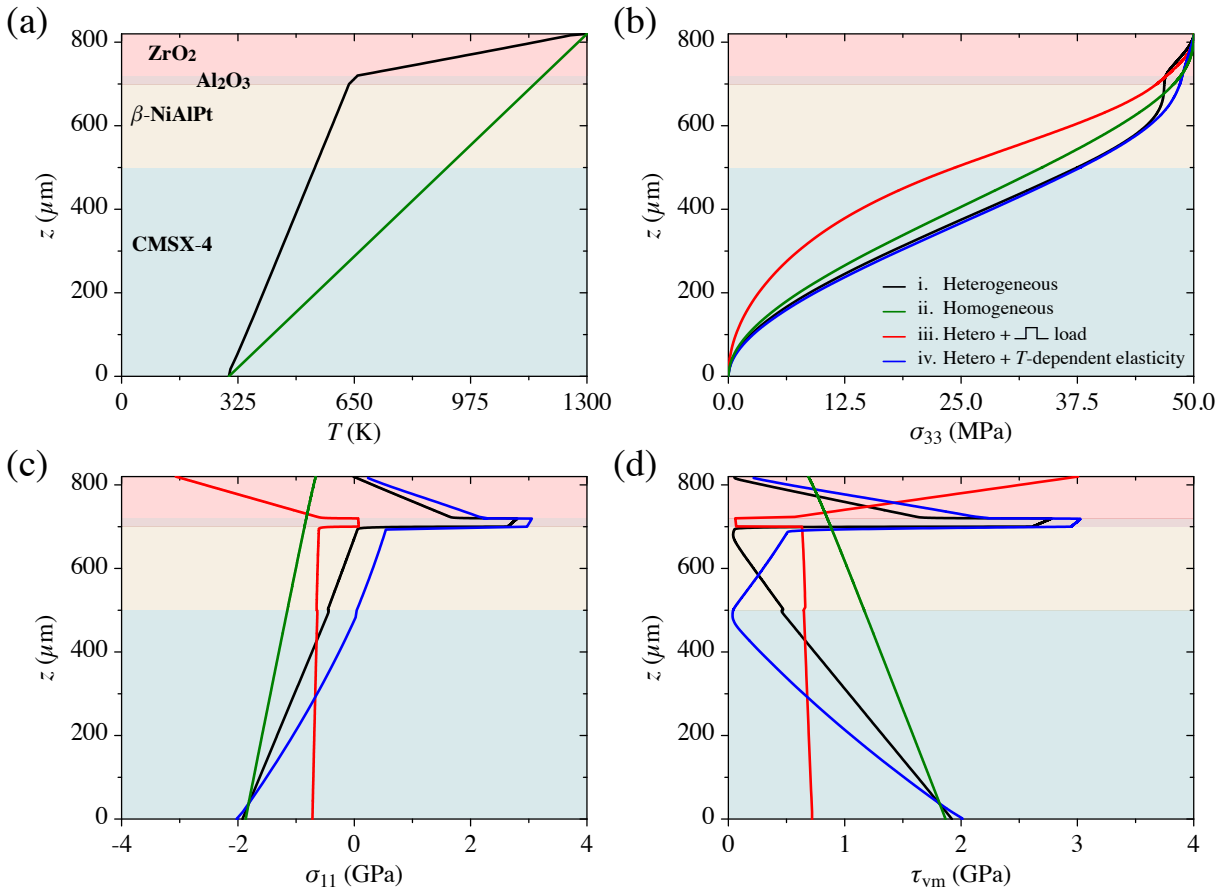

Figure 9: Steady-state response of a thermal barrier coated superalloy with four distinct layers subjected to a combined thermomechanical loading at both external faces. The through-the-thickness distributions of (a) the temperature T, (b) the normal stress σ_{33}, (c) in-plane stress σ_{11}, and (d) the von Mises stress τ_{vm}. Thermal stress solutions are solved for four thermoelastic problems with perfectly bounded interfaces, as described in the text.

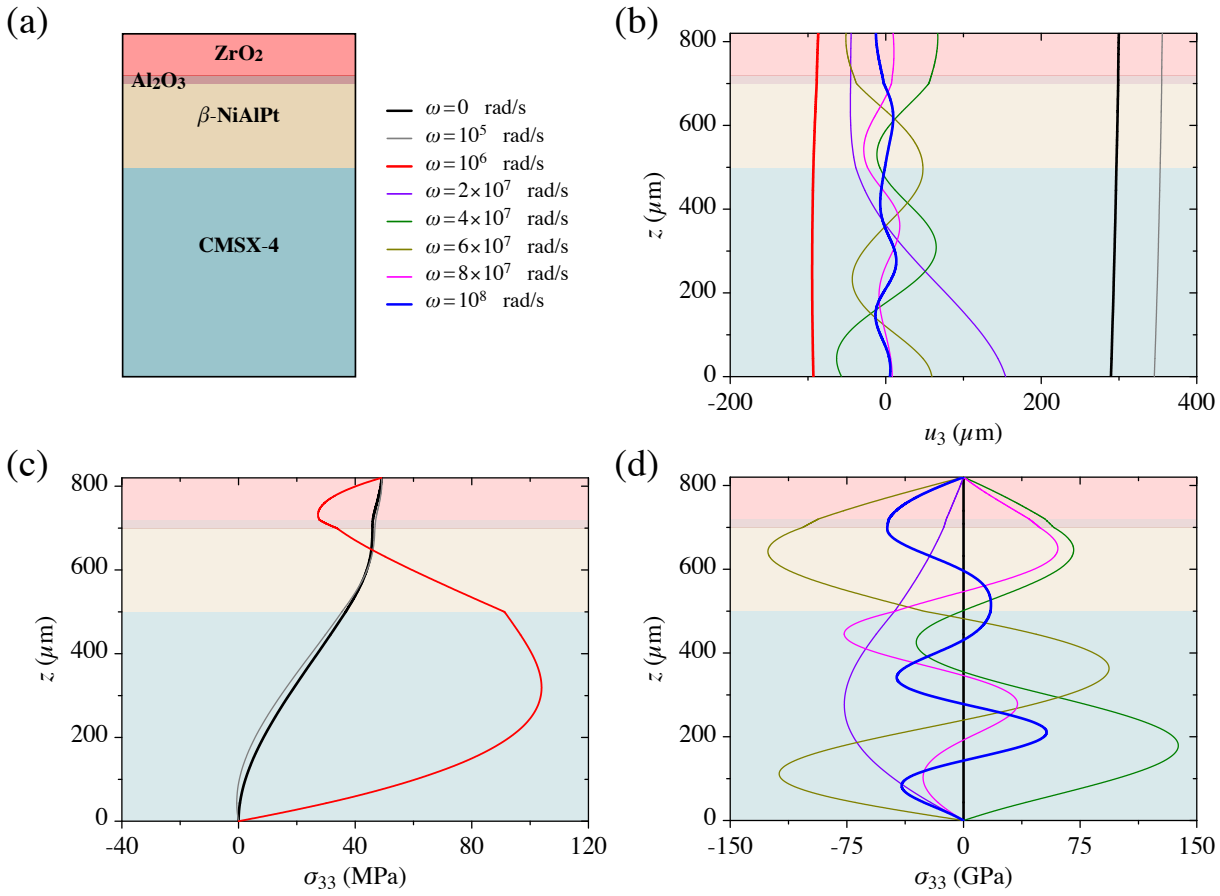

Figure 10: (a) Forced harmonic excitation of vibration in the thermal barrier coated superalloy applied to the top surface with various frequencies. The corresponding through-the-thickness distributions of (a) the normal displacement u_3, (c) the normal stress σ_{33} for low frequencies, and (c) the normal stress σ_{33} for the higher frequencies.

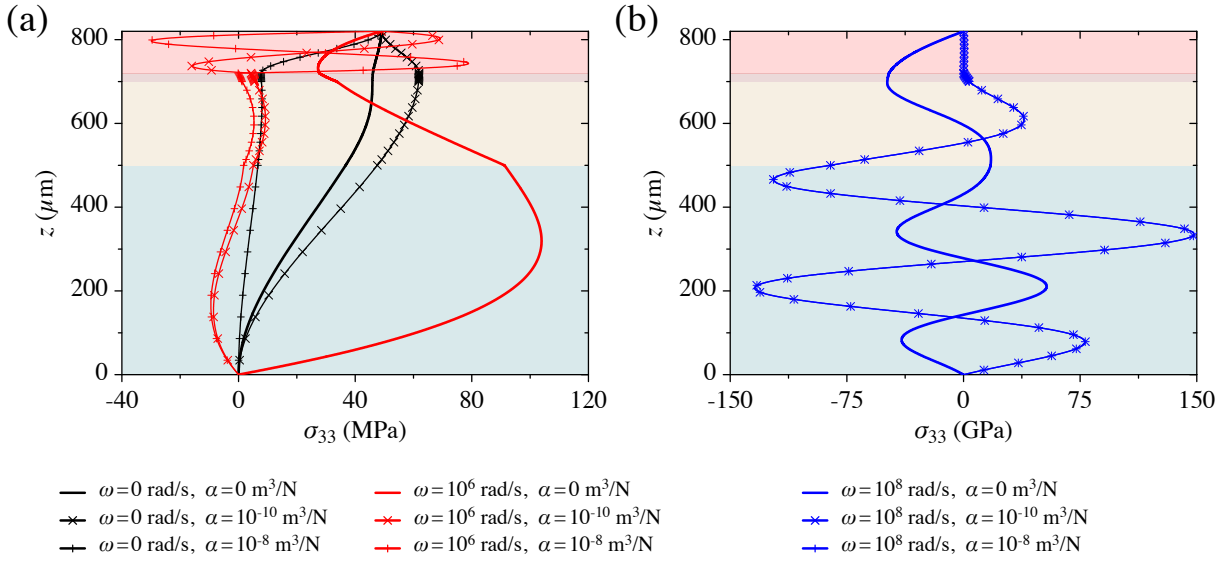

Figure 11: Forced harmonic excitation analysis of the thermal barrier coated superalloy with imperfect mechanical contact between constituents. The corresponding through-the-thickness distributions of (a) the normal stress σ_{33} for low frequencies, and (b) the normal stress σ_{33} for the higher frequencies

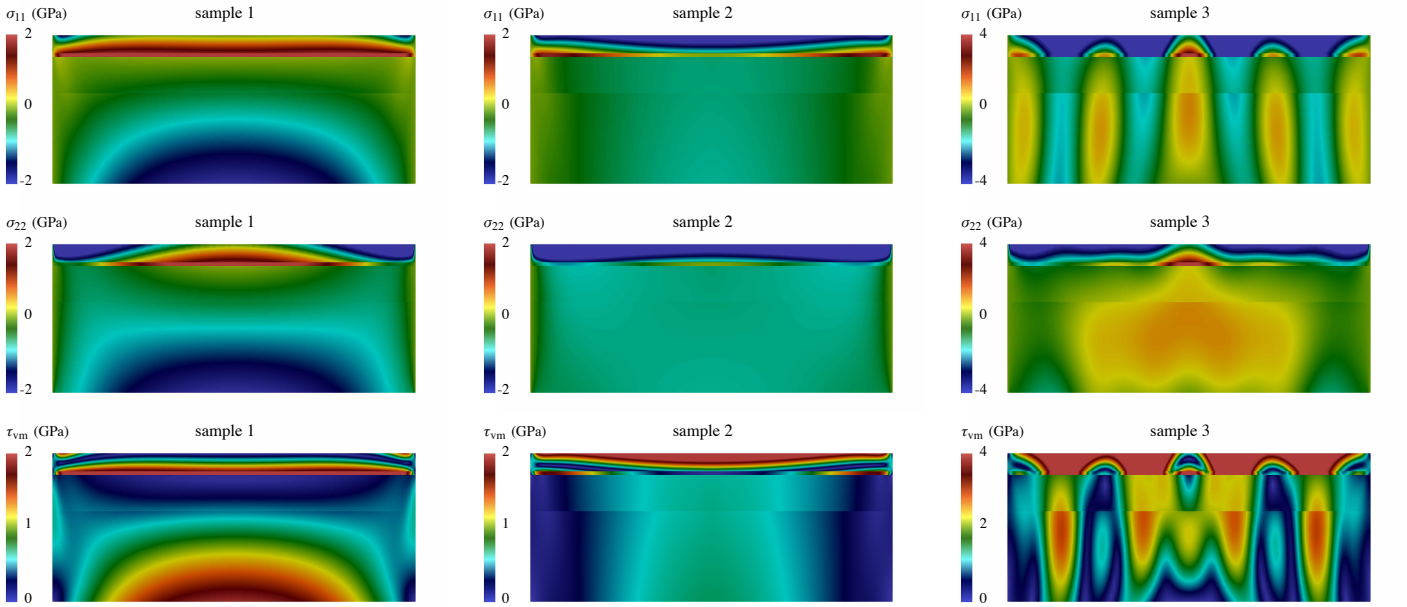

Figure 12: Residual stresses in the thermal barrier coated superalloy for three illustrative boundary-value problems, namely the steady-state case with uniformly distributed normal tractions on the top surface (sample 1), the steady-state case with heterogeneously distributed normal tractions (sample 2), and the time-harmonic vibration case with $\omega = 10^7$ rad/s and uniformly distributed normal tractions (sample 3).